Real Time Reflectometry of Ga–based Compound Semiconductor Films on Silicon during Plasma Enhanced Molecular Beam Epitaxy

by

Christopher Jay Harris

A thesis submitted to the Graduate Faculty of
North Carolina State University
in partial fulfillment of the
requirements for the degree of
Master of Science

MATERIALS SCIENCE AND ENGINEERING

Raleigh, NC
1999

APPROVED BY:

Chair of Advisory Commitee

Content

Introduction

Film Growth Theory

Plasma Processes

Laboratory Background

GaN Literature Review

Experimental Research

Future Recommendations

1

Introduction

1.1 Material Evolution

Composite structures have near surface regions with properties differing from those of the bulk material. The relationship between surface and bulk properties can sometimes have conflicting behavior to fulfill system requirements. For example, an application may require a high strength material to possess a hardness coating. Here the ductile nature of the matrix would be at odds with a brittle surface. Thin film coatings on various substrates represent one class of composite systems[1.1].

Historically, production of solid materials involved melting/ solidification technology until deposition from vapor sources matured in the 1950's. The advent of vapor phase growth brought on material property diversity unseen in traditional liquid phase melts. With liquid phase processing, the final product comes out close to thermodynamic equilibrium, relative to vapor phase counterparts, which can incorporate properties far removed from equilibrium or anywhere in between. This is accomplished by separating the steps in solid formation: 1) vapor generation, 2) transport from source to substrate, and 3) film growth. Aside from thermodynamic considerations, vapor phase deposition allows microstructure variations in grain size and composition unavailable to liquid melt processing[1.1].

Except for the plasma tube which debuted in 1855, the mid twentieth century set the stage for tremendous material opportunities. Before 1947 expired, the molecular beam epitaxy technique started the momentum, providing a vapor channel for material processing. By 1950, the first P/N junction had opened up the field of solid state electronics. As 1960 heralded in the new decade, the first laser, light emitting diode, and vapor phase epitaxy system emerged the same year. This confluence in achievements cleared the way for: fiber optic communications, large scale data storage, electro–optic devices, and cost effective thin film growth[1.2].

It’s rather symbolic that this thesis builds on those landmark events. In fact, the first light emitting diode was a GaP diode with impurities. It’s likely the impurities participated in the light emission, because the pure most stable GaP structure has an indirect band gap. In contrast, GaN exhibits a direct electron transition which makes it a prime candidate as a blue laser medium. With red solid state optical devices already firmly established, blue and green would round out the visible spectrum to allow: high resolution color monitors, energy efficient lighting, submarine communications, and high density data storage. As the field expands, material scientists take on a role which increasingly encompasses disparate technologies: metalorganic precursors, ultra high vacuum chambers, plasma systems, compound semiconductors, and real time optical sensors. This thesis will attempt to fuse these vastly different fields of interest, as they apply to GaP, GaN based heterostructure growth.

References

[1.1] R. F. Bunshah, in *Deposition Technologies for Films and Coatings*, R. F. Bunshah, ed., Noyes: Park Ridge, NJ (1982), Ch. 1.

[1.2] G. W. A. Dummer, *Electronic Inventions and Discoveries*, Institute of Physics: Philadelphia, PA (1997).

2

Film Growth Theory

2.1 Introduction

Thin film formation from vapor phase chemical reactions has become a popular method for deposition. The advantages of chemical vapor deposition over traditional physical vapor deposition techniques lie in the control of incoming source material purity, film uniformity over rough surfaces, reduced temperature film preparation, and increased variety of compounds available through chemical reaction. However, these additional degrees of freedom also complicate matters with respect to reactant introduction, influence of substrate temperature control, film composition via competing reaction paths, and the phase transformation kinetics. Unfortunately, I never ran across any mathematical model or approach which treated the chemical reaction kinetics in combination with the phase transformation process. As such, I will treat each individually in an effort to achieve continuity.

2.2 Vapor Sources

Source materials may be solid, liquid or gas at room temperature. Until the advent of plasmas, evaporation was the most popular technique for producing vaporous reactants from solid and liquid sources. Vaporization could be achieved through resistance heating, electron beam activation, laser excitation, or induction heating[2.3].

However, most solid and liquid sources have been displaced by gaseous materials due to better mass flow control and ion assisted decomposition of the vapor. These ions remove all previous thermal barriers associated with “inert” gases, because plasma formation is strictly a mechanical process. Atoms in the presence of electric fields lose electrons to form ions. Due to their size, electrons have high mobilities relative to their parent ions. This mobility helps them couple with the electric field and gain enormous kinetic energies, which result in subsequent collisions with any molecule in sight.

Clearly, these electrons have no preference as to which molecule they hit or where the molecule is fragmented or energized, so no thermal barrier exists. Although plasmas have produced many new reactant species never realized through thermal routes, the nonequilibrium process does not obey any traditional reaction kinetics. Therefore, plasmas may permit undesirable reaction paths, reduce selectivity over which reactant species is obtained, and allow very little control over reaction rate. The various types of ion sources[2.1] are summarized in figure 2.1.

2.3 Reaction Kinetics

In light of the nonequilibrium nature of plasmas, very little will be said or is known about the chemical reactions. In traditional reaction kinetics, you could list all the possible reaction paths and set up equilibrium expressions for each reaction. Using mass and energy balances, you could generally obtain a system of n equations and n unknowns which could be solved simultaneously. By playing around with reaction temperature, pressure, and reactant concentrations, you could find a set of conditions which optimized the desired product and minimized various undesirable byproducts.

The most common reaction process, particularly in the microelectronics industry, is the decomposition of a molecular gaseous species to achieve a purified elemental product, such as:

$$SiH_4(g) \rightarrow Si(s) + 2H_2(g)$$

Figure 2.2 illustrates the vast array of reaction paths available in chemical vapor deposition[2.3].

Beyond opening up new reaction paths, plasmas contribute to the phase transformation process as well, by providing photons, ion bombardment, electron bombardment, and charge accumulation on nonconducting surfaces. These energetic processes improve surface diffusion, preferentially sputter away weakly bonded material, enhance surface capture by increasing the binding energy, and ultimately provide energy to overcome the nucleation/ growth barriers[2.1].

2.4 Formation Stages

Basically, there are three types of film growth: (a) 2–D layer growth (van der Merwe mechanism); (b) 3–D nucleation, forming, growth, and coalescence of islands (Volmer–Weber mechanism); (c) 2–D monolayer growth that shifts to 3–D nucleation/ growth in subsequent layers (Stranski–Krastanov mechanism). These different growth modes, represented in figure 2.3, depend principally on the bond strength and/or stress between the substrate and the film. Fortunately, most films follow the classical Volmer–Webber model, so this mechanism will be discussed in greater detail.

From electron microscopy experiments where films were grown in–situ, there emerged three distinct stages in film deposition: (a) nucleation, where small nuclei are formed that are randomly distributed over the substrate surface; (b) growth of the nuclei and formation of larger islands, which often have the shape of small crystals; and (c) coalescence of the islands and formation of a connected network containing empty channels. Figure 2.4 depicts the latter two film stages, because the nuclei in stage one are too small to be resolved under the electron microscope[2.1].

2.5 Condensation

The energy loss of a particle which has impinged on the surface and then left it is characterized by the accommodation coefficient defined as follows:

$$\alpha = \frac{T_c - T_v}{T_c - T_s}$$

where: α = *accommodation coefficient*
T_c = *temperature corresponding to the energy of the incident particle*
T_v = *temperature of the emitted particle*
T_s = *substrate temperature*

The mean time a particle resides on, or stays adsorbed to, or is accommodated by a surface is:

$$\tau_s = \frac{1}{v} e^{\frac{Q_{des}}{kt}}$$

where: τ_s = *residence time*
v = *surface vibrational frequency of adatoms*
Q_{des} = *desorption energy of the particle*
k = *Boltzmann constant*
T = *mean temperature of particle during residence time*

A particle impinging on a surface has kinetic energy due to the substrate temperature, excess source energy, and/or plasma excitation while on the surface. This kinetic energy is dissipated partially by surface diffusion. The mean diffusion length is:

$$\overline{X} = \sqrt{2}\, a e^{\frac{Q_{des} - Q_{dif}}{2kT}}$$

where: $\overline{X}$ = *mean diffusion length*
a = *lattice spacing*
Q_{des} = *desorption energy of the particle*
Q_{dif} = *surface diffusion energy*
k = *Boltzmann constant*
T = *mean temperature of particle during residence time*

The ratio of impinging flow to the re–evaporation flow is called the saturation ratio, and is an important parameter for thin film condensation. Since impingement is directly related to the partial pressure of the deposition species in the gas phase, P, and re–evaporation is directly related to the vapor pressure of the deposition species at the substrate temperature, P_c, the saturation ratio is usually expressed as P/P_c. When:

(a) $P/P_c < 1$, the system is unsaturated;
(b) $P/P_c = 1$, the system is saturated;
(c) $P/P_c > 1$, the system is supersaturated.

Condensation depends mainly on two quantities: desorption energy, Q_{des}, characterizing the binding of condensed atoms to the substrate; and sublimation heat, Q_s, characterizing the mutual binding of condensed atoms among themselves. If:

(a) $Q_{des} << Q_s$, condensation occurs unsaturated and coverage is high;
(b) $Q_{des} = Q_s$, condensation occurs at moderate supersaturation and the heterogeneous nucleation model applies;
(c) $Q_{des} >> Q_s$, condensation occurs only at high supersaturation, coverage is low, and the atomistic nucleation model applies[2.1].

2.6 Nucleation

When comparing desorption energy to sublimation heat, two models currently exist to explain nucleation: (a) classical heterogeneous nucleation, and (b) atomistic (statistical) nucleation. Even with these two theories, some films do not conform to either model. The basic difference between the two models involves the size of the critical nucleus. Heterogeneous nucleation uses bulk material thermodynamic quantities, so in a pure sense, can only be applied to critical nuclei containing greater than 100 molecules. On the other hand, atomistic nucleation takes into account the Gibbs–Thomson effect, and other microscopic phenomenon, which influence thermodynamic quantities for small atomic clusters in the range of 1 to 10 molecules. In practice, Lewis and Anderson[2.2] have shown due to similarities in the fundamental derivation, that heterogeneous nucleation results compare favorably with atomistic nucleation results even below the 100 molecule cluster limit, as shown in figure 2.5.

Since heterogeneous nucleation theory is covered in any introductory phase transformation book such as Porter and Easterling[2.5], and atomistic nucleation theory is readily available in sources such as Lewis and Anderson[2.2], I just want to present the final expressions for both models. In heterogeneous nucleation, the nucleation rate has the following relationship:

$$J = Z2\pi r^{*} n_{o} a \sin\theta p \frac{1}{\sqrt{2mkT}} e^{\frac{Q_{des} - Q_{dif} - \Delta G^{*}}{kT}}$$

where: J = *nucleation rate*
Z = *Zeldovich constant*
r^* = *nuclei critical radius*
n_o = *density of adsorption sites*
a = *lattice spacing*
θ = *contact angle*
p = *partial pressure of deposition species*
m = *molecular mass*
k = *Boltzmann constant*
T = *mean temperature of nuclei*
Q_{des} = *desorption energy*
Q_{dif} = *surface diffusion energy*
ΔG^* = *critical Gibbs free energy*

Similarly, for atomistic nucleation, the nucleation rate can be expressed as[2.1]:

$$J = Na^{2} n_{o} \left(\frac{N}{n_{o}}\right)^{i^{*}} e^{\frac{(i^{*}+1)Q_{des} - Q_{dif} + E^{*}}{kT}}$$

where: J = *nucleation rate*
N = *impinging flow*
a = *lattice spacing*
n_o = *density of adsorption sites*
i^* = *number of molecules in nuclei*
Q_{des} = *desorption energy*
Q_{dif} = *surface diffusion energy*
E^* = *disintegration energy for i* cluster*
k = *Boltzmann constant*
T = *mean temperature of nuclei*

2.7 Growth

For 3–D growth theory, island growth is always limited by the slower of the two growth processes acting in series; namely, surface diffusion and interface transfer. For surface diffusion, growthrate is obtained from the relation:

$$J_s = \frac{2\pi D_s}{\ln l}(\bar{n} - n')$$

where: J_s = *surface diffusion growthrate*
D_s = *surface diffusion coefficient*
l = *distance to mean concentration of adatoms*
$\bar{n}$ = *mean concentration of adatoms*
n' = *concentration of adatoms at island edge*

The rate of interface transfer is determined by the interface area and the difference between the numbers of atoms which join or leave the island. Thus:

$$J_t = 4\pi r^2 \phi \beta (n' - n_t)$$

where: J_t = *interface transfer growthrate*
r = *island radius*
ϕ = *shape factor*
β = *probability coefficient*
n' = *concentration of adatoms at island edge*
n_t = *equilibrium concentration of adatoms*

Since the two mechanisms work in series, $J_t = J_s$ under equilibrium conditions[2.1].

2.8 Coalescence

The next stage, coalescence, can proceed in three ways depicted in figure 2.6:

(a) *Ostwald ripening*: vapor pressure difference between small and large radii nuclei allows the larger nuclei to retain more of the incoming material flux and thus grow faster than smaller nuclei until the smaller nuclei eventually disappear.

(b) *Cluster mobility*: nuclei have a certain level of mobility on the surface. Upon collision, the mobile nuclei have an opportunity to coalesce together. Generally, smaller nuclei have higher mobility, and hence, higher collision probability.

(c) *Growth coalescence*: if two growing particles touch one another, depending on substrate temperature and surface energies, they can either retain their shape (sinter) or exhibit a liquid like behavior and coalesce into a single crystallite, as seen in figure 2.7.

As a final note to coalescence, mechanisms (b) and (c) determine whether a film becomes epitaxial. Surprisingly, lattice mismatch between substrate and film has been found to play a lesser role in epitaxial growth than substrate temperature. Clearly, mobile nuclei which rotate until their planes line up or growing nuclei which melt together favor epitaxial growth[2.1]. Therefore, plasma excitation in combination with thermal energy can advantageously contribute to epitaxial growth, providing the bombardment process does not induce lasting defects. One strategy to manage plasma induced defects is to anneal them out at a faster rate than they are created, so a careful balance between plasma excitation and thermal energy is important.

2.9 Conclusion

For the most part, the Volmer–Weber 3–D condensation, nucleation, growth, and coalescence model handles thin film growth adequately. There are some exceptions to this rule, but these films conform to no other competing models, so fundamental research must be done to propose new mechanisms. As we have seen, plasmas have enhanced the degrees of freedom within the CVD domain in terms of source materials and surface excitation. In addition, research should be done to couple reaction kinetics to phase transformation, in order to fully appreciate the growth process.

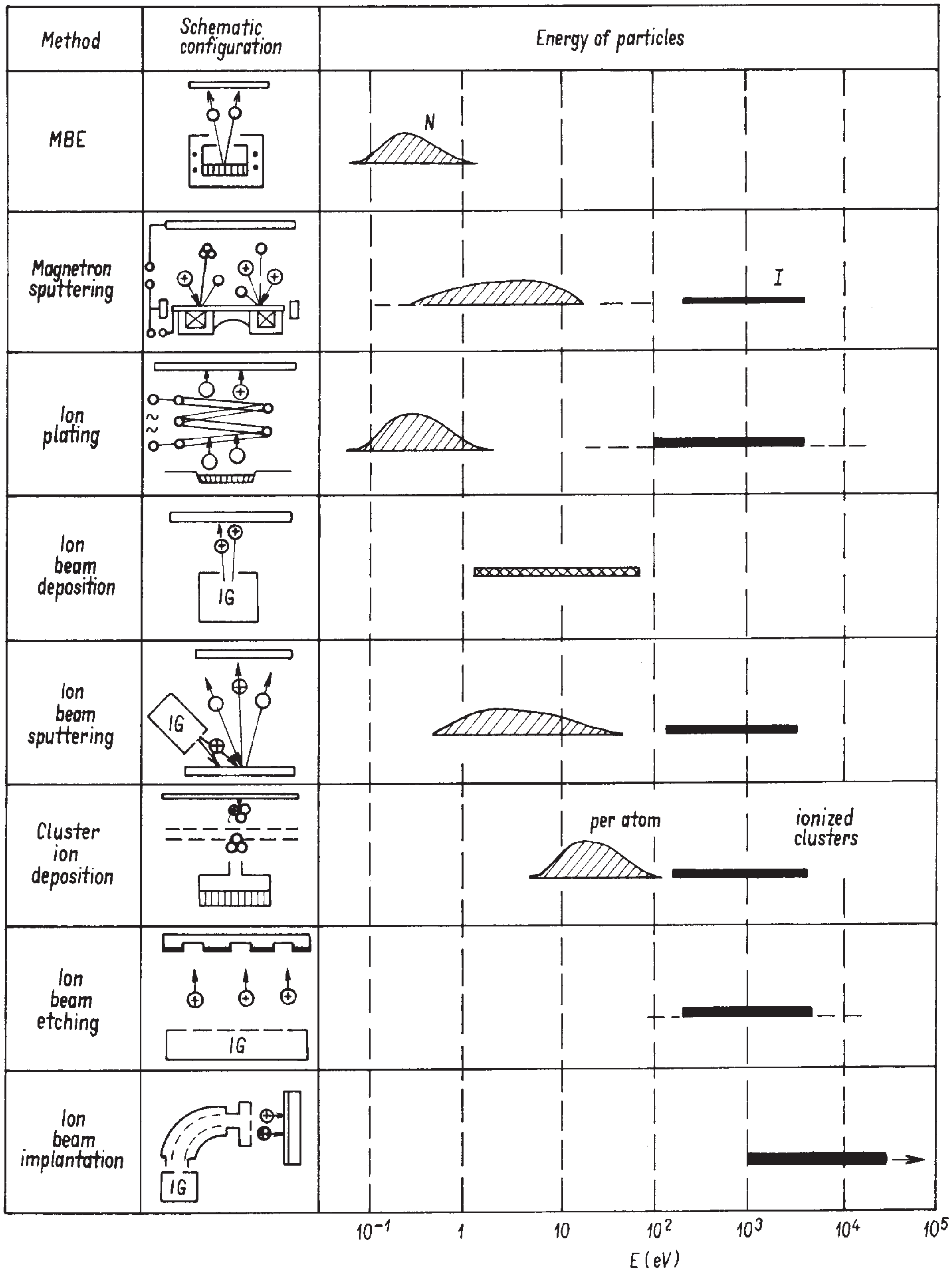

Figure 2.1: Deposition methods using ions (N = neutrals, I = ions).

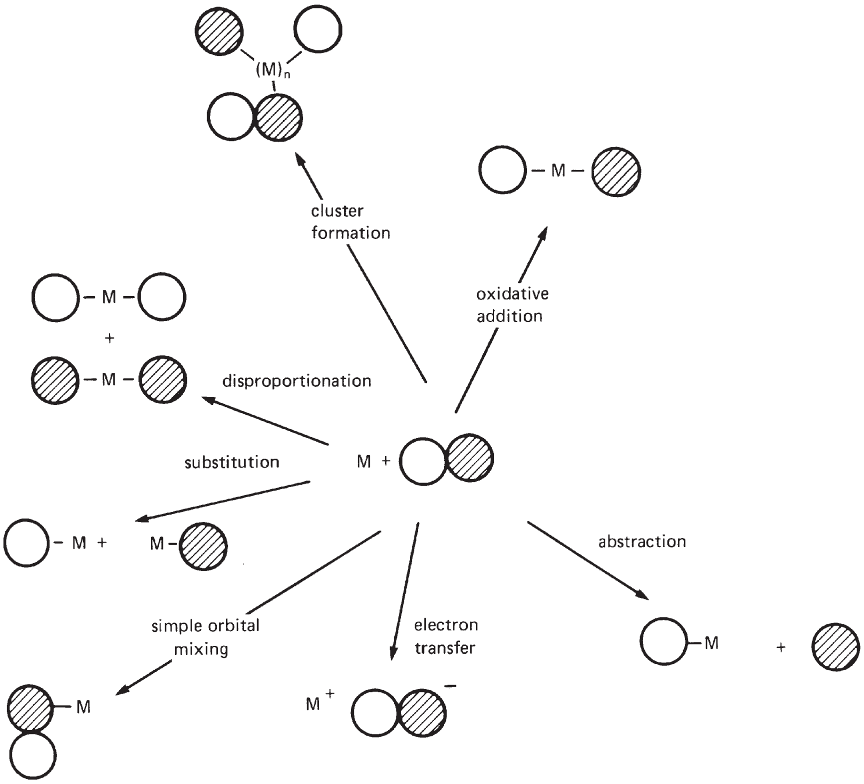

Oxidative addition:

$$Ni + C_6F_5Br \longrightarrow C_6F_5{-}Ni{-}Br$$

$$SiF_2 + C_6F_6 \longrightarrow C_6F_5SiF_3$$

Electron transfer:

$$Li_{atom} + (NC)_2C{=}C(CN)_2 \longrightarrow Li^+(NC)_2C{=}(CN)_2^-$$

Abstraction:

$$Ag_{atom} + CF_3I \longrightarrow AgI + CF_3$$

Simple orbital mixing:

$$Cr_{atom} + C_6H_6 \longrightarrow (C_6H_6)_2Cr$$

benzene sandwich compound

Substitution:

$$2Ag_{atom} + (CF_3)_2CFI \longrightarrow AgI + AgCF(CF_3)_2$$

Disproportionation and ligand transfer:

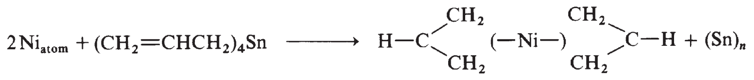

$$2Ni_{atom} + (CH_2{=}CHCH_2)_4Sn \longrightarrow H{-}C\begin{matrix}\diagup CH_2 \\ \diagdown CH_2\end{matrix}\;({-}Ni{-})\;\begin{matrix}CH_2 \diagdown \\ CH_2 \diagup\end{matrix}C{-}H + (Sn)_n$$

Cluster formation [16]:

$$Mg_{atom} + Mg_{atom} \longrightarrow Mg{-}Mg \xrightarrow{CH_3Br} CH_3MgMgBr$$

Figure 2.2: Reaction chemistry of free atoms.

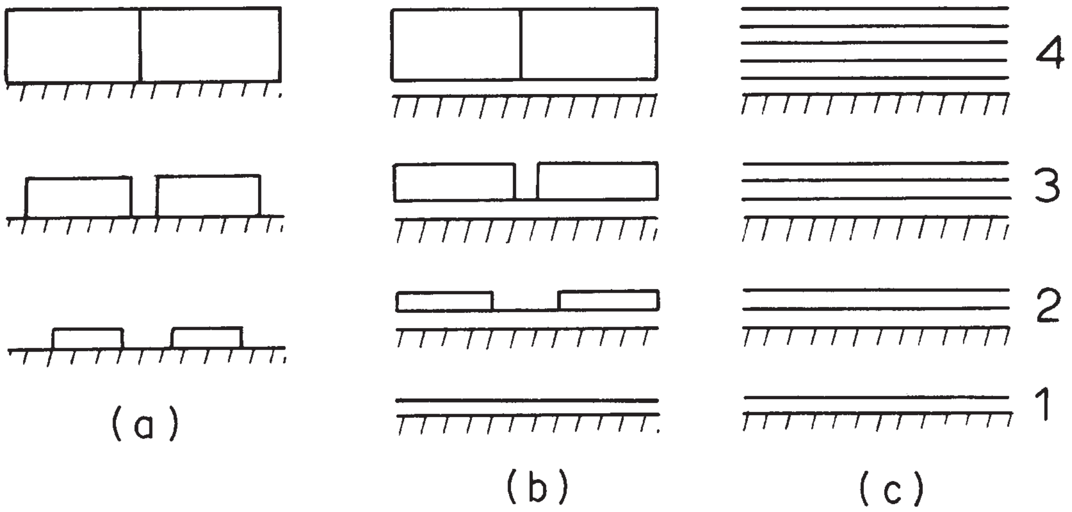

Figure 2.3: Growth models: (a) Volmer–Weber, (b) Stranski–Krasonov, and (c) van der Merwe.

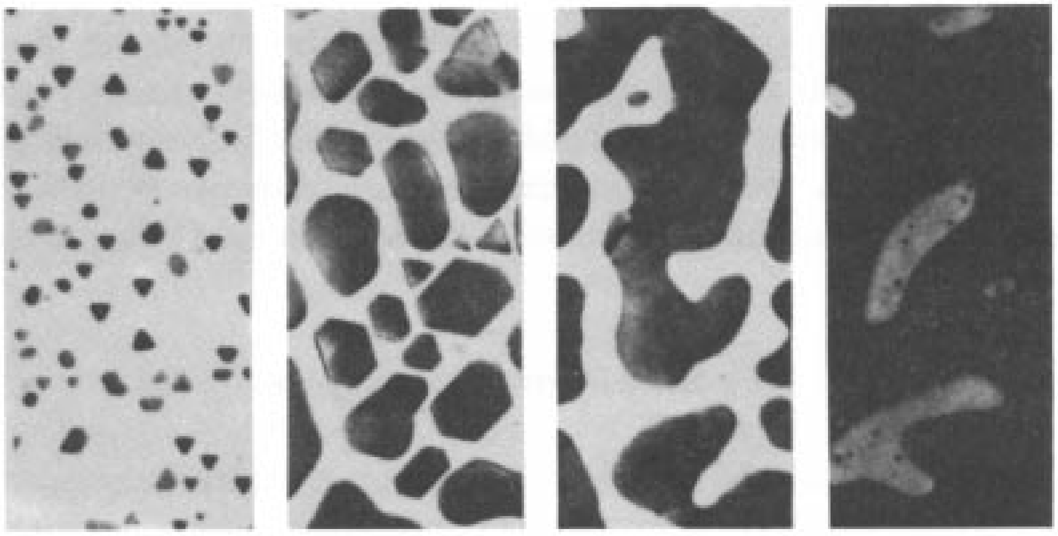

Figure 2.4: Formation stages of Ag film on MoS_2.

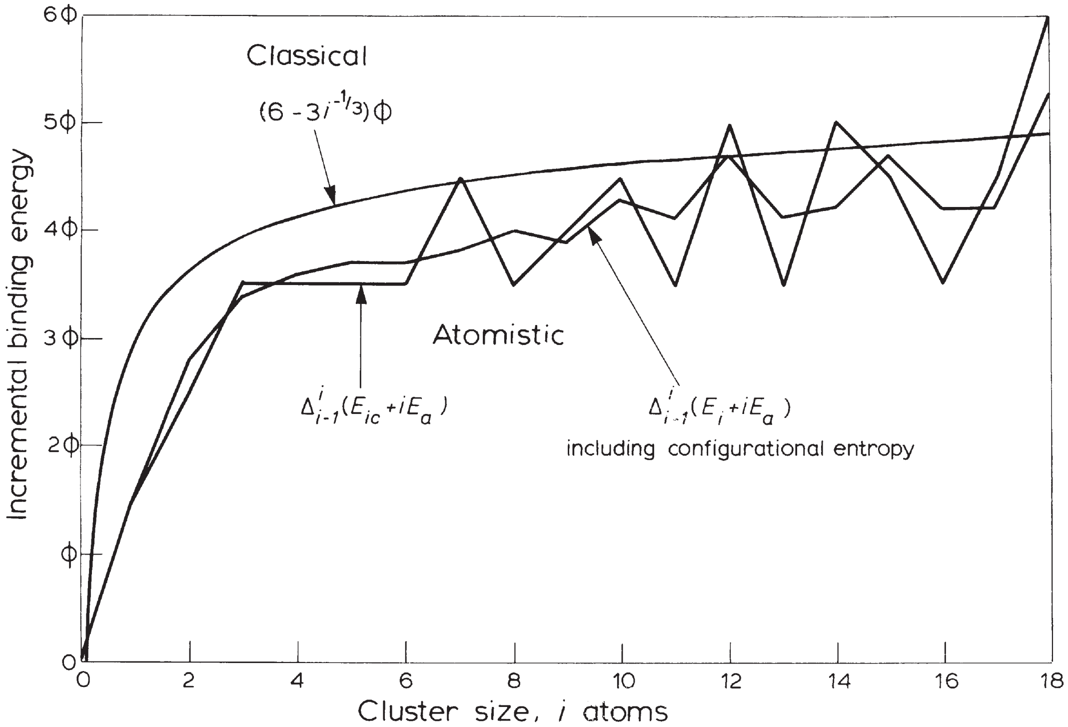

Figure 2.5: Comparison of classical (heterogeneous) and atomistic nucleation models.

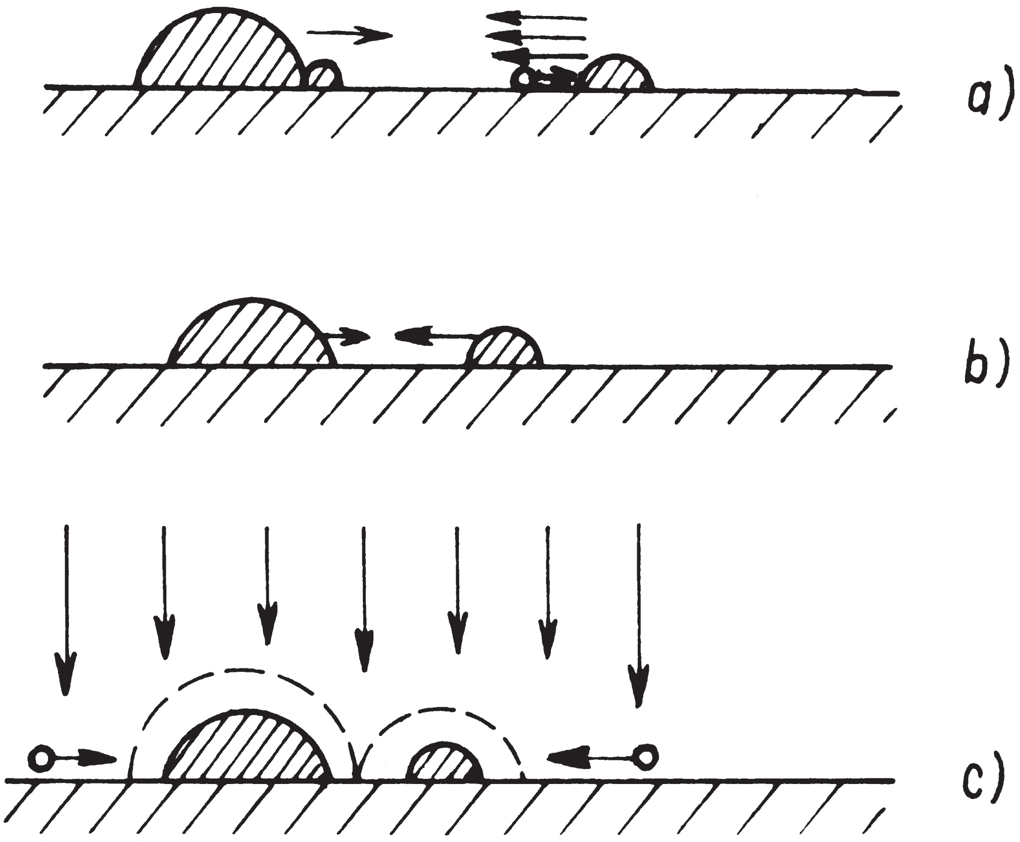

Figure 2.6: Coalescence mechanisms: (a) Ostwald ripening, (b) cluster mobility, and (c) growth coalescence.

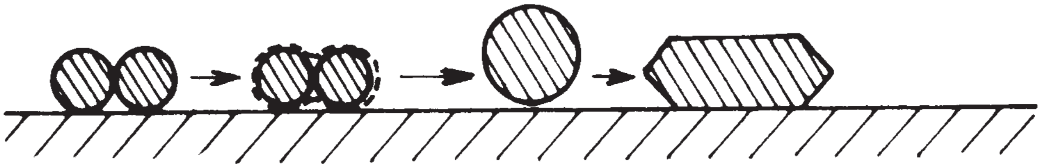

Figure 2.7: Coalescence of the islands and subsequent crystallization.

References

[2.1] L. Eckertova, *Physics of Thin Films*, Plenum: New York (1986).

[2.2] B. Lewis and J. C. Anderson, *Nucleation and Growth of Thin Films*, Academic Press: New York (1978).

[2.3] K.Klabunde, ed., *Thin Films from Free Atoms and Particles*, Academic Press: New York (1985).

[2.4] L. I. Maissel and R Glang, eds., *Handbook of Thin Film Technology*, McGraw–Hill: New York (1970).

[2.5] D. A. Porter and K. E. Easterling, *Phase Transformations in Metals and Alloys*, Van Nostrand Reinhold: Wokingham, Birkshire, UK (1981).

3

Plasma Processes

3.1 Introduction

Plasmas are taking on an increasing role in the research environment for the production of powders, whiskers, and thin films. As plasmas become more popular, traditional thermal chemistry is being abandoned, despite its well understood and controllable chemical mechanisms. If thermal chemistry is so well established, why are people shifting to plasma chemistry, which represents nonequilibrium conditions and less control? Let's explore the nature of plasmas in more detail.

3.2 Definitions

Plasma assisted chemical vapor deposition(PACVD) implies the formation of solid/vapor products from volatile reactants in the presence of an electrical discharge. Volatile reactants in an electrical field contain energetic neutrals, ions, and electrons. At high pressure, atmospheric or greater, the collision frequency is so great that the neutrals, ions, and electrons have about the same energy, and therefore defined as being in thermal equilibrium. Below atmospheric pressure, collision frequency decreases, so electrons which absorb the electric field energy most efficiently, are unable to transfer their energy to neutrals and ions. Plasmas having unequal energy distributions among the particles are called non–equilibrium or “cold” plasma discharges[3.1].

3.3 Kinetics

The primary advantage of plasma CVD over thermal CVD is the ability to deposit films at relatively low substrate temperatures. This may not seem too advantageous in itself; however, the consequences of low temperature growth are numerous. Energy input to the system can be substantially reduced because energetic electrons activate reactions in the gas phase and on the substrate surface, which normally would only occur through thermal pathways. Stress, induced by thermal expansion coefficient mismatch between substrate and film, can be minimized, because the differential between growth temperature and room temperature is reduced. High temperature CVD processes are also unacceptable for materials which would melt or decompose at thermal reaction temperatures. For in–situ device growth, minimizing substrate temperature is vital to preventing diffusional dopant cross contamination. One drawback to PACVD is that deposition of pure materials is virtually impossible. Desorption of product gases on the "cold" film surface is ineffective, resulting in films containing these impurities[3.1]. In the case of amorphous silicon,

$$SiH_4(g) \rightarrow a-Si(s) + H_2(g)$$

atomic hydrogen incorporated in the film as a–Si:H is believed to be helpful in reducing the number of defects.

Collisional dissociation of reactants by electrons in a glow discharge occur even when the reactants are thermally stable at the deposition temperature. A typical mechanism for reactant dissociation by energetic electrons can be viewed as follows:

$$RX + e^- \rightarrow R + X + e^-$$

3.4 Plasma Types

Originally, I planned to limit my discussion of plasmas to alternating current(AC) glow discharge systems, based on its popularity for plasma CVD. However, as I reviewed other plasma articles, it became clear that any AC plasma explanations involved analogies comparing AC systems to direct current(DC) or magnetron sources. Therefore, this section presents a comprehensive overview of: DC, magnetron, radio frequency(RF), and microwave(MW) plasmas, to lay the groundwork for future topics in this paper.

A direct current plasma relies on ion bombardment of the cathode which ejects secondary electrons. These secondary electrons are accelerated by the electric field away from the cathode dark space into the negative glow region. Once these high energy electrons enter the negative glow region, they become primary electrons until they lose their energy to collisions with neutral atoms, causing ionization. After these primary electrons expend their energy in the negative glow region through collisions, they are defined as ultimate electrons. Ultimate electrons either recombine in the negative glow region or migrate to the wall. Figure 3.1 schematically represents the cyclical process. Primary electrons can also migrate to the wall without dissipating their energy, so a variation to the parallel plate version of DC glow discharge is a hollow tube cathode illustrated in figure 3.2. In this configuration, electrons repelled by the cathode have a greater chance of ionizing collisions until they migrate to the wall or recombine[3.3].

Let's talk about the regions in a DC discharge in more detail. We have a cathode dark space, where high energy ions and secondary electrons exist. The high energy ions dissipate their energy by colliding with the cathode and ejecting secondary electrons. The secondary electrons get swept away and accelerated by the electric field into the negative glow region to become primary electrons. The negative glow region contains primary electrons, ultimate electrons(primaries after collision), and low energy ionization products(ions & electrons). The high energy ions leave the negative glow region to collide with the cathode. Between the negative glow and the anode lies the positive column, where there is an equal number of electrons and ions. Note, however, that this charge balance is dynamic rather than static. The positive column is the region where the electric field is sufficient to transport the discharge current from the negative glow to the anode, where ionization balances wall losses. One last point, in practice, the positive column does not exist, because the anode intercepts the plasma in the negative glow region, due to the small anode to cathode spacing[3.3].

Magnetron discharges have a barbell shaped cathode surrounded by a magnetic field as shown in figure 3.3. An anode ring can be found on one or both ends of the cathode. Magnetrons have higher ionization cross sections than hollow cathodes, because the electrons are surrounded—by the cathode at the center and both ends, and by a magnetic field on the outer shell. Figure 3.4 demonstrates how electrons behave under the influence of magnetic and electric fields. Electrons which have low energy relative to the electric field have a cycloidal motion like that shown in image d; whereas, electrons having higher energy than the electric field take on a circular motion in addition to the cycloidal motion which translates into a helical motion, depicted in image e. Thus, magnets not only confine electrons, but also enhance ionization cross sections by inducing cyclical paths, which increase collisions over comparable straight paths.

Radio frequency glow discharge applicators come in three varieties: i) parallel plate, ii) clam shell, and iii) coil type, all illustrated in figure 3.5. Contrary to popular belief, all three applicators are primarily capacitively coupled. The coil type does have an inductive component; however, the capacitance between adjacent coils predominates over inductance unless the user makes a special effort to shield capacitive effects[3.3]. Matching networks, a subject to be covered in more detail later, maximize the power coupled to the system. Electrodes are possible in the radio frequency range, because there are currently high power switching devices that operate up to the RF frequency.

Generally, the most popular RF frequency for plasma CVD is 13.56 MHz, which happens to be the only frequency allocated by the FCC for industrial applications in the 10 to 20 MHz band. At this frequency, only electrons have the mobility to follow the oscillating electric field in a sea of stationary ions. As the electron cloud approaches one electrode, it uncovers ions at the other electrode forming a temporary ion sheath which we called the cathode dark space in DC discharge. This ion sheath creates an electric field which accelerates the ions toward the electrode to generate secondary electrons. Since both electrodes take on the role of the cathode for a fraction of the time and ions are oblivious to the electric field oscillations, most people attribute the more effective ionization cross sections of RF over DC to this dual cathode model[3.3].

Microwave plasma applicators come in two forms depicted in figure 3.6. Unfortunately, no high power devices can oscillate in the microwave frequency, so microwaves have to be induced in a magnetron tube, then transported from the magnetron source to the plasma applicator in a waveguide. These complications boost the price of a MW source 5 to 10 times the cost of a direct RF source. Hopefully, someday we will have high power microwave devices to allow direct MW application, as in the RF case.

The traditional microwave applicator, figure 3.6a, was a circular silica tube intersecting a rectangular waveguide in a perpendicular fashion. This method limited the plasma region to about 1” diameter due to the physical dimensions of the 2.45 GHz waveguide. Waveguide dimensions are dictated by Maxwell equations for single mode wave propagation, but as a general rule, come close to the microwave wavelength[3.4]. Provisions for substrate heating or cooling on this scale are nearly impossible, so substrate temperature is strictly dependent on microwave power and chamber pressure. In addition, the plasma is in close proximity to the silica walls, which can be etched away and contaminate the growing film.

The newer microwave applicator overcomes this 1” diameter limitation by introducing the microwave directly into the plasma chamber through a window, as shown in figure 3.6b. This large area microwave applicator can accommodate samples up to 4” diameter, allows independent control of substrate temperature by means of a heater, and limits film contamination to sample holder etch. There are actually three different ways to operate this plasma cavity: i) high pressure non–magnetic, ii) low pressure electron cyclotron resonance(ECR), and iii) magneto assisted high pressure, each of which will be discussed individually in the next few paragraphs.

i) At high pressures(.01 to 100 torr), electron density is high enough to sustain a glow discharge without the aid of magnets; however, chamber geometry has to be strictly controlled to form a resonant cavity for microwaves.

ii) For lower pressures(.001 to 1 torr), magnets keep electron density high enough so that the microwaves dissipate all their energy in one pass, so chamber geometry is less important. Design of this cavity makes use of a carefully matched magnets which cause the electrons to resonate in a cycloidal or a helical frequency the same as the microwave frequency. Electrons absorb energy most efficiently from the electric field at their cyclotron resonance frequency[3.5]. Consequently, ionization cross sections are enhanced by electron gyrations and efficient coupling between electrons and the electric field.

iii) A hybrid between the first two cases combines the magnetic field with high pressures. Above 1 torr, the radius of electron gyration is greater than the path length, so ECR no longer predominates. Hence, ionization cross sections are only influenced by electron gyrations, similar to the DC magnetron source.

3.5 AC Characteristics

This section deals with understanding why alternating current glow discharges are used, why self bias occurs, how matching networks couple power to the plasma, and how to choose the right frequency.

Although AC plasmas have better ionization cross sections than DC, there is a stronger motivation for using AC plasmas. For the discussion involving DC plasmas, we assumed that the deposition material was electrically conductive. Let’s see what happens if we try to grow an insulating film in a DC plasma. Initially, the insulating material will drop to $-V_S$, the supply voltage. The glow discharge will be initiated and the film will begin to be bombarded by positive ions. The film will start to charge positively, because electrons in the film escape to neutralize the ions. (If a conducting film were present, these electrons would be replenished by the DC circuit.) As the film charges positively, it approaches zero potential extinguishing the plasma. This whole scenario is displayed graphically in figure 3.7 [3.6]. In light of this information, it concerns me how people obtain diamond films using DC or hollow cathode methods, since a 5 eV band gap is essentially an insulator material, unless a graphitic component provides the necessary conductance.

The only solution to this charging effect is to use alternating current, where the net charge flow is zero, but what frequency? To answer that question, we must estimate how long it takes to charge up an insulating surface:

$$C = \frac{Q}{V} = \frac{it}{V}$$

$$t = \frac{CV}{i}$$

$$f = \frac{1}{t}$$

where: C = *capacitance* = *1 pF/cm*^{2} *(quartz)*
Q = *stored charge*
V = *applied voltage* = *1000 V* *(typical)*
i = *ion current density* = *1 mA/cm*^{2} *(typical)*
t = *charging time* = *1* μ*s*
f = *frequency* = *1 MHz*

Thus, for SiO_2(quartz) growth, if a frequency much less than 1 MHz is used, the film will be charged up most of the time, and a plasma will be present only a small fraction of the time. This more adequately explains why 13.56 MHz is very popular for insulator deposition[3.6].

A negative bias voltage is imposed on a floating potential film during growth. Figure 3.8 attempts to illustrate this point. Isolated objects with a floating potential can't draw current. So if we introduce a floating potential surface to an AC plasma, the electron flux will initially be greater than the ion flux, based on mobilities. As the electrons build up, a negative bias appears. The negative bias starts to repel the electrons, reducing the electron flux. This bias continues to grow until steady state conditions are met: electron flux = ion flux, so that the net current balances to zero[3.6].

Matching networks are most easily understood by considering a DC plasma equivalent circuit like the one shown in figure 3.9. The objective of a matching network is to maximize the power delivered to the plasma discharge. If we take an expression for power, differentiate that expression, set the differential equal to zero, a relationship should emerge to show what conditions will maximize power:

$$P = IV$$

$$V = IR$$

$$P = I^2R$$

$$I = \frac{V}{(r + R)}$$

$$P = \frac{V^2R}{(r + R)^2}$$

$$\frac{dP}{dR} = \frac{V^2(r + R)^2 - 2(r + R)V^2R}{(r + R)^2}$$

where: P = *power delivered to load (plasma & matching network)*
I = *total current*
V = *voltage drop across load*
R = *load resistance*
r = *internal resistance*

Therefore, dP/dR = 0 if r = R. This explanation can be extended to AC plasmas if r is replaced by z=a+jb and R is replaced by Z=c+jd to account for capacitive and inductive loads. To maximize power in the AC case, Z(load impedance) should be the complex conjugate of z(internal impedance). That is, if z=a+jb, then maximum power will be delivered to the plasma when Z=a–jb [3.6].

The closing paragraphs deal with comparing RF to MW plasmas. Although there don’t appear to be any definitive answers, the results give some insight to the general trends. The two approaches used so far include: i) a mathematical model by Ferreira and Loureiro[3.7] and ii) a surface wave experiment by Claude, et al[3.8]. In the comparison of plasmas, the v/w ratio separates the RF from the MW regime, where v is the average electron–neutral collision frequency, and w is the wave angular frequency: $w = 2\pi f$.

Theoretical modeling of argon plasmas has produced electron energy distribution curves such as figure 3.10. RF and MW domains differ significantly in that MW (v/w < 1) has maxwellian behavior whereas RF (v/w > 1) displays non–maxwellian behavior. Additionally, the RF is richer in low energy electrons but deficient in high energy electrons. MW has a lower average electron energy but a long high energy electron tail. Despite its lower average electron energy, the energy is spread out over more electrons; therefore, MW has higher ionization cross sections. Also, the high energy electron tail may enhance deep UV emission[3.7].

Traditionally, RF and MW plasmas could not be compared experimentally due to differences in power densities characteristic of the excitation source geometry. Then, Claude, et al. devised a standing wave tube where wave launchers could emit frequencies in the range 12 to 400 MHz cutting across the RF/MW regime where excitation frequency was the only variable. Curves displaying growth rate versus frequency for constant power input looked like figure 3.11. The upper curve is a hydrocarbon gas whereas the lower curve is a fluorocarbon gas. Differences in growth rate for RF versus MW domains ranged from 3 to 5 times higher for microwave frequencies; however, plateaus existed in both regimes, indicating frequency may not be as important as regime. Note the fluorocarbon gas did not exhibit the low frequency plateau, although no explanation was given. The authors did account for the differences in film growth rate between the hydrocarbon and fluorocarbon gas sources due to electron binding energy differences; fluorocarbon has stronger electron attachment and thus lower growth rate[3.8].

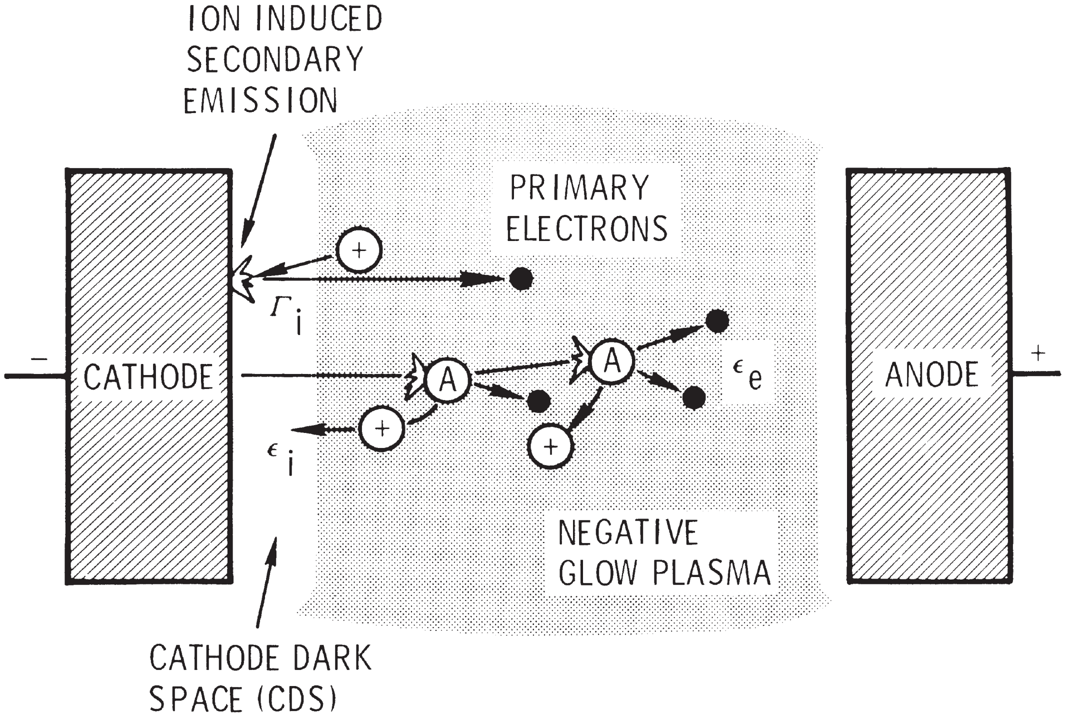

Figure 3.1: Schematic illustration of DC discharge.

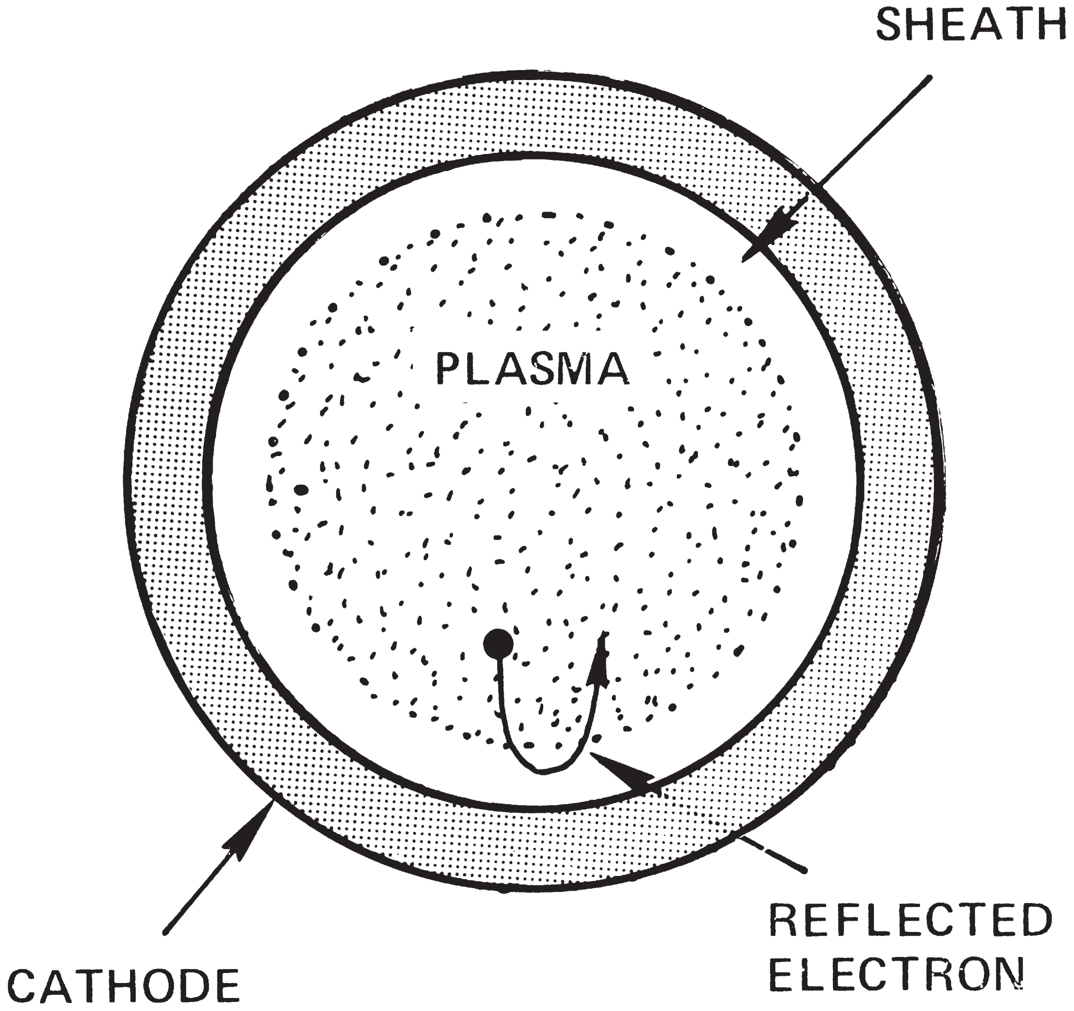

Figure 3.2: Hollow cathode discharge.

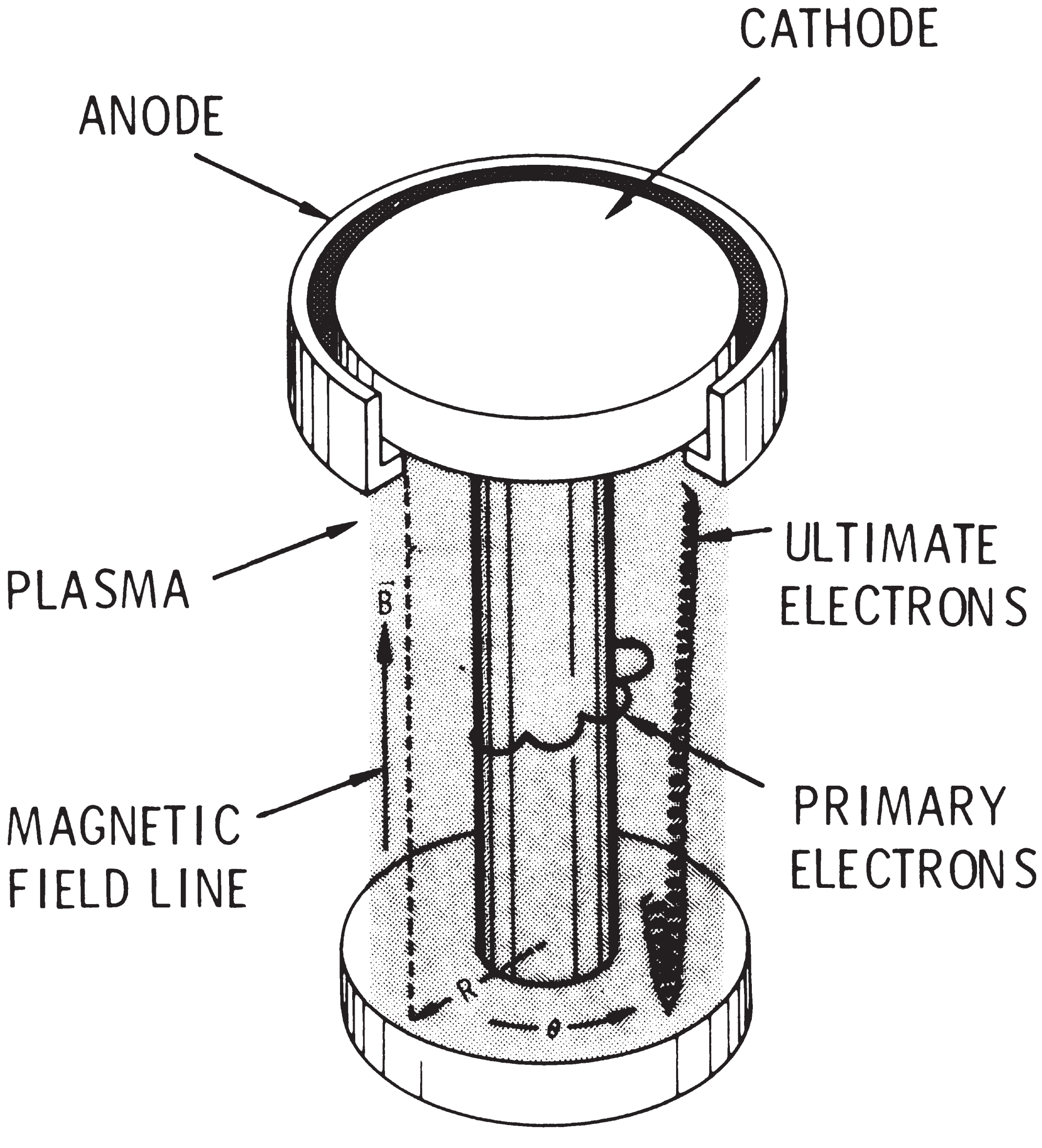

Figure 3.3: Cylindrical–post magnetron sputtering source.

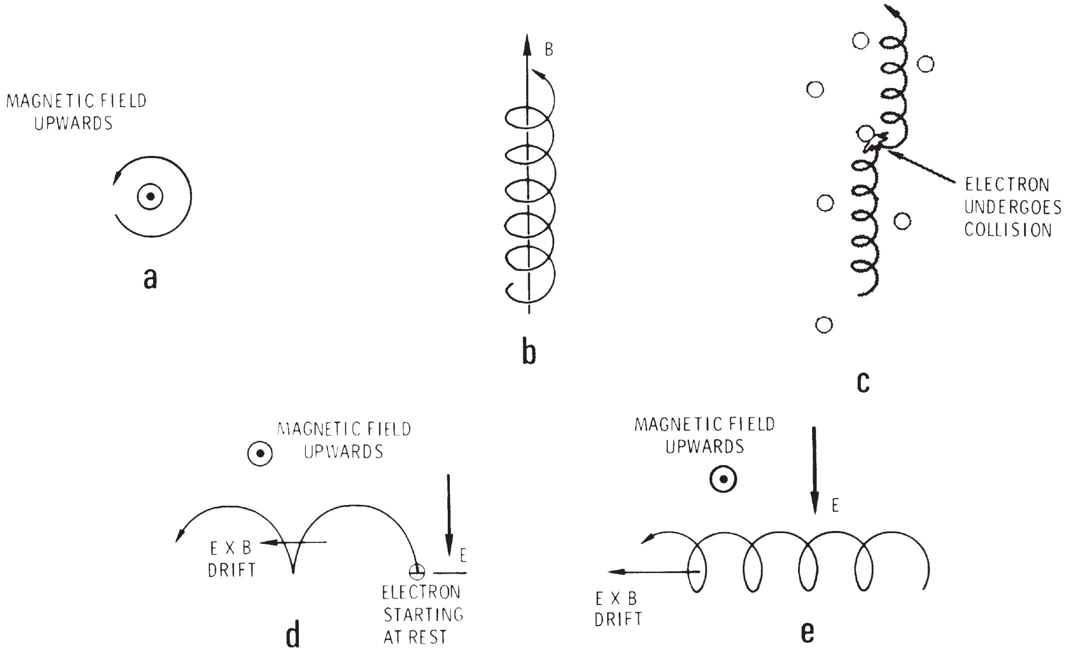

Figure 3.4: Electron motion in static magnetic and electric fields.

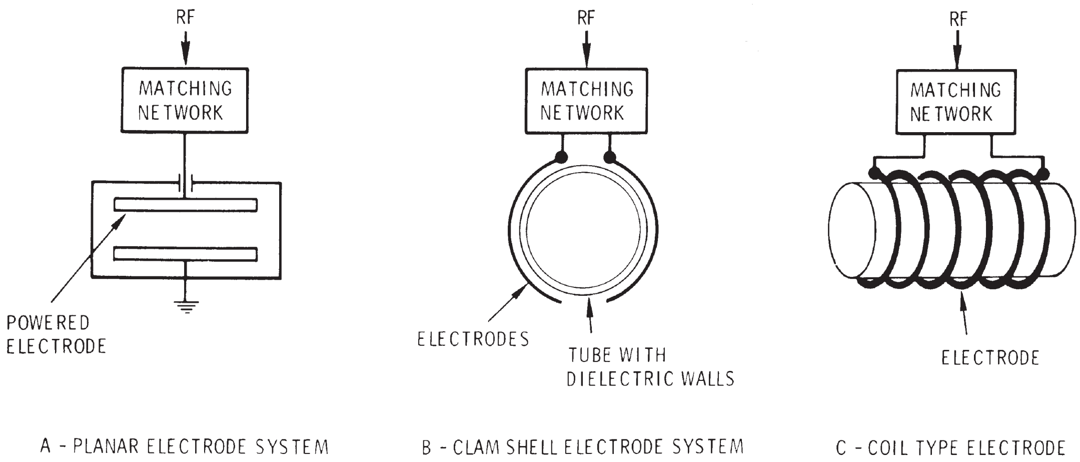

Figure 3.5: Commonly used RF plasma discharge devices.

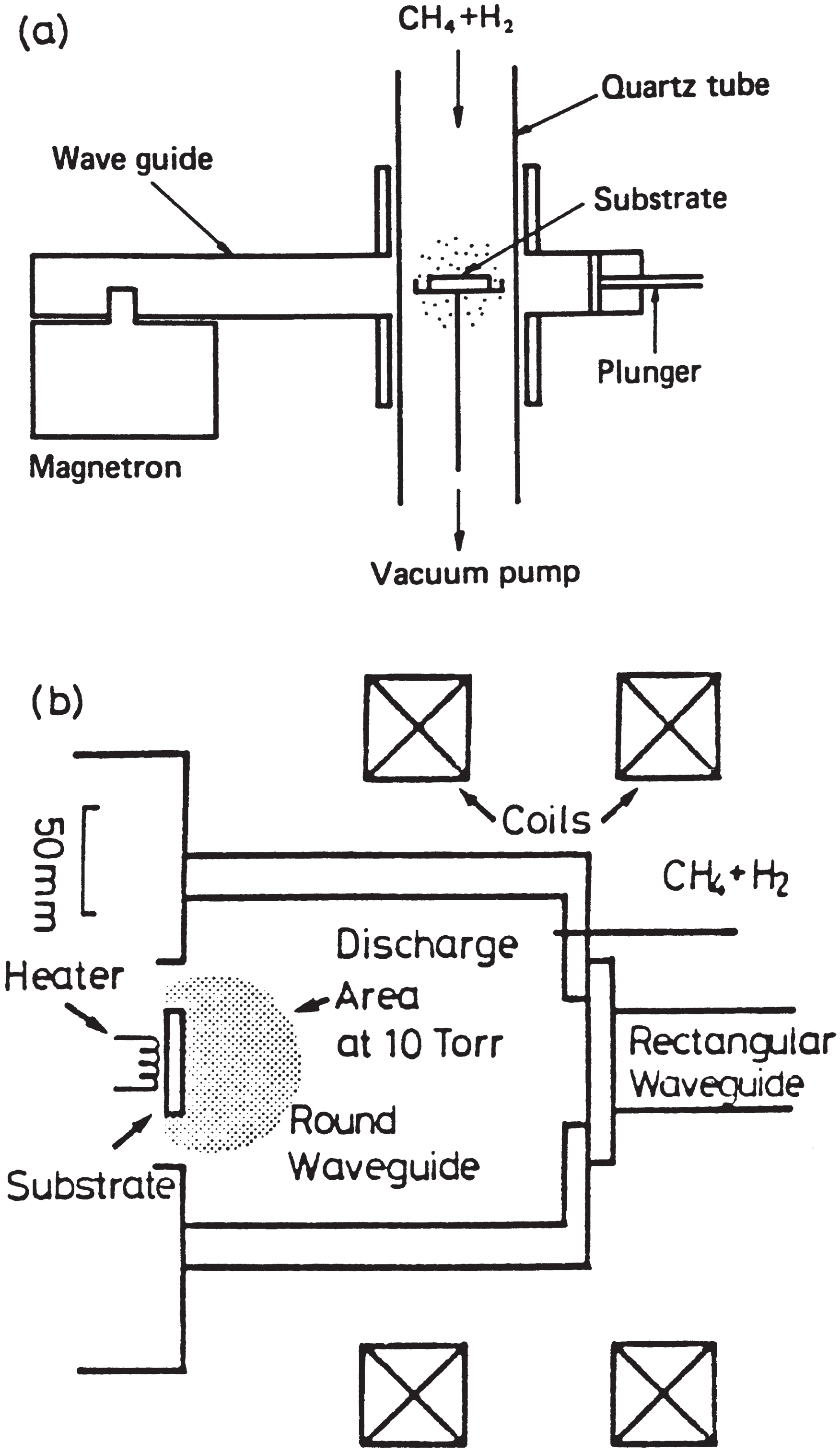

Figure 3.6: Microwave plasma applicators; (a) traditional and (b) large area.

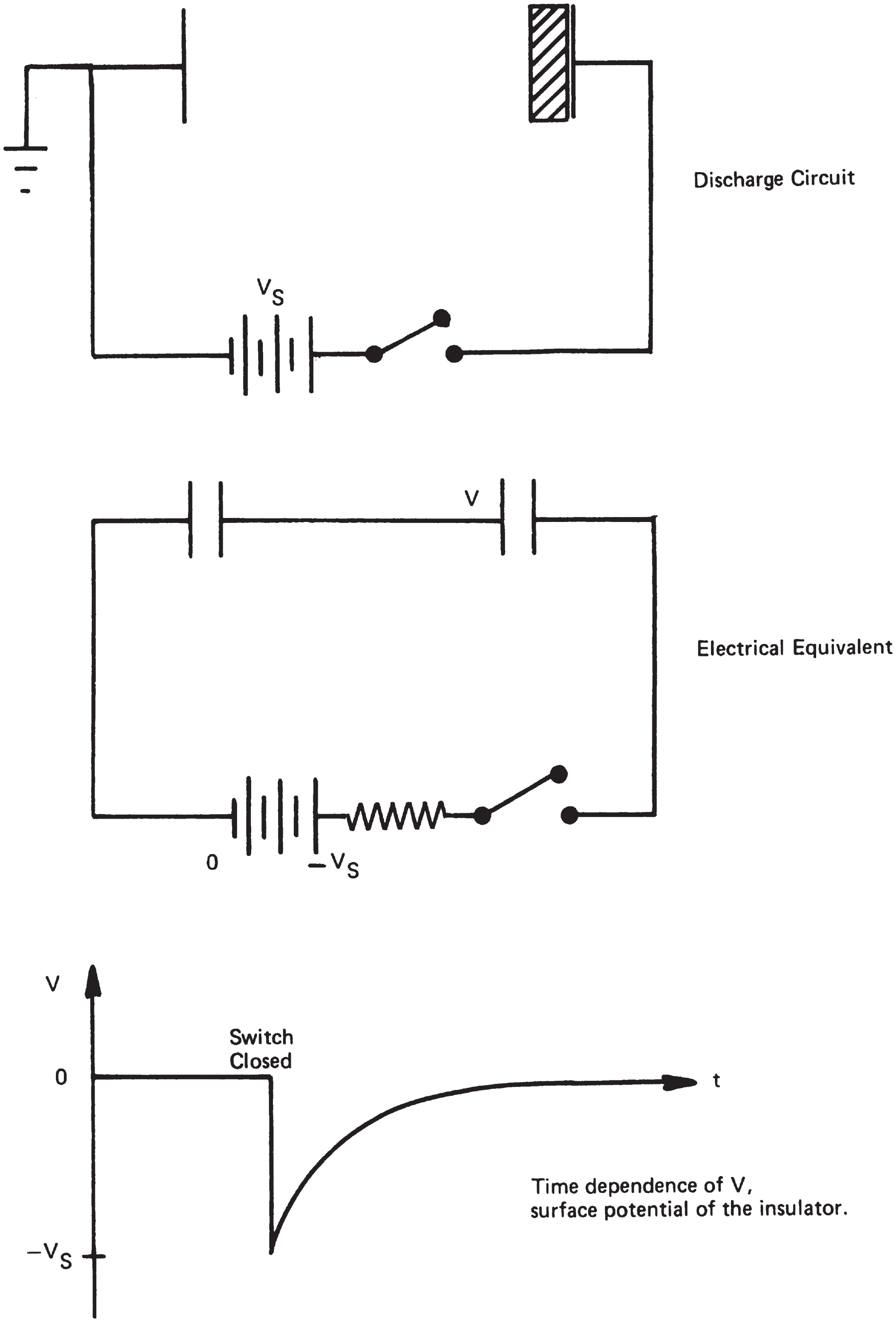

Figure 3.7: Surface charging of an insulating cathode.

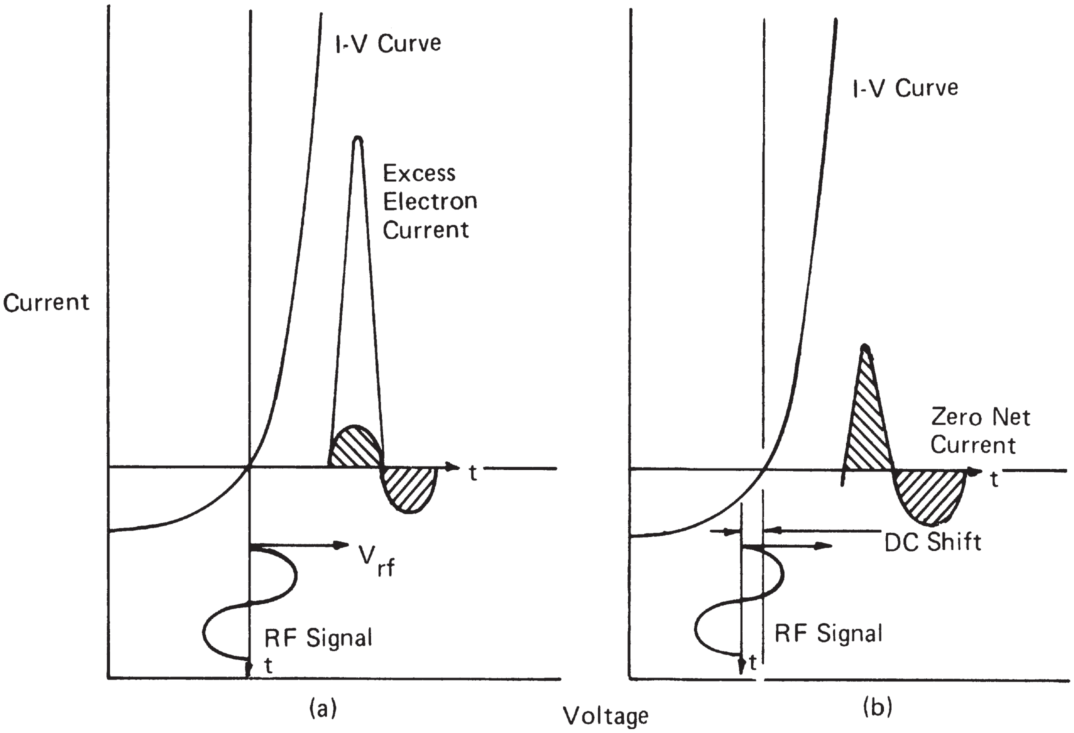

Figure 3.8: Self–biasing of a floating potential surface.

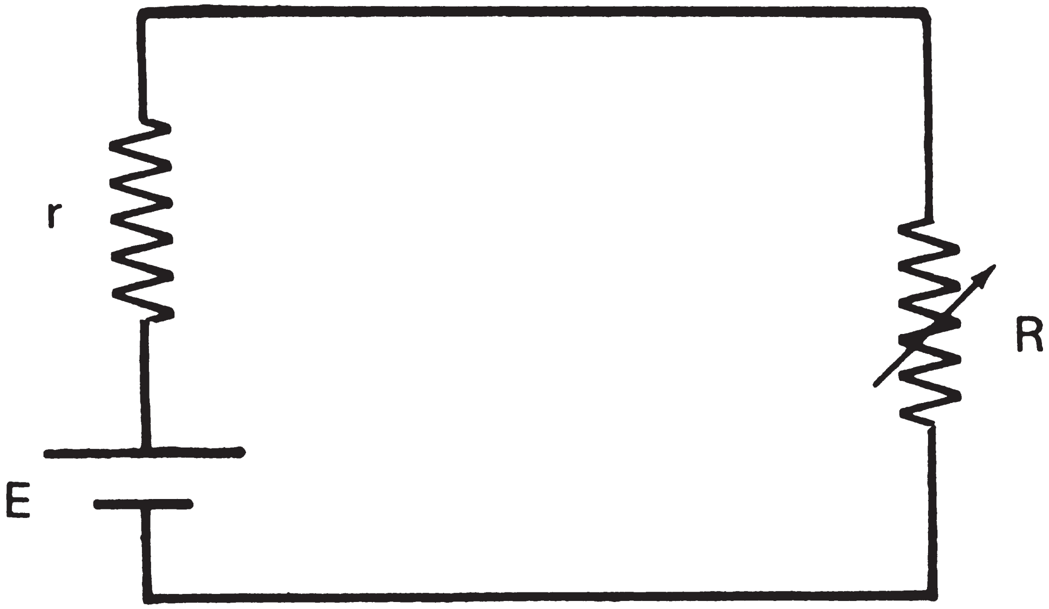

Figure 3.9: DC plasma equivalent circuit.

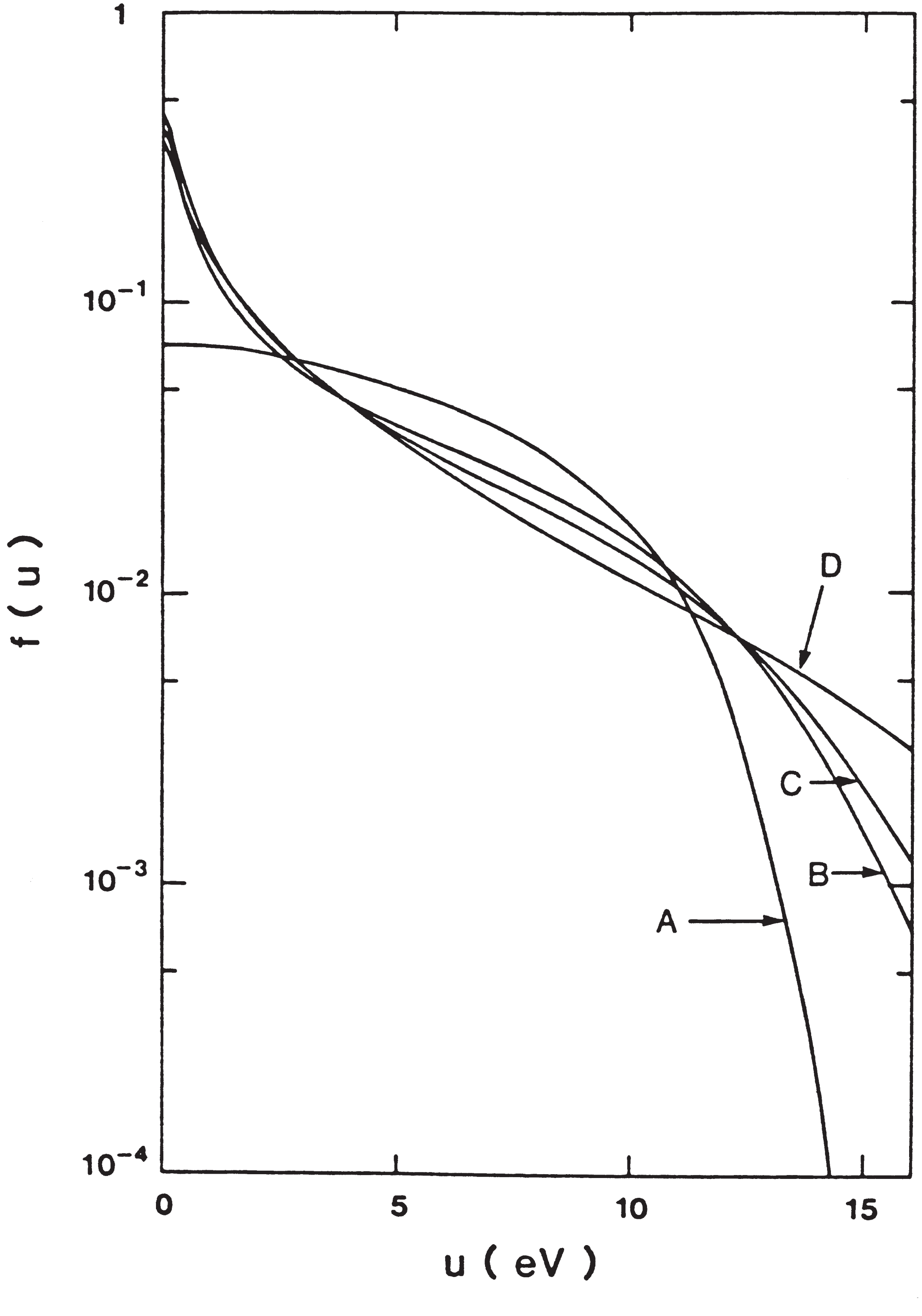

Figure 3.10: Electron energy distribution function vs. electron energy; (a) RF, (b)–(c) intermediate frequencies, and (d) MW.

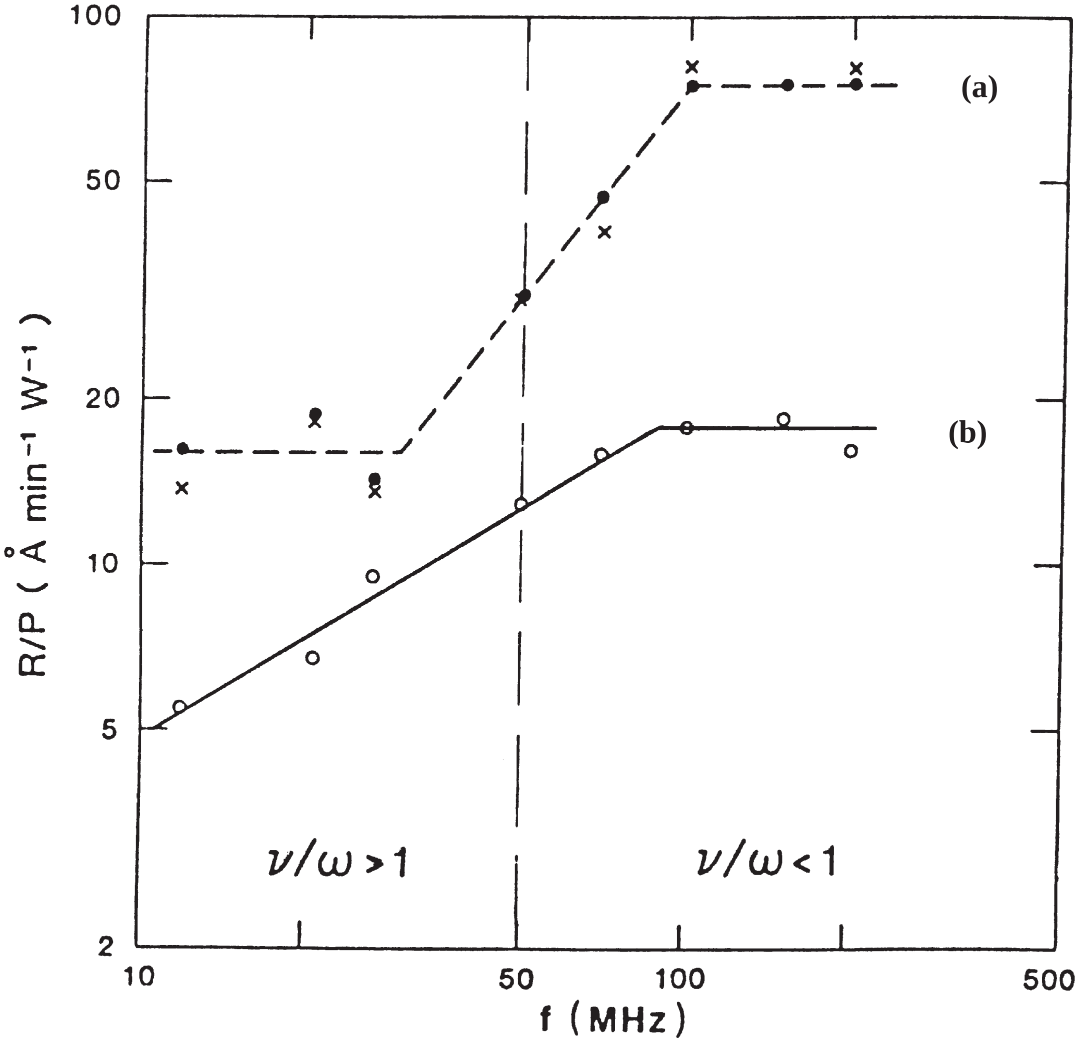

Figure 3.11: Growthrate/power absorbed vs. excitation frequency; (a) hydrocarbon gas and (b) fluorocarbon gas.

References

[3.1] T. D. Bonifield, in *Deposition Technologies for Films and Coatings*, R. F. Bunshah, ed., Noyes: Park Ridge, NJ (1982), Ch. 9.

[3.2] J. H. Comfort, L. M. Garverick, and R. Reif, *Journal of Applied Physics*, **62**, 3388 (1987).

[3.3] J. A. Thorton, in *Deposition Technologies for Films and Coatings*, R. F. Bunshah, ed., Noyes: Park Ridge, NJ (1982), Ch. 2, 5.

[3.4] A. L. Van Koughnett, *Transactions of the International Microwave Power Institute*, **1**, 17 (1973).

[3.5] M. Kitagawa, et al., *Journal of Applied Physics*, **61**, 2084 (1987).

[3.6] B. N. Chapman, *Glow Discharge Processes*, Wiley: New York (1980), Ch. 5.

[3.7] C. M. Ferreira and J. Loureiro, *Journal of Physics*, **D17**, 1175 (1984).

[3.8] R. Claude, et al., *Plasma Chemistry and Plasma Processing*, **7**, 451 (1987).

4

Laboratory Background

4.1 Introduction

Although this chapter started out as a review of literature within our research group, I stumbled across some provocative data in Jim Kelliher's PhD thesis, that needed a little further interpretation. Our lab has taken on the challenge of compound semiconductor synthesis using metalorganic precursors, in parallel to novel in situ optical monitoring schemes, with an eye towards surface driven process control. Traditionally, people have relied on more remote sensing parameters, such as: pressure, temperature, mass flow control, and even thickness measurements as a means of controlling film properties. If one had a real time sensor to evaluate surface chemistry features, then an opportunity exists to modify those features before they become archival defects in the growing crystal lattice. More specifically, GaP heterostructure molecular beam growth and plane–polarized reflectance spectroscopy, will be the focus of this chapter. Rather than reveal any details of my discovery here, I'll let the story unfold for you, as the pieces of the puzzle fell together for me.

4.2 GaP Heteroepitaxy

The motivation for growing GaP on Si substrates is to achieve dielectric isolation between Si layers and grow nonlinear optics such as $ZnGeP_2$ on Si/GaP/Si/GaP... superlattices. The crystal structure of Si is a diamond cubic lattice, which is described as two face centered cubic (FCC) lattices displaced by a 1/4 unit body diagonal. For GaP, it has zinc blende cubic structure, which corresponds to a Ga FCC lattice interwoven with a P FCC lattice, separated by the 1/4 unit body diagonal. What makes Si/GaP even more attractive as a heterostructure is a lattice mismatch of only 0.4% at room temperature:

Property	Si	GaP	unit
Lattice Constant @ 300 K	5.431	5.451	Å
Thermal Expansion Coefficient	2.33	5.3	x 10^{-6}/C

However, GaP’s thermal expansion coefficient is more than double Si’s, so low temperature processing is essential in preserving crystal quality[4.1].

To grow GaP, triethylgallium (TEG) and tertiarybutylphosphine (TBP) are chosen as precursors on the III–V sides, respectively, so in molecular beam terminology, it’s viewed as chemical beam epitaxy (CBE). In general, metalorganics provide lower vapor pressure, less toxicity, and reduced growth temperatures relative to pure metals or hydride gas sources[4.1].

Triethylgallium decomposes in a successive ethyl elimination steps[4.2]:

$$Ga(C_2H_5)_3 \leftrightarrows Ga(C_2H_5)_2\cdot + C_2H_5\cdot$$

$$Ga(C_2H_5)_2 \leftrightarrows GaC_2H_5\cdot + C_2H_5\cdot$$

$$GaC_2H_5\cdot \leftrightarrows Ga\cdot + C_2H_5\cdot$$

In comparison, tertiarybutylphosphine only has one organometallic bond, which can pyrolyze in a number of different ways[4.2]:

$$C_4H_9PH_2 \leftrightarrows PH_2\cdot + C_4H_9\cdot$$

$$C_4H_9\cdot + C_4H_9PH_2 \leftrightarrows C_4H_9PH\cdot + C_4H_{10}$$

$$C_4H_9PH\cdot \leftrightarrows PH\cdot + C_4H_9\cdot$$

The overall reaction, between triethylgallium and tertiarybutylphosphine, looks something like this[4.1]:

$$Ga(C_2H_5)_3[g] + C_4H_9PH_2[g] \rightarrow GaP[s] + 3C_2H_6[g] + C_4H_8[g]$$

TBP decomposition is enhanced on GaP surfaces, based on strong chemisorption of PH and PH_2 adatoms, to a Ga terminated surface layer. The strong attachment of the Ga–P bond weakens the P–H bonds of the phosphine surface fragments, allowing the dangling hydrogen atoms to react with TBP surface molecules. In contrast, phosphine fragments only weakly chemisorb to a SiO_2 surface, keeping a tight rein (or reign) over the hydrogen atoms, which can no longer participate in TBP catalysis. Figure 4.1 illustrates the underlying surface chemistry differences. Chemisorption of phosphine radicals on Si falls somewhere in between SiO_2 and GaP. As such, a higher supersaturation of TBP is required over Si, relative to GaP, which can lead to 3D nucleation. Because SiC and SiO_2 substrates inhibit GaP nucleation, this TPB decomposition mechanism may elucidate the selective nature of GaP deposition on foreign substrates, contaminated areas, and patterned wafers[4.1].

Although no direct studies have been carried out, there’s strong reason to believe that phosphine radicals on the surface also promote TEG decomposition, because it aids in trimethylgallium (TMG) pyrolysis. In light of TBP surface behavior, it seems inevitable that a higher supersaturation of TEG is necessary during GaP heteroepitaxy, relative to homoepitaxy. After complete surface coverage, the growth environment would seem closer to a homoepitaxial case, except for interface strain, misfit dislocations, and some interdiffusion. Clearly, TEG supersaturation is essential to achieve GaP nucleation, but how much is enough? Under low supersaturation, fewer nuclei reach critical size, which requires a longer incubation time for islands to coalesce, and more likely to yield 3D film growth. At a midrange supersaturation, a higher density of nuclei survive, leading to smoother quicker surface coverage, and a better chance for 2D layer growth. Beyond a certain supersaturation level, Ga droplets form at the expense of GaP nuclei, coarsening the surface, causing a phase separation, and potentially leading to a vapor–liquid–solid (VLS) growth mechanism, where whiskers can evolve. Once full surface coverage is obtained, the supersaturation requirements diminish, so reducing the TEG mass flux appropriately, optimizes the steady state film growth[4.4].

Varying the substrate temperature reveals three distinct GaP growth regimes, plotted in figure 4.2. At low temperatures, below 260 C, the growthrate has exponential behavior, implying kinetic limitations in the cracking efficiency of the two metalorganic precursors, TEG and TBP. At midrange temperatures, between 260 and 450 C, the growthrate still increases, but at a pace more consistent with mass flow limitations. Beyond 450 C, the growthrate declines rather sharply, suggesting another kinetic process kicks in, such as: GaP decomposition, Ga evaporation, or perhaps even Si substrate carbonization. In this last regime, the temperature boundary, where the growthrate starts to decline, differs between the two substrate orientations, Si(100) and Si(111). Inclusion of Ozasa data, who used TEG and PH_3 on Si substrates, with all other growth conditions about the same, reinforces the fundamental advantages of using TBP rather than PH_3. The weaker tertiarybutyl–PH_2 bond affords a lower growth temperature envelope than the stronger H–PH_2 bond[4.3].

Elemental analysis of GaP films grown on Si substrates in a continuous flow molecular beam reactor exhibited significant amounts of oxygen, carbon, silicon oxide, and silicon carbide at the film/ substrate interface. Figure 4.3 is a representative sample of secondary ion mass spectroscopy, for a GaP film, grown at 310 C, for 3 hours, with a TBP/TEG flux ratio of 25. In this figure, only carbon and silicon carbide are highlighted, but the oxygen/ silicon oxide counterparts possess similar behavior. Note that the phosphorous level is dramatically higher, than either carbon or silicon carbide, until its tail coincides with the carbon/ silicon carbide drop off, so even after interlayer formation, GaP still dominates the composition. As seen in figure 4.4, there appears to be an induction period of about 30 min, before carbon reaches a measurable level, then the concentration surges, and eventually tapers off to a linear dependance, with the square root of time, after about an hour into growth. Electron microscopy reveals the subcutaneous layer of silicon oxide/ silicon carbide has amorphous character. Therefore, all the data is consistent with a diffusion controlled interlayer film growth mechanism, where oxygen and carbon diffuse through the film and accumulate at the GaP/Si interface, until a high enough supersaturation is present to initiate nucleation and growth. After the excess oxygen and carbon have been consumed, the growthrate subsides to a steady state behavior[4.3].

Although the data is not conclusive, I would like to propose that TEG, rather than TBP, is the primary origin of the carbon, that leads to the subcutaneous SiC. Let me start my argument by quoting the experimental procedure Jim Kelliher explicitly points out in the literature[4.3]:

> *"After establishing ultra high vacuum conditions, heating is initiated. When the substrate reaches a temperature of 160 C, the TBP flow is switched to the growth chamber. The TEG flux is switched to the CBE chamber when the desired substrate temperature is reached to commence GaP nucleation and growth. Reversing the sequence, i.e. exposing the silicon surface first to the TEG and then adding the TBP flux, results in the formation of silicon carbide that prevents the nucleation of an epitaxial GaP film."*

The shut down procedure is very similar, in that TEG is diverted out of the growth chamber, while TBP is kept flowing through the growth chamber, until the substrate cools down below 160 C. The concept, behind flowing reactants during the heat up and cool down cycle, is to minimize decomposition/ evaporation of the volatile III–V components, on the substrate and film surface, in the presence of ultra high vacuum, which can be substantial. If you refer back to figure 4.4, the carbon concentration is below a measurable amount during the induction period. What happened to all the carbon that was supposed to be building up to supersaturation, in accordance with a diffusion controlled interlayer film growth mechanism? Part of the reason the carbon is diffusing to the interface is due to its low solubility in GaP and attractive interfacial energies for contaminants, in the same context as grain boundaries in polycrystalline materials. Perhaps the carbon doesn't get locked into the subcutaneous layer until it bonds to silicon as SiC. After the run, while the substrate is cooling down, in the absence of TEG, while only TBP is still flowing, the chemical potential for carbon shifts in the other direction, out of the film. If TBP were the primary carbon source, the carbon concentration would be preserved in the film during cool down. Besides a chemical gradient, it is conceivable that as the substrate approaches room temperature, elastic stresses and strains at the interface become relieved as the lattice mismatch diminishes, until interfacial energies become less attractive to contaminants. We already know TEG produces SiC directly on the silicon substrate if used during the heat up cycle. In addition, a comparison of GaP and GaAs films grown with trimethylgallium versus triethylgallium revealed less carbon incorporation in films originating from TEG[4.1]. From a chemical bonding viewpoint, a trend appears to be taking shape; the more stable the carbon radical created after metalorganic decomposition, the less carbon is incorporated in the film. Let's look at the carbon radical stability in relation to the number of nearest carbon neighbors:

metalorganic	*TMG*	*TEG*	*TBP*
radical stability	$CH_3\cdot <$	$CH_3CH_2\cdot <$	$(CH_3)_3C\cdot$
reactivity	$CH_3\cdot >$	$CH_3CH_2\cdot >$	$(CH_3)_3C\cdot$
radical type	0°	1°	3°

The less stable a particular species is, the more reactive it will be, so there appears to be a direct correlation between carbon incorporation and radical reactivity. Beware, carbon chain length has less bearing on reactivity than the number of carbons surrounding the activated carbon, so a 2° carbon radical, such as isopropyl, $(CH_3)_2CH\cdot$, would fall sequentially in between 1° and 3°, in terms of stability. On the basis of this analysis, triisobutylgallium (TIBG) , another commonly available Ga source, would be better than TEG, with respect to carbon incorporation. Although I have not seen any commercially available product, clearly something along the lines of tertiarybutylgallium (TBG), would be the ultimate Ga source, with only one highly stable carbon radical created. Any discussion concerning the origin of the oxygen might be even more speculative than carbon, suffice it to say that water frequently contaminates metalorganics.

Before we move on, I wanted to make a few more points regarding metalorganics and the data presented in Jim Kelliher's literature. To prevent Ga droplet formation on GaP films, a TBP/TEG mass flux ratio of 25 is required for Si(100), in comparison to a mass flux ratio of 10 for Si(111), so substrate orientation appears to influence film growth direction and associated surface kinetics, such as: nucleation, Ga evaporation, Ga diffusion, organometallic decomposition, etc. In fact, x–ray diffraction results confirm that GaP films grow with the same surface orientation as the underlying substrate, which would imply coherence. For stoichiometric GaP films, a TBP/TEG mass flux ratio of 25 serves as a critical boundary, in a continuous flow molecular beam environment, for two reasons. First of all, the cracking temperature of TEG is lower than TBP. Secondly, TEG has a sticking coefficient near unity, in comparison to most phosphorous precursors, which have sticking coefficients < 1. Under those circumstances, equal amounts of TEG and TBP decompose, although TEG would release three times as many carbon radicals as TBP. Before the substrate temperature reaches 160 C, TBP flow must be initiated in the CBE chamber; otherwise, no growth occurs. Apparently, TBP passivates the Si(100) 1x1 hydrogen terminated surface, through hydrogen and phosphine fragments, as the substrate approaches growth temperature. One strategy for reducing carbon incorporation in GaP films is to grow at higher temperatures; however, this would somewhat defeat the purpose of using metalorganic precursors in the first place[4.1].

Needless to say, carbon and oxygen are undesirable components in a GaP film, so our lab engaged in a major paradigm shift concerning reactant flows. Rather than increase the substrate temperature, as eluded to by others in the last paragraph, why not have a continuous flow of hydrogen gas during growth? We already saw the virtues of how dangling hydrogen atoms, from phosphine surface radicals, catalytically enhance TBP decomposition, perhaps additional hydrogen will: replenish those dangling hydrogen atoms consumed, scavenge carbon/ oxygen adatoms on the surface, and promote TEG decomposition, since three successive ethyl groups need removal. In addition, a GaP film is composed of alternating layers of gallium and phosphorous atoms, so why not pulse the metalorganic precursors, at separate times, with a delay in between pulses to: allow each reactant to decompose more effectively, reduce unintentional burying of contaminants, increase hydrogen exposure, and give surface adatoms time to migrate around on the surface, improving crystal integrity. Figure 4.5 depicts a typical reactant pulsing scheme, and the associated GaP film reflectivity fluctuations, which will be covered in more detail later in this chapter. Although atomic layer epitaxy (ALE) is feasible for certain GaP systems[4.3], the growth chemistry in our CBE chamber does not exhibit self termination behavior, beyond each monolayer. However, we could arbitrarily impose ALE, based on an average growth cycle, by modulating our pulses appropriately. At this stage, it’s not clear if “pseudo–ALE” conditions would provide any tangible benefit. For the pulse sequence shown in figure 4.5, roughly 2 monolayers deposit, per source vapor cycle, on average.

During GaP growth, in the process window: $260 \leqslant T \leqslant 450$ C, a surface reaction layer, containing intermediate species between reactants and products, was discovered through reflectance measurements. In parallel to that, pulsing investigations were carried out, where only the delay time between reactant pulses is varied, with the pulses themselves kept constant. When the delay time after a TBP pulse is extended, the growthrate per source cycle does not change; whereas, lengthening the delay time after a TEG pulse increases the growthrate per source cycle, meaning a residual of active species is still present, never quite reaching fruition. Despite a near unity sticking coefficient, and a lower cracking temperature, TEG appears to kinetically limit the growth process, with the remaining ethyl groups invoking the barrier. Thus, in addition to TBP fragments, the surface reaction layer probably contains monoethylgallium and gallium adatoms, at the upper end of growth temperature window, and a full spectrum of adatoms, including TEG, diethylgallium, monoethylgallium, and gallium, at the lower end of the growth temperature window. With a peak thickness on the order of a few monolayers during the TEG pulse, the surface reaction layer perpetually changes in thickness and composition throughout the source cycle. Ideally, you would like to see the surface reaction layer approach extinction before the next TBP pulse; however, under excess reactant flow, it's conceivable that some species carry over from one pulse cycle to the next[4.2].

4.3 Reflectometry

Crystal growers have long sought a noninvasive, nondestructive way to monitor film quality and thickness, as the process evolves. The most common technique involves reflectometry, where a light beam is projected into the growth chamber, striking the substrate at a near perpendicular incidence angle, and measuring the outgoing reflectance intensity. Generally, a wavelength is chosen below the bandgap of the deposit layers, so the incident beam does not get absorbed, as the film continues to grow. As figure 4.6 illustrates for a multilayer film, the incoming beam reflects off every interface where the index of refraction changes, including: the growth surface, intermediate layers, and the substrate. Each reflected beam traverses a different length, based on the given film layer thickness, which results in constructive or destructive interference, when the beams coalesce at the surface. Although each interface has the potential to change the phase of the incident and reflected beams, postgrowth thickness calibrations help to compensate for phase shifts. Therefore, the spacing between interference fringes serves as a guide to deposit thickness, while the change in fringe amplitudes gives an indication of film quality, since the reflectivity of a smoother film decays more slowly, over time, than a rougher deposit.

A more sophisticated approach to reflectometry would use plane polarized light impinging on a substrate at the Brewster angle. Plane polarized light has the property that its polarity is aligned with the plane containing the incoming and outgoing light beams. The Brewster angle uniquely defines the angle where an insulator material allows virtually 100 % transmission of plane polarized light through its lattice. In semiconductor materials where some adsorption takes place, the name pseudo–Brewster angle applies, and it signifies the angle where maximum transmission occurs for plane polarized light. Figure 4.7 compares the plane polarized light behavior for gallium and sodium from a light source at 589.3 nm. The TM mode is equivalent to plane polarized light, and the TE mode is exactly perpendicular to plane polarization. At this wavelength, sodium behaves like a metal and reflects most of the light away; whereas, gallium exhibits semicondutor character, expressing its pseudo–Brewster angle at 82 degrees, which represents the minimum reflectance/ maximum transmission value.

So, plane polarized light, at the Brewster angle, permits the maximum transmission level, which ultimately leads to the most sensitive interference signal. Let’s look at a plane–polarized reflectance spectroscopy (PRS) arrangement, shown in figure 4.8. Since coherence is not a constraint, the light beam can be a laser, a light emitting diode, or a focused lamp. In the case of a lamp, a band pass filter would need to be chosen to limit the light source to a single wavelength. To adjust the polarizer, you simply rotate it, until you obtain a minimum signal on the photodiode detector, which signifies plane polarization. For a wavelength at 632.8 nm, the Si substrate has a Brewster angle of 75 degrees. With heteroepitaxy, there's always a trade off between selecting the Brewster angle of the substrate versus the film, but in this case, GaP has a Brewster angle of 72 degrees for the same wavelength as Si. As we saw in figure 4.7, the Brewster angle is generally not an abrupt feature, so anywhere close is acceptable. Because nucleation is the most critical stage of film growth in the suppression of 3D growth modes, our lab favors the Brewster angle of the substrate. The windows represent two chamber ports that are transparent for the light spectrum dictated by experiments. Included in the setup is a photomultiplier tube, at an arbitrary angle, to give an indication of film roughness through a scattered signal.

As figure 4.9 depicts, the GaP heteroepitaxy optical mediums consist of: the ambient, a transient surface reaction layer (SRL), the GaP film, and the Si substrate. Three critical interfaces contribute to the interference signal: 1) the film/ substrate interface provides long range interference fringes characteristic of the film thickness, 2) the SRL/ film interface superimposes itself as fine structure on the interference fringes, fluctuating in synchronization with the source cycle, and 3) the ambient/ SRL interface serves as a reference beam. Figure 4.10 presents the overall features of PRS, with inserts magnifying the fine structure, and the bottom curve showing the scattered light signal. For both the PRS and the scattered light signal, the sharp response in the first two minutes of growth represents the nucleation phase, where islands temporarily add texture to the film surface. For GaP on Si, the periodicity of interference fringes occurs every 1050 Å, according to Fresnel equation calculations. Figure 4.5 demonstrates how the fine structure oscillates at the same frequency as the pulse cycle, which has a period of 4 s. At this point, I would like to defer the conscientious reader to two comprehensive reviews on PRS, the fine structure, and the application of Fresnel equations, in references [4.5] and [4.6], since no further knowledge, than covered here, will be required in the interpretation of my experimental data.

4.4 Conclusion

Basically, we have seen that GaP deposition on Si is not only possible by chemical beam epitaxy, but it’s lattice grows in the same orientation as the underlying substrate, perhaps due in part to similar unit cells and lattice constants. Tertiarybutylphosphine gives rise to phosphine radicals on the growth surface that help passivate the Si substrate prior to GaP deposition, and catalytically enhance both TBP and TMG decomposition, with the likelihood towards TEG as well. There appears to be a provocative correlation between the reactivity of carbon radicals, originating from metalorganic precursors, and carbon incorporation in the film. No specific mechanism has been proposed for carbon incorporation, but it seems likely that the more reactive carbon radicals are more capable of bonding to the surface or displacing less hearty species. In tandem with carbon, oxygen has been observed to incorporate in the lattice, and diffuse toward the GaP/Si interface during film growth. The driving force behind this migration is low solubility in the GaP film, reduced interfacial energy, and under supersaturated conditions, formation of silicon carbide, silicon oxide. Although raising the growth temperature might reduce contaminants, a constant flow of hydrogen scavenges undesirable surface species, and alternating pulsed reactant beams separate the decomposition reactions. On the growth front, a transient surface reaction layer, whose species are dominated by TEG intermediates, may hold the key to controlling the GaP lattice structure. Through the use of the plane–polarized light at the Brewster angle, reflectometry becomes an ultrasensitive real time tool in evaluating surface and film layers simultaneously.

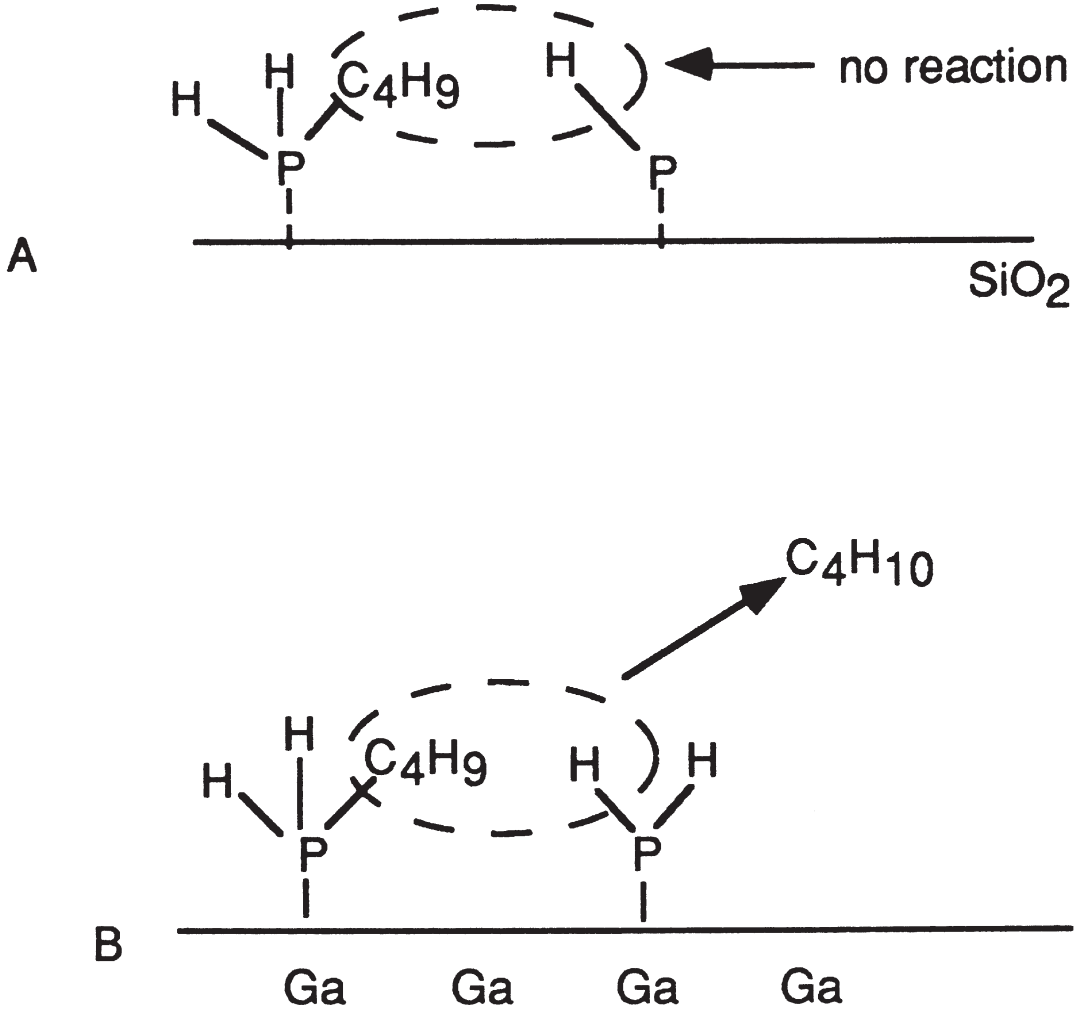

Figure 4.1: Substrate influences on TBP decomposition: (a) silicon oxide, (b) GaP.

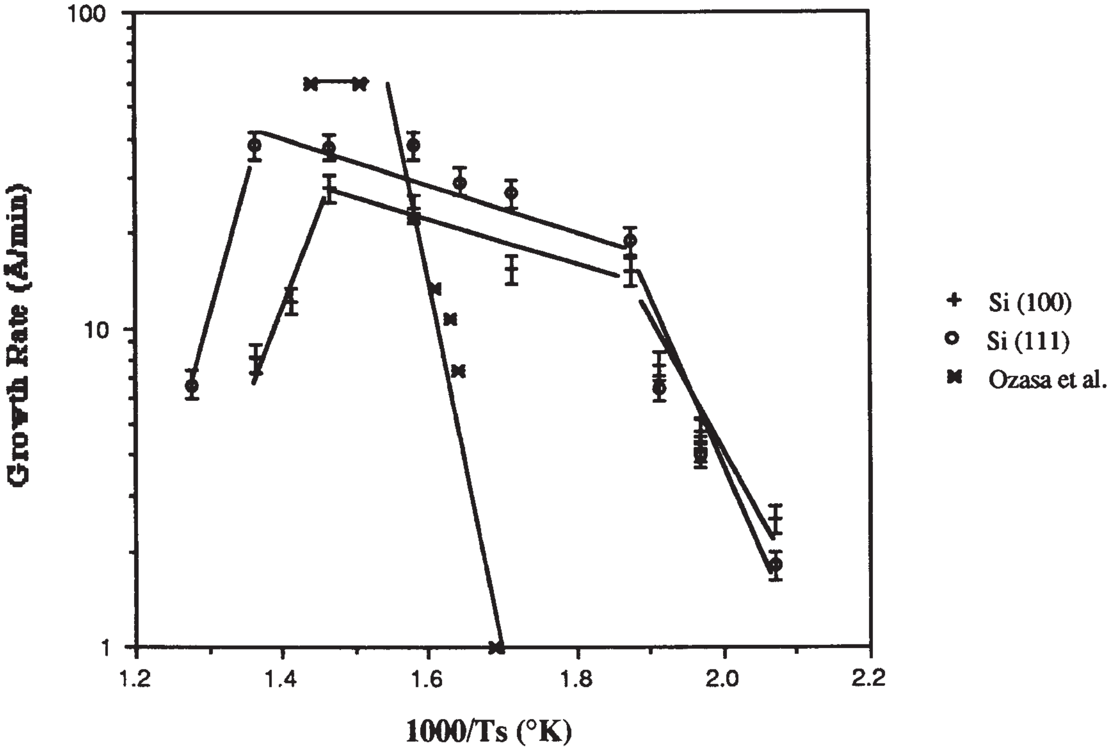

Figure 4.2: Temperature dependence of GaP growthrate utilizing TEG and TBP vapor sources on Si(100), Si(111) substrates, in contrast to literature data where TEG and phosphine sources were used instead.

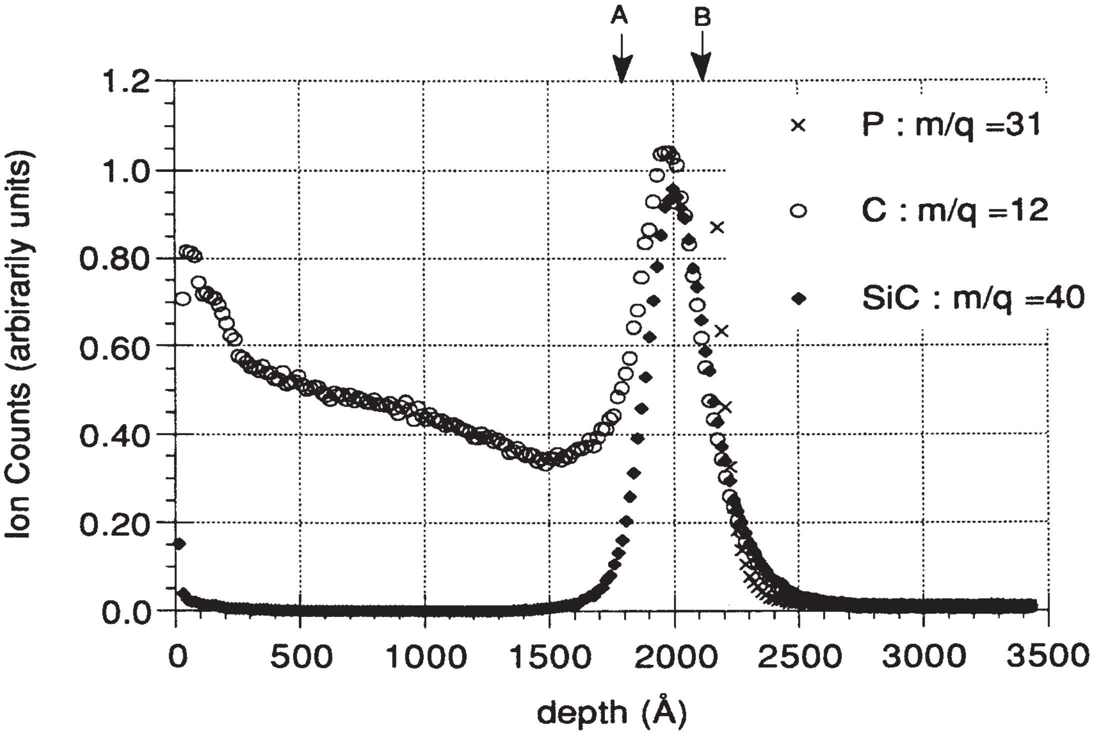

Figure 4.3: “Elemental” depth profile of phosphorous, carbon, and silicon carbide for a typical GaP film grown on Si.

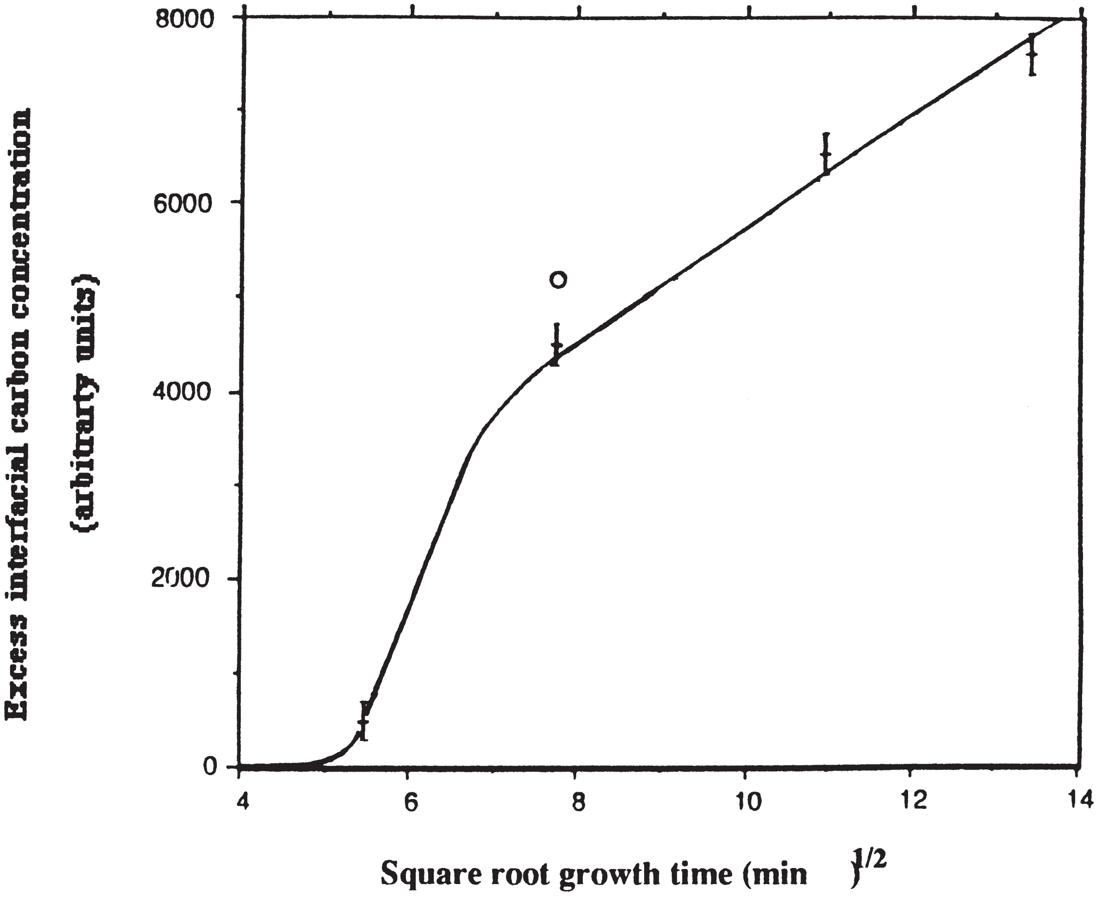

Figure 4.4: Interfacial carbon concentration as a function of the square root of growth time.

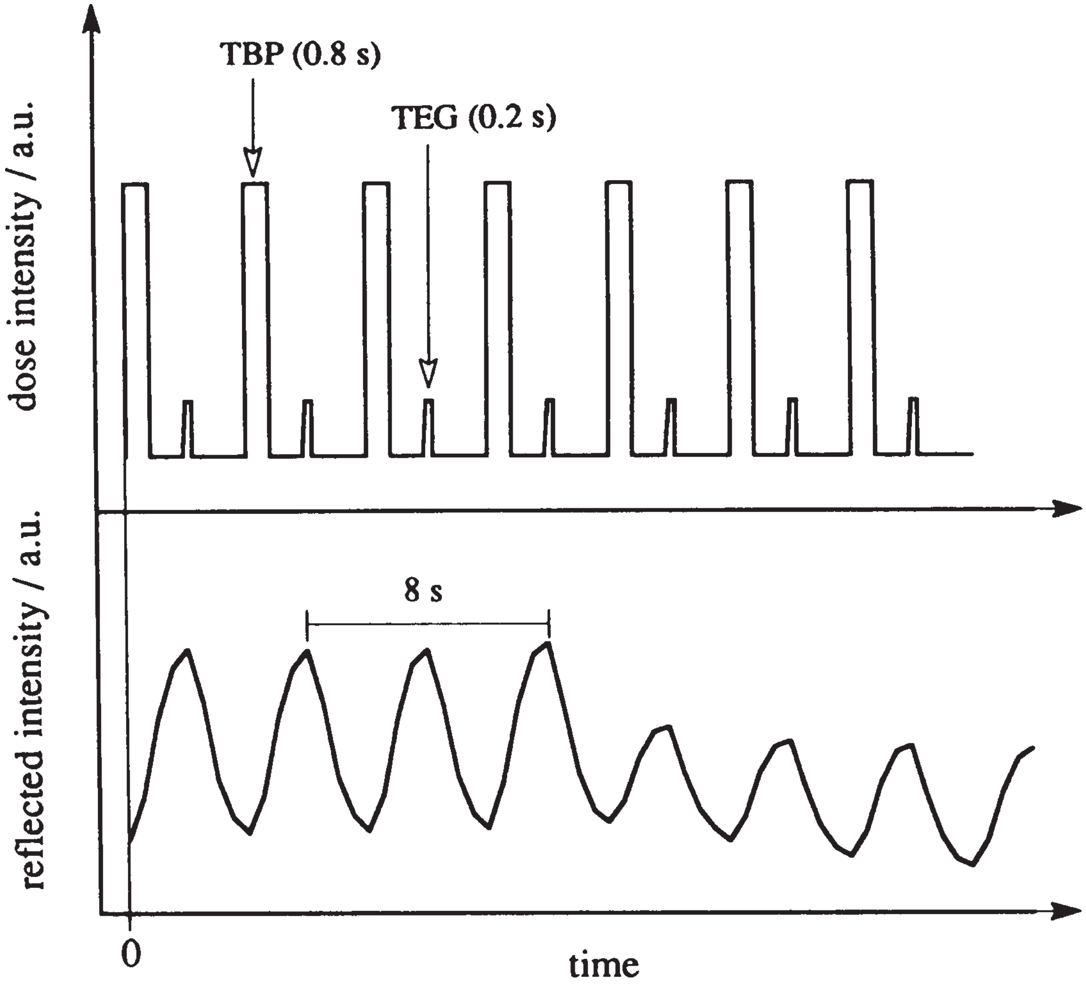

Figure 4.5: Vapor source pulse sequence, with a 4 s overall pulse cycle, and corresponding GaP surface reflectance signal.

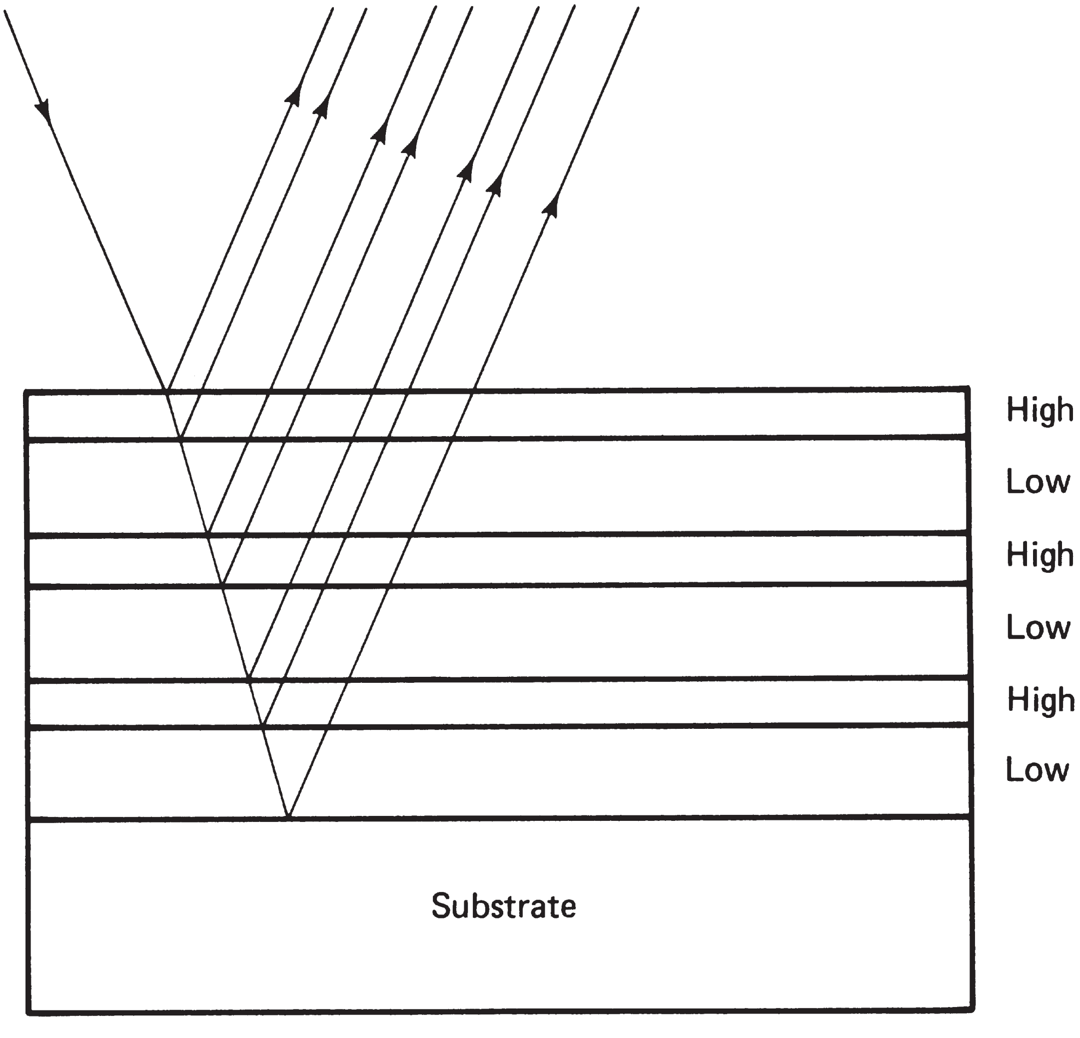

Figure 4.6: Origin of interference fringes in a multilayer dielectric film having alternating indexes of refraction.

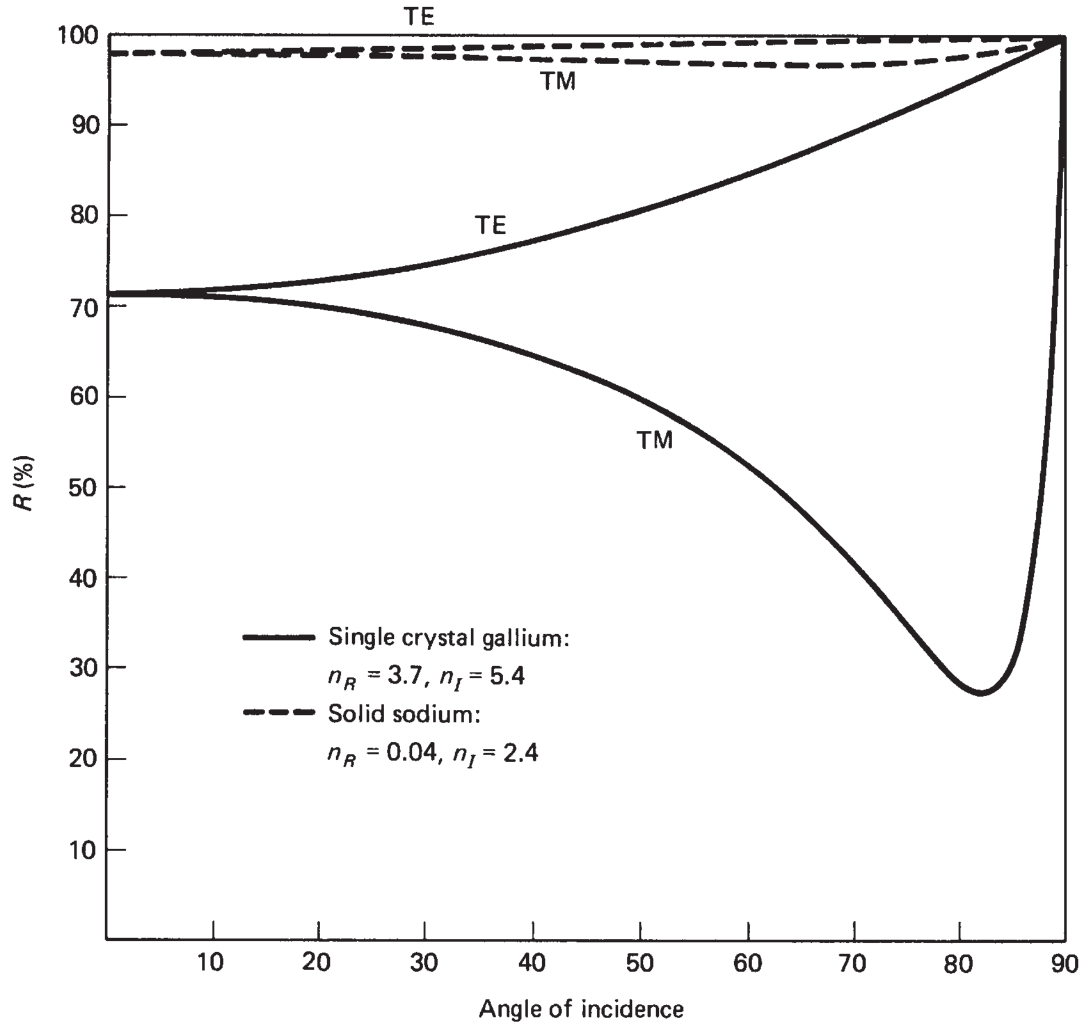

Figure 4.7: Reflectance intensity of Ga and Na over a range of incident angles from a light source at 589.3 nm.

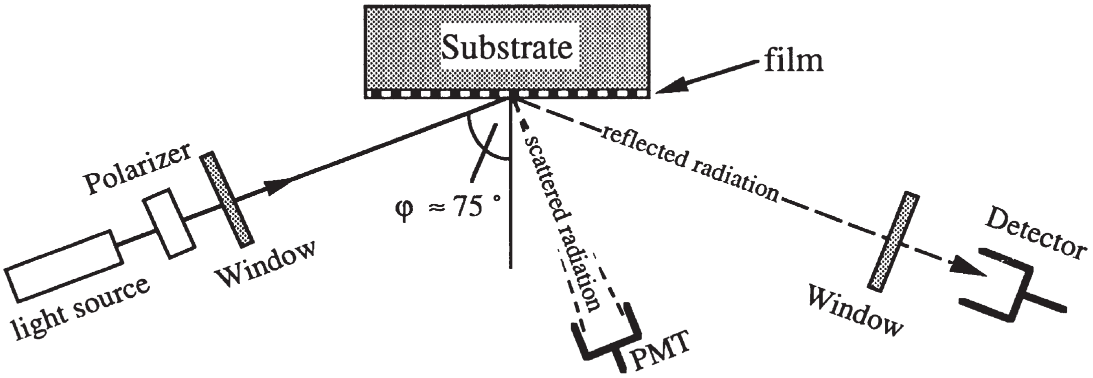

Figure 4.8: Plane–polarized reflectance spectroscopy experimental set up.

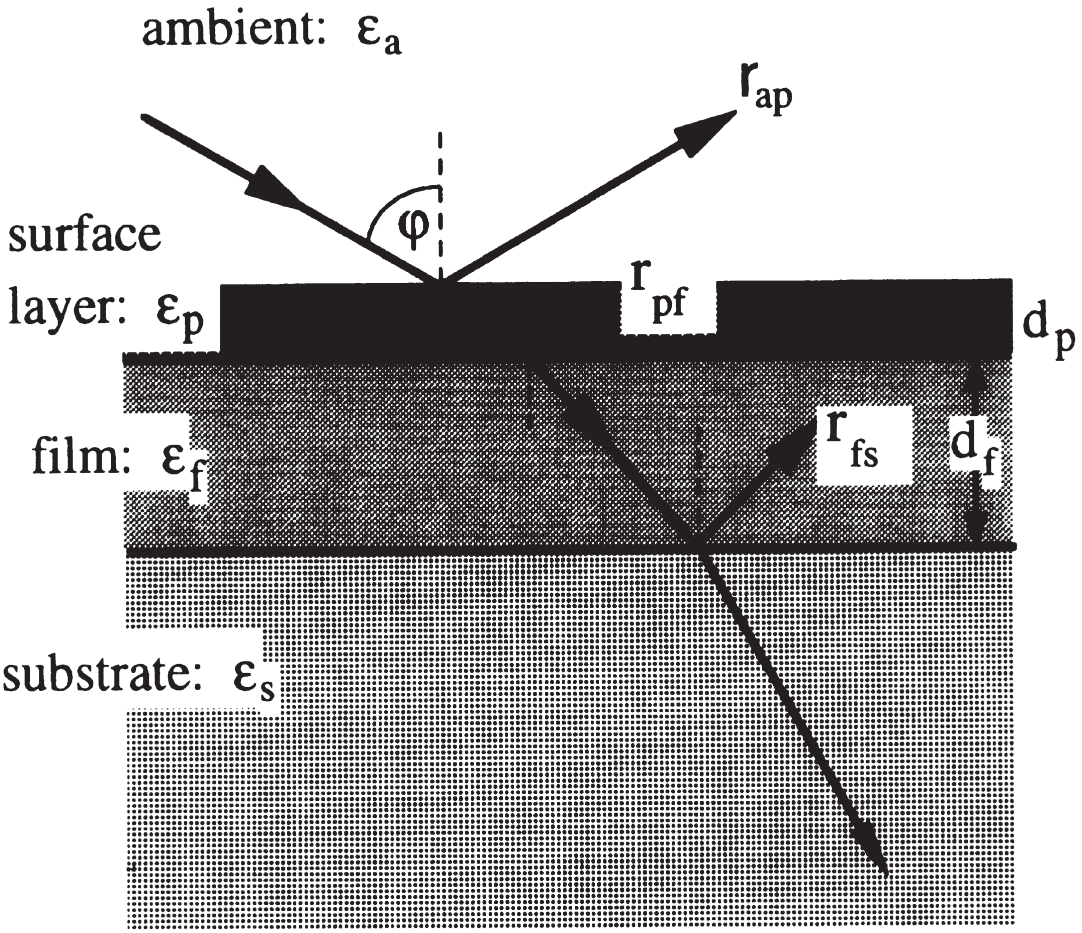

Figure 4.9: The optical mediums and associated interfaces encountered during chemical beam epitaxy of GaP on Si.

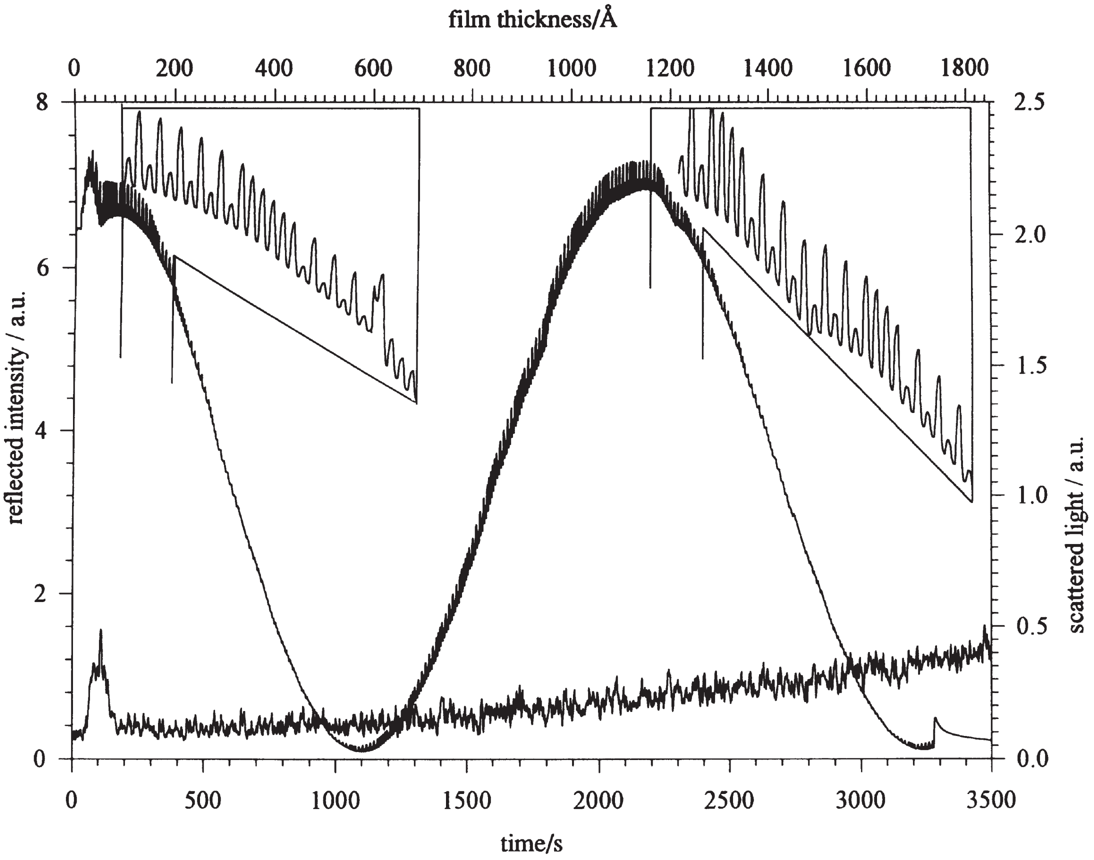

Figure 4.10: Plane–polarized reflectance spectroscopy signal, upper curve, and accompanying scattered light intensity, lower curve, for heteroepitaxial growth of GaP on Si.

References

[4.1] J. T. Kelliher, *PhD Thesis*, North Carolina State University: Raleigh, NC (1994).

[4.2] K. J. Bachmann, et al., *Journal of Crystal Growth*, **183**, 323 (1998).

[4.3] J. T. Kelliher, et al., *Materials Science and Engineering*, **B22**, 97 (1993).

[4.4] K. J. Bachmann, et al., *Journal of Vacuum Science and Technology*, **B14**, 3019 (1996).

[4.5] N. Dietz and K. J. Bachmann, *MRS Bulletin*, **5**, 49 (1995).

[4.6] N. Dietz and K. J. Bachmann, *Vacuum*, **47**, 133 (1996).

[4.7] F. L. Pedrotti and L. S. Pedrotti, *Introduction to Optics*, Prentice–Hall: Englewood Cliffs, NJ (1987).

5

GaN Literature Review

5.1 Introduction

AlN, GaN, and InN have shown promise in optoelectronic, elevated temperature, and high power device applications. These materials and their alloys cover the energy gap range of 1.9 to 6.2 eV, with wavelengths ranging from 650 to 200 nm, spanning the light spectrum from red to ultraviolet (uv). On the device front, they have suitable properties for: negative electron affinity cold cathodes, electronic devices, surface acoustic wave devices, uv detectors, Bragg reflectors/ waveguides, uv/ visible light emitting diodes (LED), and laser diodes for digital data read/ write applications. Figure 5.1 summarizes the overall performance parameters associated with the III–V nitride materials[5.1].

With all that potential, growth of GaN thin films was originally attempted by hydride vapor phase epitaxy (HVPE) [5.2]. Subsequently, metal organic chemical vapor deposition (MOCVD) [5.3] and molecular beam epitaxy (MBE) [5.4] came along with each technique having its advantages and disadvantages. For instance, HVPE is probably the fastest technique for growing films, the MOCVD method historically produces the best quality films, while the MBE approach boasts the lowest temperature growth and most control. Since my research involved molecular beam techniques, the focus of this chapter will be on theoretical and experimental literature addressing molecular beam issues. Although the order of presentation may seem unusual, I narrowed down the field of papers to the most significant achievements, then put them in a chronological sequence, to emphasize how each landmark sets the stage for new development.

5.2 Growth Model

In a molecular beam growth environment, GaN achieves optimum growthrate in the temperature range of 750 to 800 C. Below 750 C, it is believed to be kinetically limited by reduced nitrogen incorporation. Above 800 C, GaN decomposition and/or Ga desorption are thought to come into play[5.5].

When Ga hits the growth surface in a GaN molecular beam system, Ga adsorbs on the surface in two possible energy states. The first layer of Ga sticks to the surface in a strongly bound state; whereas, subsequent layers are more loosely bound and desorb significantly easier than the primary layer. The primary layer differs from secondary layers because only the first layer can chemisorb, in comparison to the other layers, which physisorb. In fact, Ga in excess of monolayer coverage will hinder growth by blocking out prospective nitrogen species from reacting into a thermodynamically preferred surface state[5.5].

One way to differentiate between the two Ga surface states is to look at hydrogen evolution from the surface with a mass spectrometer. If Ga and ammonia are III–V source beams, respectively, then they lead to the forward reaction on the surface:

$$2Ga + 2NH_3 \rightarrow 2GaN + 3H_2$$

Researchers at the University of Minnesota demonstrated experimentally, using desorption mass spectroscopy, that only the first layer of Ga on a GaN surface resulted in elevated hydrogen evolution. Beyond monolayer coverage, Ga accumulation on the surface didn’t generate any additional hydrogen above the background level, confirming that ammonia reacts only to first layer Ga sites[5.5].

However, a competing reaction, contributing to hydrogen generation, can result from ammonia decomposition, even in the absence of Ga:

$$2NH_3 \rightarrow N_2 + 3H_2$$

If the substrate temperature is held constant, along with a steady state flow of ammonia, then there is no reason to believe that this aspect of hydrogen evolution would change significantly over time, interfering with the background hydrogen level[5.5].

Based on these arguments, the scientists used a simple mass balance equation around a fixed surface area, to relate hydrogen evolution change, μH_2, to GaN growthrate:

$$\frac{1}{A}\frac{dN_{Ga}}{dt} = F_{Ga} - F_N(1 - {}_{Ga}) - {}_{Ga}F_0(T)$$

where: A = *substrate surface area*
N_{Ga} = *number of Ga sites*
t = *time*
F_{Ga} = *Ga flux*
F_N = *N flux provided by* NH_3
${}_{Ga}$ = *Ga surface coverage*
$F_0(T)$ = *Ga desorption flux*
or evaporation rate
at substrate temperature

Separating the terms, the equation reads, the change in Ga sites over time for the substrate surface equals the incoming Ga flux minus the film growthrate minus the overall Ga desorption rate. The film growthrate, the middle term to the right of the equal sign, requires the most clarification. It assumes that the Ga flux is greater than the N flux, so that all nitrogen reacts on surface contact to strongly bound Ga sites, $(1 - {}_{Ga})$. In contrast, the overall desorption, the last term on the right, can only take place from weakly bound Ga sites, whose surface coverage is ${}_{Ga}$. Despite the model's simplicity, figure 5.2 demonstrates the results between experimental and theoretical values. The peak near the center of the curve is where the Ga flux presumably equals the N flux. Therefore, excess Ga does indeed reduce GaN film growth, theoretically and experimentally. Within the temperature range of 700 to 800 C, higher temperatures suppress the decline better than lower temperatures. Perhaps the larger discrepancies between experimental and theoretical values at lower temperatures hinge on the nitrogen incorporation efficiency[5.5].

5.3 Physisorption Precursor

Russian scientists believe that group III nitrides differ significantly from other III–V compounds in accord with a nitrogen physisorption precursor, illustrated in figure 5.3. The boundaries of the curve, E^{v}_{Ga} and $E^{v}_{N_2}$, represent the free atom or vacuum energy levels of gallium and nitrogen in the gas phase, respectively. Although most atoms and molecules have the potential to physisorb prior to chemisorption, some have an activation energy, between the two adsorption states, that stays below the free atom level, permitting spontaneous chemisorption. In the case of GaN, nitrogen has a substantial barrier, between the two adsorption states, which gives it relative stability after chemisorption, but reluctance to react prior to chemisorption. This explains why activation of pure nitrogen by plasma or ionization is necessary for nitride growth. Additionally, GaN exhibits higher thermal stability, relative to GaP or GaAs, at elevated temperatures, despite the higher volatility of nitrogen over the other group V elements[5.6].

To prove their point, the researchers developed a phase type diagram, showing the boundary between liquid and solid GaN, with and without the physisorption barrier, for a wide range of nitrogen fluxes and temperatures, keeping the Ga flux fixed. As figure 5.4 shows, most people deposit GaN films, in a plasma enhanced molecular beam system, near the border between liquid and solid phase. Without the physisorption barrier, the thermodynamic model would predict only liquid over the vast range of experimental growth conditions[5.6].

5.4 Ammonia Catalysis

An On–Surface Cracking (OSC) approach has emerged for molecular beam growth of GaN. The new group V injector takes advantage of ammonia catalysis experience on metal surfaces and is somewhat of a hybrid between a nitrogen plasma beam and a conventional ammonia leak valve. Ammonia passes through a small pretreatment chamber with molybdenum disc flow baffles, which catalytically precrack the ammonia into a mixture of ammonia, nitrogen, and hydrogen, depending on flowrate, temperature, and pressure settings within the injector[5.7].

5.5 Polarity

GaN grows most commonly in a hexagonal wurtzite structure, along with the other nitrides, AlN and InN. In contrast, BN, as well as many other III–V compounds; GaP, GaAs, AlP, and InP, favor a cubic growth habit. However, the cubic zinc blende structure for GaN is also encountered in heteroepitaxy. Some would even argue that cubic and hexagonal forms are inseparable, although one structure generally dominates for a given growth environment and substrate.

Let’s look at a GaN wurtzite lattice, represented in figure 5.5. The gallium face occurs in the <0001> direction, while the nitrogen face is oriented in the $<000\bar{1}>$ direction. One has to be careful in differentiating the two faces, because polarity is a bulk characteristic of the crystal, rather than a surface phenomenon, so it’s quite possible to have a Ga terminated surface on a nitrogen face and vice versa. As such, “capping,” “polarity,” and “face” are preferable terms to “termination” in reference to polarity[5.8].

One factor that distinguishes wurtzite nitride deposition from the other III–V compounds is growth along the polar axis, either the <0001> or $<000\bar{1}>$ direction. In comparison, all the zinc blende III–V materials, such as GaAs, grow along a non–polar axis, including cubic GaN[5.8].

Polarity arises in compounds due to electronegativity differences between the elements in combination with orientation. For instance, carbon dioxide is a linear structure, which balances out the charges between the two C–O bonds, so turns out nonpolar; whereas, water is a bent structure, which still carries a net dipole, when charges between the two O–H bonds are summed up, spatially. In a binary element system, with a single coordination arrangement between atoms, such as the III–V or II–VI compounds, polarity is inevitable, unless the electronegativities have equal magnitude.

Hellman[5.8], at Bell Labs, did an exhaustive literature review of GaN polarity, and learned that Ga, N surface faces have completely different chemical behavior; the Ga face having better stability. Under molecular beam growth environments, the N face polarity grows 10 to 20 times slower than Ga face polarity. This might be attributed to two decomposition reactions which occur more favorably in N face direction:

$$2GaN \rightarrow N_2 + 2Ga$$

$$GaN + N \rightarrow N_2 + Ga$$

In addition, the N face will etch on the order of 10 times faster than a comparable Ga face in KOH or NaOH aqueous solutions. 3x surface reconstructions are frequently observed for N face surfaces in the 100 to 300 C temperature range; whereas, 2x reconstructions are more characteristic of Ga face surfaces[5.8].

Polarity plays an important role during GaN nucleation, on like or foreign substrates. Take for example, sapphire (aluminum oxide), which has received quite a bit of attention among experimentalists. Sapphire starts out nonpolar, but researchers have learned that nitriding the surface improves GaN nucleation. If you compare the surface energies for the two possible polarities of AlN, established during nitridation, only the Al face structure is stable under typical growth conditions. Some authors feel that the nitridation step may create the necessary polarity for GaN growth[5.8].

Another coveted step by experimentalists is a low temperature GaN buffer layer followed by a high temperature anneal on sapphire. Considering the disparity in decomposition rates between the Ga and N faces, perhaps the N face nuclei are eliminated in this procedure. Generally speaking, Ga face polarity films have smoother more desirable morphology than N face counterparts[5.8].

5.6 MBE Sources

There’s a number of different ways to operate a molecular beam epitaxy, MBE, system and its name depends on the source types. To use GaN as an example:

Name	Abbreviation	III source	V source
microwave plasma electron cyclotron resonance MBE	ECR–MBE	Ga	ECR–N_2
gas source MBE	GSMBE	Ga	NH_3
metal organic MBE	MOMBE	TEG	plasma N_2
chemical beam epitaxy	CBE	TEG	NH_3

On the III side, Ga metal effusion cells or an organometallic precursor, triethylgallium, TEG, supplies the necessary material; whereas, the V side contains either a nitrogen plasma or ammonia beam.

A research group from the University of Houston explored MBE growth of GaN using all the combinations listed in the III–V source table. They studied in situ reflection high energy electron diffraction, RHEED, and a fairly new surface probe called time of flight mass spectroscopy of recoiled ions, TOF–MSRI, derived from ion scattering spectroscopy. The TOF–MSRI technique involves a low energy ion beam hitting the growth surface at a shallow angle of incidence and evaluating the species which etch off the surface in a mass spectrometer. Although it sounds similar in nature to secondary ion mass spectroscopy, SIMS, the new scattering method: 1) has such a low energy ion beam, that is virtually nondestructive to the target surface, 2) is nearly independent of chemical environment, so matrix effects are minimized, and 3) has substantially better sensitivity, particularly in the lighter elements, compared to SIMS. So, the scientists were able to track surface crystallinity with RHEED and elemental surface fluctuations with TOF–MSRI [5.9].

The overwhelming wisdom among GaN crystal growers is to: 1) nitride the sapphire surface, 2) deposit a low temperature GaN buffer layer, 3) anneal buffer layer at high temperature, then 4) proceed with continuous GaN film growth at a relatively high temperature. The researchers at University of Houston evaluated each of these steps with various source combinations under in situ surface analysis[5.9].

First they looked at optimizing the sapphire nitradation temperature, so a 3 sccm stream of microwave ECR nitrogen plasma was aimed at the aluminum oxide substrate at a constant microwave power, and only the substrate temperature was varied. TOF–MSRI showed an onset of nitridation occurring above 650 C, as a nitrogen peak emerged. In contrast, RHEED didn’t indicate any change in crystallinity until 700 C, which illustrates the superior performance of the new ion scattering technique[5.9].

The next endeavor was to determine the minimum nitrogen exposure time for complete nitridation. This was accomplished by keeping the substrate temperature, nitrogen flow, and microwave power constant, while taking TOF–MSRI and RHEED samples at 10 minute intervals. After 20 min, the nitrogen peak of the mass spectrum had already saturated out, but the carbon peak was still declining, which demonstrated the cleaning aspects of the ECR nitrogen plasma in addition to nitridation. Beyond 30 min, no significant change in measurements were observed for TOF–MSRI, but RHEED indicated crystal degradation. The RHEED pattern showed overlapping aluminum nitride and aluminum oxide crystalline behavior until the 30 min mark[5.9].

For GaN buffer layer growth, experiments similar to the nitridation series were repeated with a Ga beam, representing ECR–MBE conditions. The minimum temperature for crystalline GaN buffer layer growth turned out to be 500 C as determined by RHEED. Subsequent anneal at 750 C showed no change in RHEED pattern, confirming crystallinity. In the exposure time experiments, elemental analysis revealed only N, O, Al, and Ga peaks, no contaminants throughout the procedure. Within 5 min, the Al and O peaks disappear, indicating the buffer layer had already exceeded the ion probe depth of a few monolayers. RHEED patterns suggested two dimensional crystal film growth. Again, beyond 30 min, TOF–MSRI spectrums don't change. Annealing at 750 C didn't influence either surface probe; therefore, the buffer layer maintains crystallinity throughout the entire experiment[5.9].

To compare the work with plasma, the Houston scientists ventured into gas source MBE, which uses gallium and ammonia sources. Without plasma activation, the substrate temperature must be elevated to 780 C to achieve sapphire nitridation. Such a high cracking temperature for ammonia reduces the residence time of the reactants on the surface, which could lead to desorption before the nitridation can take place. Aluminum oxide nitridation requires an exchange reaction between the O and the N atoms which slows down the process even further relative to steady state GaN growth. Ion scattering measurements reveal a weaker N peak than normally seen with ECR nitrogen plasma, plus an almost constant O peak intensity throughout the nitridation, demonstrating a less robust nitridation and very little O/N exchange. RHEED images change from a crystalline aluminum oxide pattern to a diffuse amorphous behavior. Therefore, the evidence suggests that an amorphous aluminum oxy–nitride, AlON, was formed[5.9].

In contrast to sapphire nitridation, GaN buffer layers form at a substrate temperature of 550 C in a gas source MBE environment, which illustrates how Ga on the surface may catalytically benefit ammonia cracking. Elemental surface analysis shows Al and O peaks still present, meaning the GaN doesn't completely cover the surface, at least down to the resolution of a few monolayers. RHEED patterns give diffuse images characteristic of amorphous or rough surfaces. Annealing leads to crystallization and a reduction in the Ga/N ratio from 5.4/1 down to 2.5/1, due exclusively to diminishing Ga peak intensity. This implies that the excess Ga, which may have formed droplets on the surface, evaporate away during the annealing process[5.9].

Under gas source MBE conditions, GaN growth is finally attempted, starting with flux experiments, to determine which flow conditions result in stoichiometric surface composition. Figure 5.6 shows the Ga to N peak intensities for two distinct Ga effusion cell temperatures, as the ammonia flux is allowed to vary. The dotted curve represents a Ga cell temperature of 950 C, characteristic of 2.8 x 10^{-6} Torr beam pressure; while the solid curve is a threefold increase in flux, at a Ga cell temperature of 1000 C and an equivalent beam pressure of 8.5 x 10^{-6} Torr. In the lower Ga flux case, there's a wide window of 1:1 Ga/N stoichiometry and the curve is rather smooth; whereas, the solid curve seems rather abrupt and never achieves stoichiometry. Clearly, a deficient ammonia flux results in a Ga rich surface, but what circumstances might lead to a Ga rich surface at higher ammonia bombardment? Taking into account the chemistry, recall that GaN formation generates hydrogen. If that hydrogen is swamped by incoming ammonia molecules, it will have to fight harder to diffuse up to the surface and desorb. Perhaps stoichiometry is never achieved in the higher Ga flux case, because the GaN surface is already saturated with Ga, so any additional Ga buries the reactive sites at the GaN interface, imposing a diffusion barrier for incoming ammonia and impeding hydrogen liberation[5.9].

Shifting their attention to chemical beam epitaxy, CBE, the Houston researchers took advantage of their previous knowledge, and settled for an ECR nitrogen plasma to nitride the sapphire substrate. For the buffer layer, they attempted chemical beam epitaxy, with TEG and ammonia; however, no GaN nucleated on the surface, for a wide range of substrate temperatures. To explain the failure, the authors provide some possible scenarios: 1) TEG and other ethyl–gallium surface intermediates may not have as favorable bonding configuration as gallium to catalyze ammonia cracking, 2) presence of the ethyl bonds to gallium reduces the binding energy to the surface and the overall residence time of any gallium–ethyl–ammonia complex relative to gallium alone, 3) oxygen contamination, attributed to metalorganics, can produce volatile gallium surface complexes which desorb fairly readily, or enhance the reaction barrier for gallium–ammonia interactions[5.9].

Fortunately, switching the group V source to an ECR nitrogen plasma and maintaining the TEG, analogous to metal organic MBE, succeeds in buffer layer deposition at 450 C, lower than any other method attempted. However, carbon and oxygen peaks appear in the TOF–MSRI spectrums. Annealing the buffer layer removes the carbon contamination, but the oxygen peak still prevails, consistent with the Ga–C bond being weaker than either Ga–N or Ga–O [5.9].

Once the buffer layer is firmly established, returning to chemical beam epitaxy yields GaN films, with carbon incorporation varying with substrate temperature and TEG/ ammonia source ratios. Above 750 C, a transition occurs in the growth mode from polycrystalline to single crystal morphology. As the carbon incorporation increases, the crystal quality deteriorates[5.9].

5.7 Surface Phenomenon

A collaboration between the Fritz–Haber Institute and Xerox Palo Alto Research Center produced some meaningful results surrounding the GaN growth surface. They applied first principles density function theory to evaluate: different GaN surface structures, unintentional arsenic doping, and adatom diffusion rates[5.10].

Because N atoms have small radii relative to Ga, the Ga spacing in GaN is only slightly larger than pure Ga. Under these circumstances, Ga atoms on the GaN surface favor metallic bonds among themselves, which are only slightly weaker than pure Ga, rather than traditional semiconductor materials, which form dimers and trimers between surface atoms[5.10].

A majority of GaN surfaces are Ga terminated because: 1) metallic bonds extend to the surface to support excess Ga, and 2) nitrogen molecules exhibit one of the strongest bonds between two atoms in nature, limiting the chemical potential elsewhere. Other than a Ga–N bond at the GaN interface, N adatoms are undercoordinated on the surface, making them less stable than a free nitrogen molecule[5.10].

This reinforces what the Russian scientists observed earlier when they described a physisorption precursor[5.6]. If a nitrogen molecule is already sitting in a deep potential energy well, then it must surmount an formidable barrier before it can bond to Ga as Ga–N. In addition, substantial reaction barriers imply dramatic configurational changes must take place in the transition state before the reaction can go forward.

Experimentalists growing cubic GaN on GaAs observe surface reconstructions which can only be stable if arsenic resides on the surface throughout GaN growth. As figure 5.7 illustrates, density functional theory can account for this behavior. The different curves represent the GaN surface energy changes with arsenic coverage for the three most common GaN growth planes: (0001), $(000\bar{1})$ wurtzite, and (001) zinc blende; using solid, dashed, dotted lines, respectively[5.10].

For wurtzite structures, the energy reaches a minimum at 0.25 monolayer arsenic coverage, but turns positive prior to full saturation. The energy difference between the two wurzite minimums can be rationalized by the number of Ga dangling bonds: one for (0001) and three for $(000\bar{1})$, as seen in figure 5.8. With more dangling bonds, one should expect higher impurity levels growing on $(000\bar{1})$ surfaces relative to (0001), which will ultimately compromise film quality[5.10].

In contrast, the (001) cubic surface approaches an energy minimum at 0.5 monolayer arsenic coverage, and stays negative through full saturation. The energy minimum at 0.5 monolayer coverage corresponds to a (2x2) arsenic dimer surface. Because the solubility of arsenic is extremely low in GaN, and the surface energy is negative regardless of coverage, arsenic behaves like a model surfactant for the (001) surface. Due to positive surface energy ranges in the wurtzite structures, arsenic's surfactant potential is questionable in the hexagonal realm; however, the authors have been unable to find any experimentalists willing to test this hypothesis[5.10].

To address diffusion issues on GaN surfaces, the collaborators compared diffusion pathways for Ga and N adatoms on a clean Ga terminated surface. Although figure 5.9 only depicts a zinc blende surface structure, the picture is qualitatively the same for all GaN surfaces. An N adatom prefers its normal epitaxial site between two Ga atoms; whereas, a Ga adatom favors a 4–fold hollow site, the same position it would occupy in bulk GaN, without the N atoms present. The diffusion barriers between the two adatoms differ significantly, based on bonding characteristics; Ga–Ga bonds have fairly weak undirected metallic bonds, in comparison to Ga–N bonds, which have strong directional covalent behavior. The fundamental difference in surface bonding means that the Ga adatom is dramatically more mobile than its N adatom counterpart[5.10].

Accordingly, the consequences of adatom diffusivity on GaN growth can be postulated. Ironically, the diffusion barrier is so high for N atoms, they are kinetically hindered from desorption, which can only take place if they find a partner, to desorb as molecular nitrogen. Under Ga rich conditions, the highly mobile Ga atoms insure N atom capture probability, long before the N atoms have a chance to recombine and evolve away.

If an N rich condition is allowed to prevail, calculations show that the surface becomes kinetically stagnated with N atoms, which slows down the Ga atom diffusivity. When the Ga atoms are kinetically limited: 3–D growth, stacking faults, surface roughening, and faceting become more likely, jeopardizing the film morphology. Finally, the extreme binding energy for molecular nitrogen and the large disparity in atomic radii, which drive polar surfaces to be Ga rich, are general characteristics inherent to other III–V nitride structures, such as AlN, InN, and any prospective alloys[5.10].

5.8 Conclusion

Optimum GaN growth occurs in a molecular beam environment with equal III–V flux ratios in a 750 to 800 C temperature range. The stability of GaN and other nitrides can be attributed to a physisorption precursor, which testifies to the strength of the barrier between molecular nitrogen and GaN. To overcome this barrier, a wide range of N atom sources have been deployed, including: microwave plasma ECR, radio frequency plasma, ion beams, and ammonia catalysis. GaN morphology can range from cubic to hexagonal, with Ga face polarity preferred in the wurtzite case. Ga face polarity has fewer dangling bonds, reducing contaminants, and is less likely to decompose than N face polarity. Regardless of polarity, a Ga terminated surface is favored thermodynamically, based on the unique bonding character of the III–V nitrides. Fortunately for crystal growers, a Ga terminated surface kinetically hinders N adatom recombination/ evolution, and fosters Ga diffusivity, leading to smoother, lower defect films.

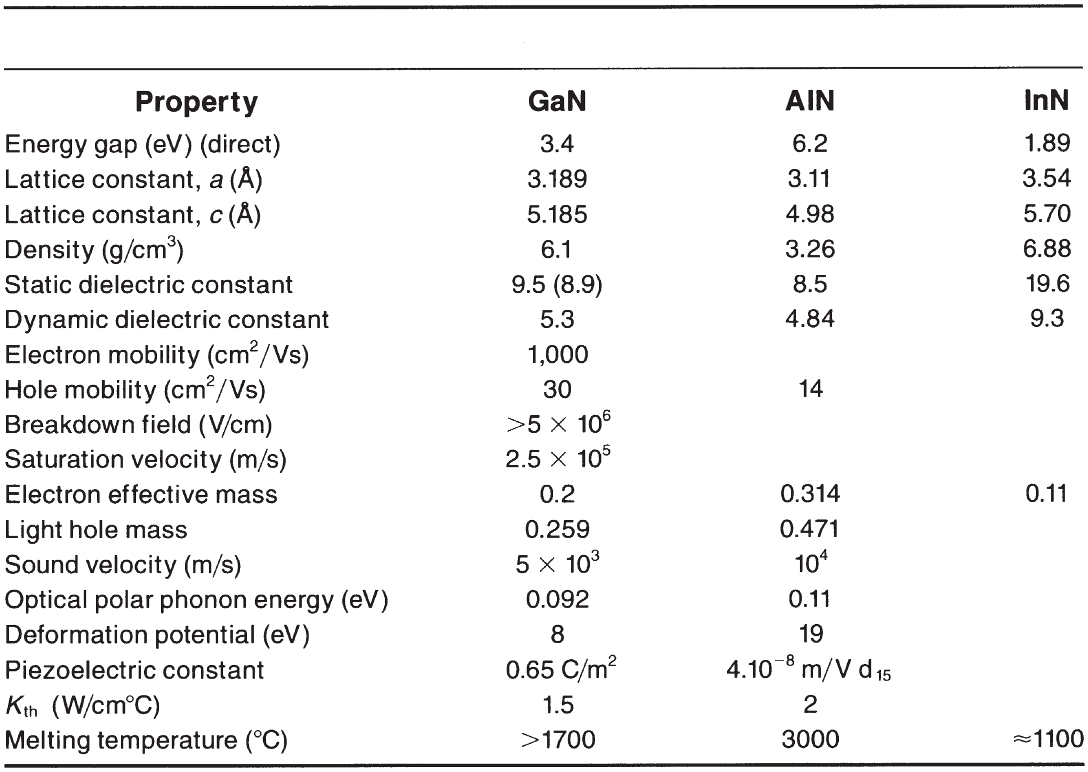

Property	GaN	AlN	InN
Energy gap (eV) (direct)	3.4	6.2	1.89
Lattice constant, *a* (Å)	3.189	3.11	3.54
Lattice constant, *c* (Å)	5.185	4.98	5.70
Density (g/cm^3)	6.1	3.26	6.88
Static dielectric constant	9.5 (8.9)	8.5	19.6
Dynamic dielectric constant	5.3	4.84	9.3
Electron mobility (cm^2/Vs)	1,000		
Hole mobility (cm^2/Vs)	30	14	
Breakdown field (V/cm)	$>5 \times 10^6$		
Saturation velocity (m/s)	2.5×10^5		
Electron effective mass	0.2	0.314	0.11
Light hole mass	0.259	0.471	
Sound velocity (m/s)	5×10^3	10^4	
Optical polar phonon energy (eV)	0.092	0.11	
Deformation potential (eV)	8	19	
Piezoelectric constant	0.65 C/m^2	4.10^{-8} m/V d_{15}	
K_{th} (W/cm°C)	1.5	2	
Melting temperature (°C)	>1700	3000	≈ 1100

Figure 5.1: Material parameters for the III–V nitrides.

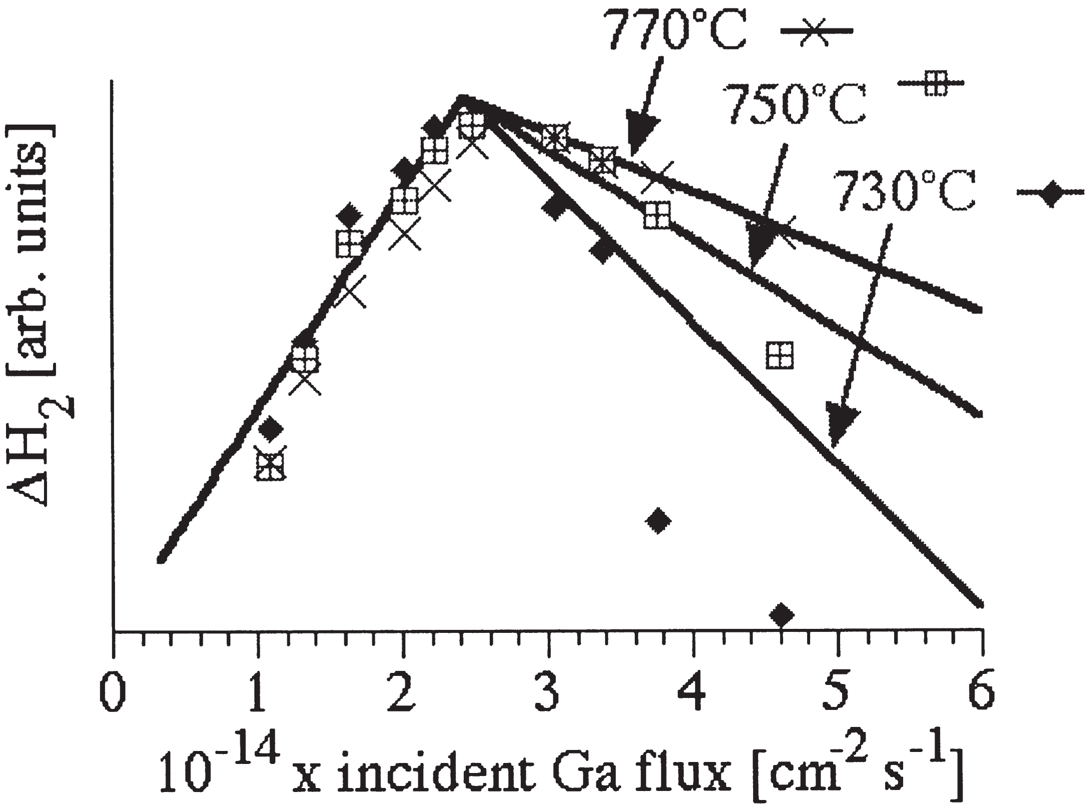

Figure 5.2: GaN growthrate, measured by hydrogen evolution, in relation to Ga flux for a constant ammonia flux. The lines give a theoretical comparison to the experimental points.

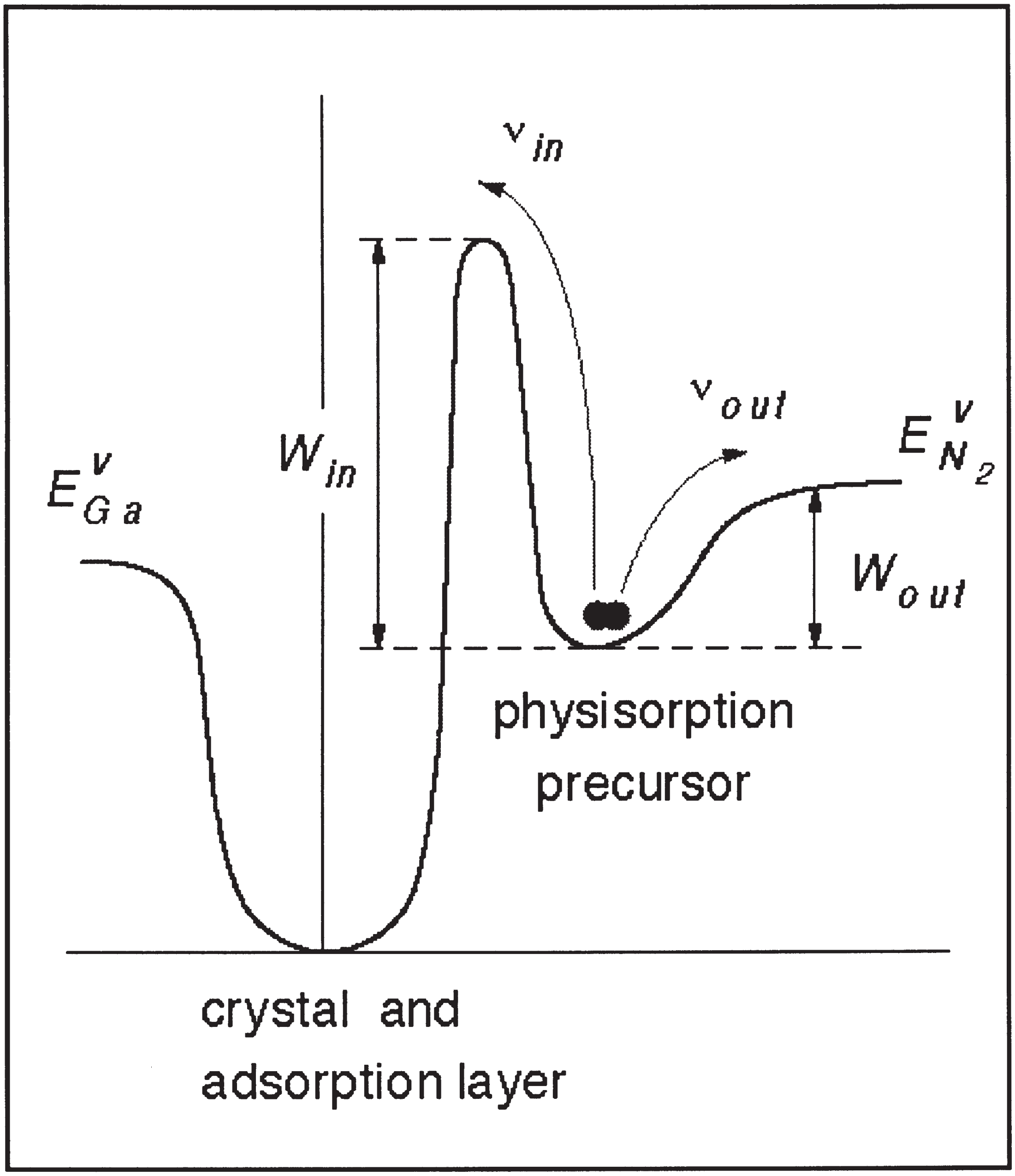

Figure 5.3: Potential energy coordination diagram for GaN formation depicting the massive physisorption barrier for nitrogen.

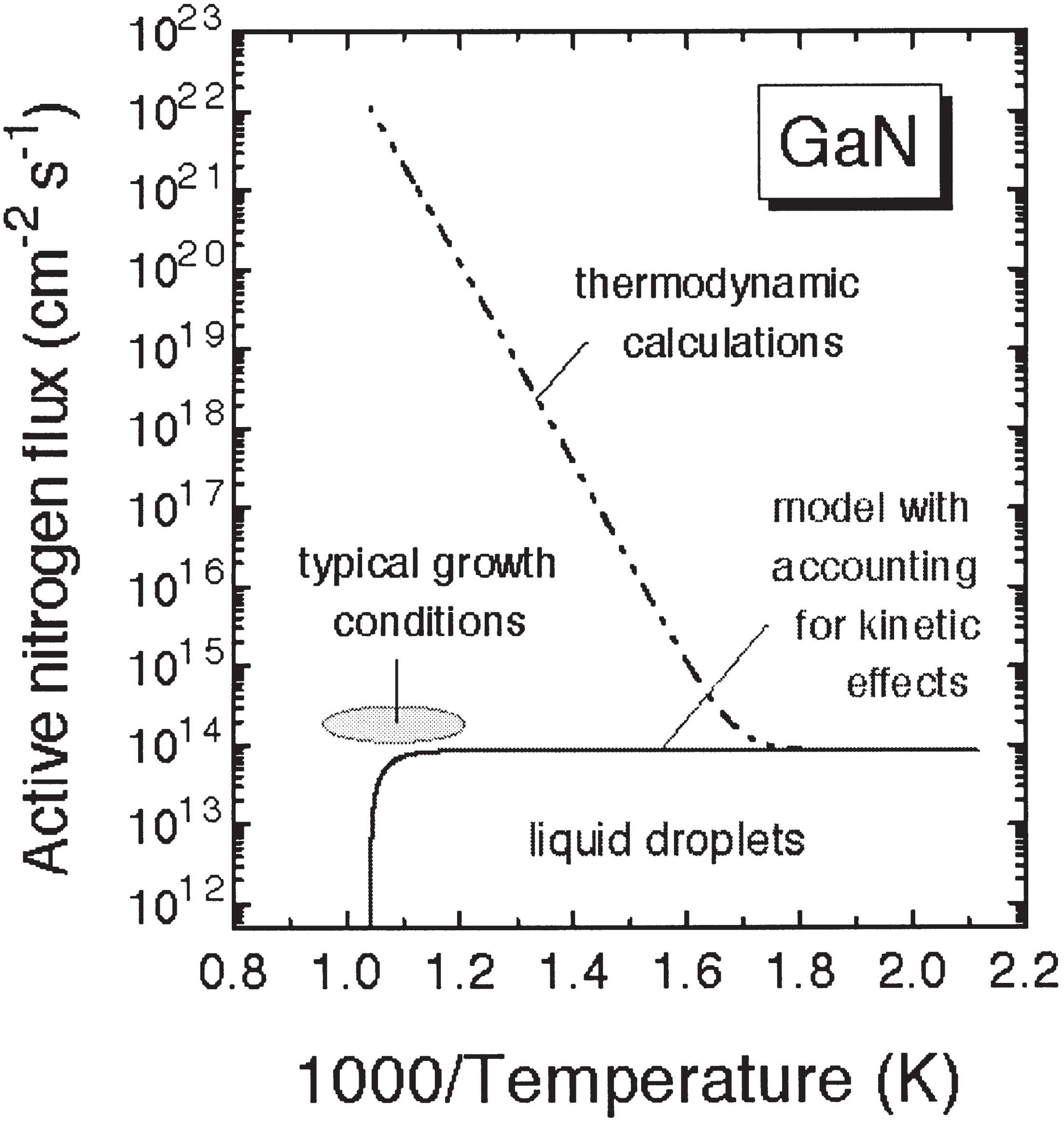

Figure 5.4: Phase diagram illustrating the GaN liquid/ solid interface for various growth conditions, with (kinetic) and without (thermodynamic) a nitrogen physisorption barrier.

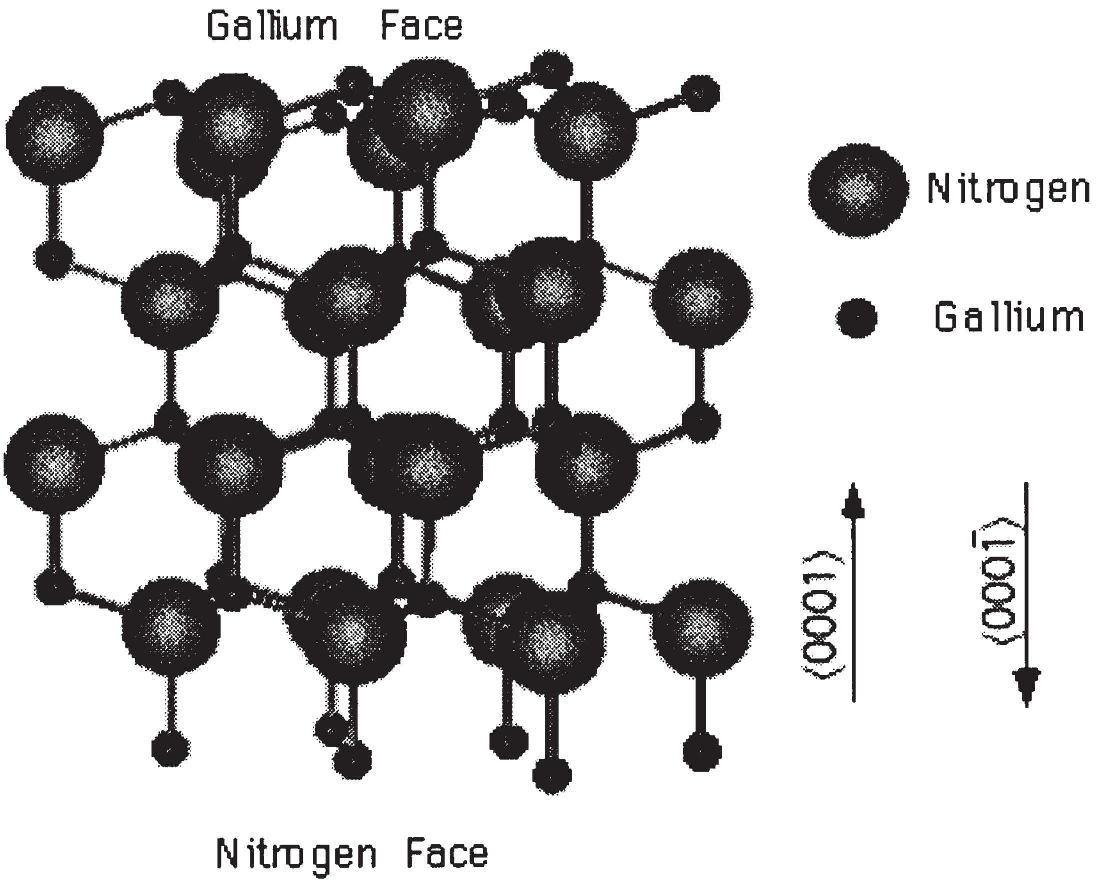

Figure 5.5: Hexagonal GaN wurtzite lattice showing polarity conventions.

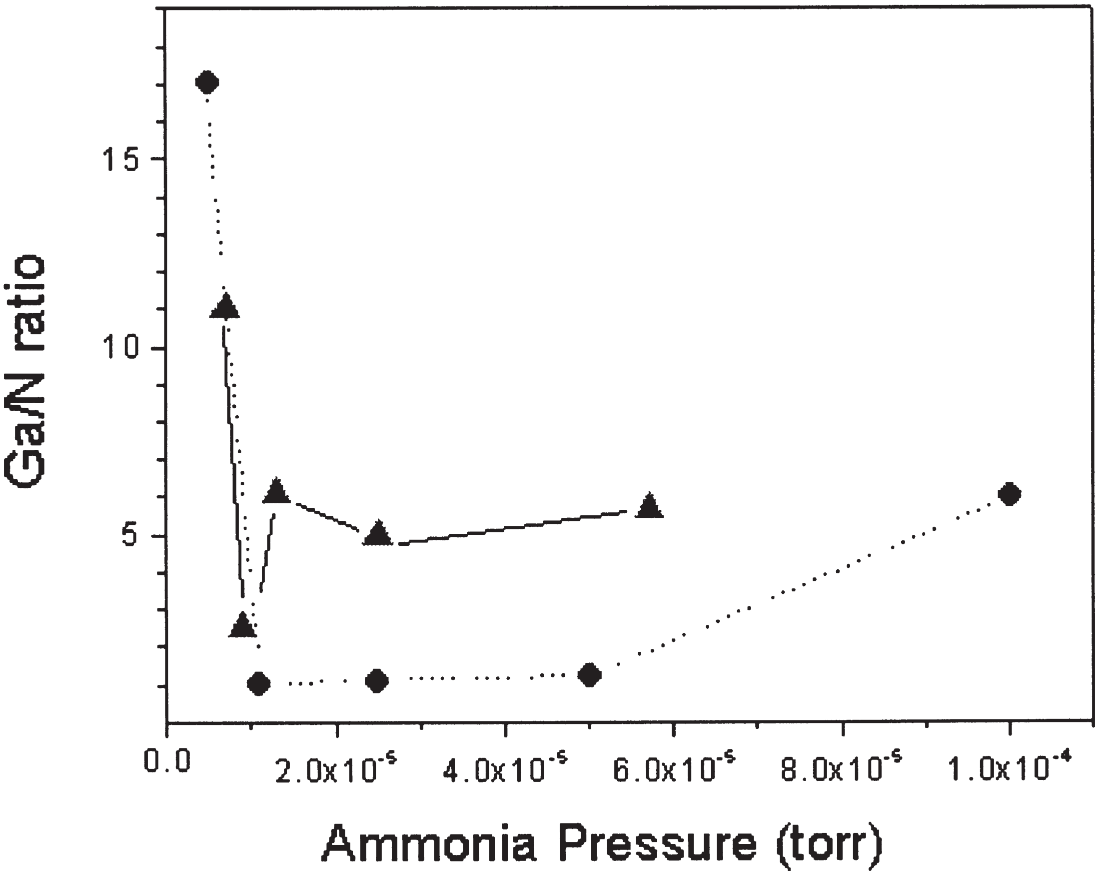

Figure 5.6: Ga to N peak intensities measured on the surface during GaN growth at a low Ga flux, circles, and a high Ga flux, triangles, in comparison to ammonia flux variations.

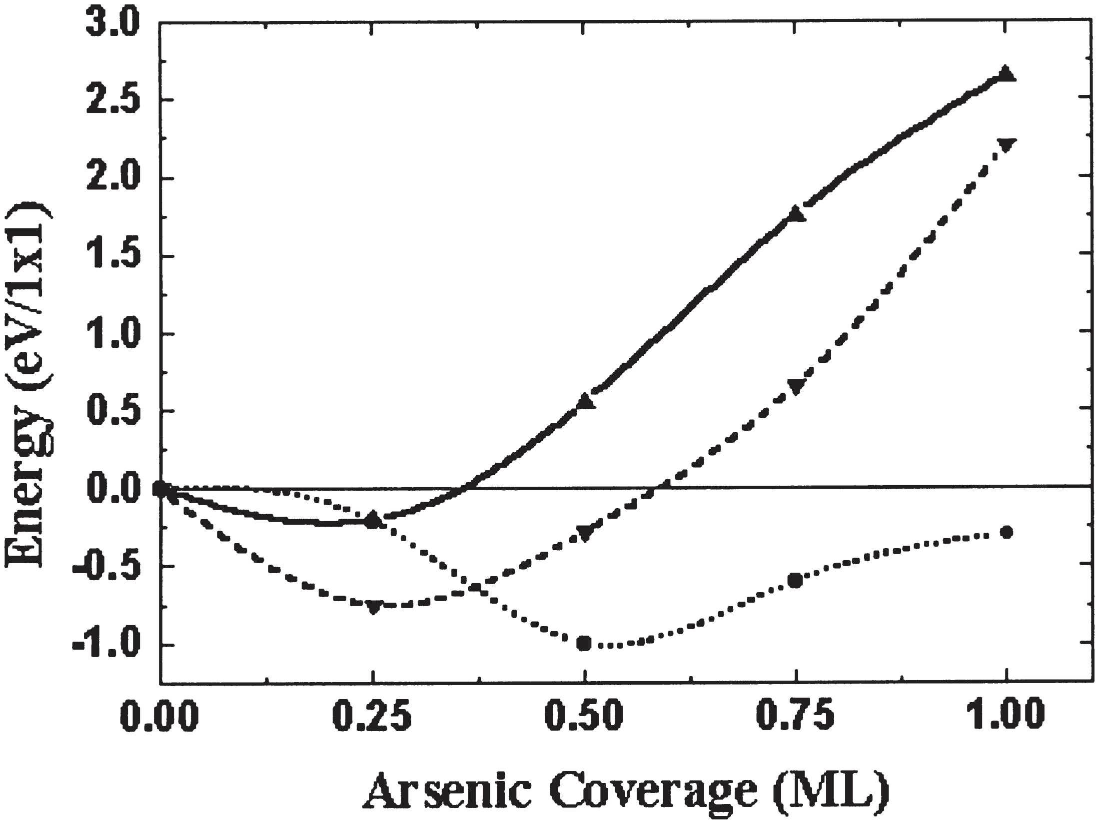

Figure 5.7: Surface energy change for (0001), ($000\bar{1}$), and (001) GaN surfaces, using solid, dashed, and dotted lines, respectively, as a function of arsenic monolayer coverage.

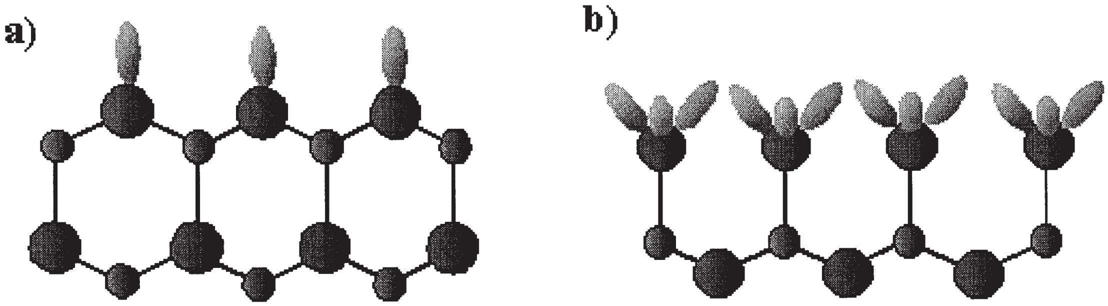

Figure 5.8: GaN surface structure for; (a) Ga face and (b) N face polarities, highlighting dangling bond features from a Ga terminated surface.

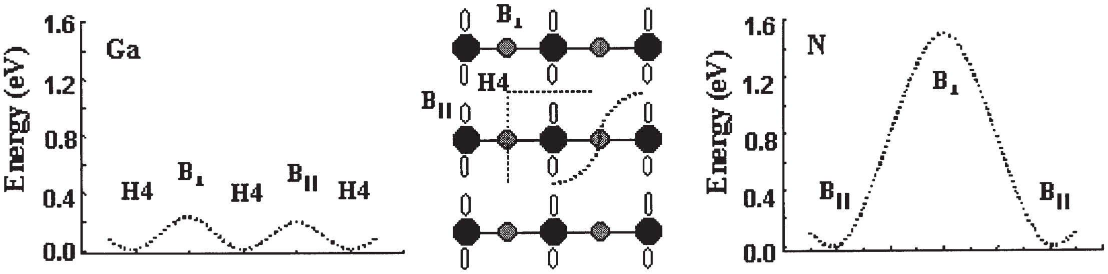

Figure 5.9: Energy diagrams and diffusion pathways for Ga and N adatoms on a (001) GaN surface, where diffusion pathways are marked by dotted lines, large atoms are Ga, and small atoms are N.

References

[5.1] S. N. Mohammad, et al., *MRS Bulletin*, **2**, 22 (1997).

[5.2] R. Singh, et al., *MRS Internet Journal of Nitride Semiconductor Research*, **3**, 13 (1998).

[5.3] B. Beaumont, et al., *MRS Internet Journal of Nitride Semiconductor Research*, **1**, 17 (1996).

[5.4] M. A. Sánchez–García, et al., *MRS Internet Journal of Nitride Semiconductor Research*, **3**, 32 (1998).

[5.5] D. E. Crawford, et al., *MRS Internet Journal of Nitride Semiconductor Research*, **1**, 12 (1996).

[5.6] M. V. Averyanova, et al., *MRS Internet Journal of Nitride Semiconductor Research*, **1**, 31 (1996).

[5.7] M. Kamp, et al., *MRS Internet Journal of Nitride Semiconductor Research*, **2**, 26 (1997).

[5.8] E. S. Hellman, *MRS Internet Journal of Nitride Semiconductor Research*, **3**, 11 (1998).

[5.9] E. Kim, et al., *MRS Internet Journal of Nitride Semiconductor Research*, **3**, 22 (1998).

[5.10] T. Zywietz, et al., *MRS Internet Journal of Nitride Semiconductor Research*, **3**, 26 (1998).

6

Experimental Research

6.1 Introduction

The research I performed fell into three distinct categories: substrate temperature calibration, GaP deposition enhancement, and preliminary GaN growth. Since the dielectric constant for Si is known over a wide temperature range and wavelength spectrum, changes in reflectivity can yield substrate temperature. Due to the construction and installation of a new plasma tube, experiments dealing with activated species can now take shape for GaP heteroepitaxy in the molecular beam growth system. Finally, some preliminary studies were carried out that point to a potential GaN growth strategy on Si using TEG and nitrogen plasma source beams.

6.2 Approach

As seen in figure 6.1, the growth apparatus is an ultra high vacuum chamber, pumped by turbomolecular pumps to an ultimate base pressure in the low 10^{-9} Torr range, with a growth pressure of about 5×10^{-5} Torr under a 6 sccm gas load. A loadlock exists to preserve the growth chamber vacuum integrity. The chamber has variety of gas sources, including: TEG, TBP, hydrogen, and nitrogen, with the capability to mix hydrogen among all the other vapors. Independently, source gases can be directed into the main growth chamber or a separate bypass chamber for bleeding off excess reactants. While filament excitation is available for TEG and TBP precursor sources, an RF plasma tube can activate hydrogen and nitrogen gas streams. A custom built in–house project, the plasma tube has a 25 mm diameter, 100 mm length, 1.5 mm orifice, and a 150 mm pathlength from the orifice to the substrate. Copper tubing, 1/8 inch diameter, coiled around the exterior tube wall, delivers the RF power to the gases at 13.56 Mhz. For a mass flowrate of 5 sccm passing through the tube, design calculations would suggest a pressure on the order of 100 mTorr. A two inch diameter Si substrate faces down on a radiatively coupled heating stage, whose heat is generated by DC resistance through a Mo plate. A generous number of optical ports afford dual plane polarized reflectance spectroscopy measurements, which we choose 75 and 70 degree incident angles, at and below the pseudo–Brewster angle of Si, for a wavelength of 632.8 nm. In addition to the reflectometry components described in chapter 4, a chopper and lock–in amplifier have been added to filter out stray low frequency light. Unfortunately, the reflection high energy electron diffraction (RHEED) power supply was inoperative, so crystallographic surface information could not be collected. For all experiments, the Boron doped p–type Si(100) substrates were given an RCA clean, a full strength HF dip for one minute, a deionized water rinse, and a nitrogen purge, prior to loadlock introduction.

Temperature calibrations were carried out in the molecular beam chamber with just hydrogen gas flowing at 5 sccm to simulate normal growth conditions and preserve Si surface conditions at elevated temperatures. The DC voltage ranged between 3 and 33 V on the Mo heater plate as the current was raised from 3 to 12 A in 1 A steps at 600 s intervals. Reflectivity measurements were made at 75 degrees under PRS conditions, and plotted out thereafter, to visually average intensity values.

The most challenging step in the data processing of the temperature measurements is the generation of the Fresnel curve, which proceeds in the following manner. For an interface between two distinct mediums, the general complex reflectivity is:

$$r_{k,k+1} = \frac{\varepsilon_{k+1}\sqrt{\varepsilon_k - \varepsilon_1 \sin^2\phi_1} - \varepsilon_k\sqrt{\varepsilon_{k+1} - \varepsilon_1 \sin^2\phi_1}}{\varepsilon_{k+1}\sqrt{\varepsilon_k - \varepsilon_1 \sin^2\phi_1} + \varepsilon_k\sqrt{\varepsilon_{k+1} - \varepsilon_1 \sin^2\phi_1}}$$

where: r = *complex reflectivity or Fresnel coefficient*
ε = *overall dielectric constant*
ϕ = *incident angle from the normal*

Since the dielectric constant of the ambient is defined as, $\varepsilon_1 = 1$, and the only interface under consideration is between the ambient and the Si substrate, the Fresnel coefficient simplifies to:

$$r_{1,2} = \frac{\varepsilon_2\sqrt{1 - \sin^2\phi_1} - \sqrt{\varepsilon_2 - \sin^2\phi_1}}{\varepsilon_2\sqrt{1 - \sin^2\phi_1} + \sqrt{\varepsilon_2 - \sin^2\phi_1}} = \frac{a - b}{a + b}$$

$$\begin{array}{lccl} \textit{define:} & a & = & \varepsilon_2\sqrt{1 - \sin^2\phi_1} \\ & b & = & \sqrt{\varepsilon_2 - \sin^2\phi_1} \end{array}$$

From the literature, the dielectric constant for Si as a function of temperature fits an empirical relationship[6.1][6.2]:

$$\varepsilon_2(\Re) = 15 + 2.1x10^{-3}T + 1.5x10^{-6}T^2$$

$$\varepsilon_2(\Im) = 0.132e^{0.0025T}$$

$$\begin{array}{lll} \textit{where:} & \Re & \textit{denotes real} \\ & \Im & \textit{denotes imaginary} \\ \textit{with:} & T & \textit{in} \quad [C] \end{array}$$

Once the Fresnel coefficient has been evaluated for a particular temperature, the true reflectance is a product of the complex reflectance and its conjugate:

$$R = rr^*$$

Figure 6.2 demonstrates the true reflectance as a function of temperature for the Brewster angle of Si, $\phi_1 = 75$ degrees at $\lambda = 632.8$ nm. With the Fresnel curve, reflectance values can be associated with temperatures, so the last task is to relate a measured reflectance intensity to a true reflectance. By definition:

$$R = \frac{I}{I_o}$$

$$\begin{array}{lcll} \textit{where:} & R & = & \textit{true reflectance} \\ & I & = & \textit{reflectance intensity} \\ & I_o & = & \textit{beam intensity} \end{array}$$

Since the reflected intensity can be measured at room temperature, it provides a reference temperature to obtain the true reflectance from the Fresnel curve and establish the beam intensity. Thereafter, the beam intensity serves as a constant which connects a measured reflectance intensity to true reflectance. Then, the procedure encompasses measuring a raw reflected intensity, converting that value to a true reflectance through the beam intensity, and consulting the Fresnel curve to ascertain the temperature.

The mass flow parameters relevant to GaP heteroepitaxy experiments were:

Pressure = 5×10^{-5} *Torr*
H_2 = *5* *sccm*
TBP = *0.8*
TEG = *0.04*

Pulsing:	Main	Bypass
TBP	0 → 0.8 s	
TEG	1.5 → 1.8	1.8 → 2.5

During an overall growth cycle of 3 s, TEG flows into the main growth chamber for 0.3 s, is vented into a separate bypass chamber for 0.7 s, and has an accumulated flux to the surface:

$$NetTEG = 0.04sccm\left(\frac{2.3s}{3s}\right) = 0.031sccm$$

Therefore, the realized TBP/TEG flow ratio becomes 26. For all deposition runs, the sequence of events proceeded as follows:

t=	*0 s*	*Initiate continuous TBP flow to growth chamber* *and continuous TEG flow to bypass.* *Raise heat to 8 A ⇨ PRS Temp = 490 C.* *Charge up filament or ignite plasma (if applicable).*
	900	*Lower heat to 7 A ⇨ PRS Temp = 380 C.*
	1800	*Begin vapor source pulsing.*
	2000	*PRS 75 shows signs of growth.*
	5400	*Turn off heat.* *Resume continuous TBP flow to growth chamber* *and continuous TEG flow to bypass.*
	7200	*Deactivate filament or extinguish plasma (if applicable).* *Shut off gases.*

Up until this point, all the variables remained constant. The objective of this GaP series was twofold: 1) to determine the influence of TBP precracking through a filament, and 2) to see how a hydrogen plasma beam modifies film growth. Since the hydrogen flow is coupled to the TBP stream, hydrogen was activated by the filament as well. One GaP film was grown without either the filament or the plasma to serve as a baseline for comparison. For a voltage span of 6 to 12 V AC, filament powers ranged from 16 to 49 W. In order make room for GaN studies, only one GaP plasma experiment was performed, with a net power of 49 W delivered to the hydrogen stream.

For an exploratory look at GaN growth, hydrogen and nitrogen gases were passed through the RF plasma tube. The deposition strategy was to start with a standard GaP run, as outlined above, then gradually shift over to GaN by: increasing the nitrogen flow through the plasma, scaling back the TBP flow, and raising the substrate temperature. In accordance with the GaP/ hydrogen plasma run, the plasma was ignited at the beginning of the experiment. If GaN growth was achieved, modulate the process variables, such as: plasma power, substrate temperature, and gas flows to optimize deposition conditions.

6.3 Results and Discussion

As figure 6.3 reveals, the plane–polarized reflectance signal at 75 degrees was extremely responsive to temperature fluctuations. It's not clear what happened between 4500 and 5500 s, when the signal experienced a little turbulence dwelling in the 600 C range, but substrates have been known to shift position during heat up as the aluminum oxide holder expands. Unfortunately, no other surface probes, such as the RHEED or the PRS at 70 degrees were running at the time to collaborate this temporary deflection. Another possible cause might be in the power supply itself, since incoming power lines have been known to fluctuate throughout the day as loads on the system changed. If the calibration had been run more times, the data might be more conclusive.

Never the less, figure 6.4 illustrates the temperature values derived from the Fresnel curve, after the raw reflectivity measurements were scaled by the incoming beam intensity. Although current and voltage curves could be generated by this data, power was chosen as the independent variable to take into account future resistivity changes in the Mo heater. However, this calibration should not discount the possibility that the Mo heater experiences radiative changes over time as: the surface becomes contaminated, the Mo evaporates incongruently, the gas environment differs, or the surface texture modifies emissivity. Therefore, periodic renewal of these temperature measurements is advisable.

In order to calibrate these reflectivity measurements to an absolute temperature, Hellman[6.3] has noted that an oxide free Si(111) surface exhibits a surface reconstruction from 7x7 to 1x1 at a transition temperature of 830 C. Five degree increments above and below the transition temperature yield distinctly unique RHEED patterns. Clearly, this gives an added incentive to clarify the RHEED situation in our chamber.

GaP deposition enhancement through filament precracking of TBP or hydrogen plasma excitation are summarized in figures 6.5 through 6.7. They look at reflectivity at 75 degrees, reflectivity at 70 degrees, and laser light scattering, respectively, or more briefly: PRS 75, PRS 70, and LLS. Recall that the filament activation contains a mixture of both TBP and hydrogen; whereas, the plasma is exclusive to hydrogen, so two individual excitation channels are explored.

Relative to the baseline sample, precracking the TBP with the filament at 6 V may have slightly enhanced the deposition rate, but anything beyond that voltage level caused a progressive decline in growthrate. This trend is clearly evident in the PRS 75 and PRS 70 curves by noting the shift in the maxima and minima positions with respect to time. In perspective, it might have been more interesting to pursue the voltage range below 6 V, to determine where the TBP excitation maximizes GaP growth.

Alternatively, the hydrogen plasma beam didn’t have a significant influence on growthrate, but the scattered light intensity reveals a considerably smoother film development than the reference sample. Because the growthrate didn’t change, it implies that etching is not dramatic component at this power level, or that growth enhancement is balanced out by the etch rate. The symmetrical shape of the first PRS 75 peak confirms that the hydrogen plasma shortens the nucleation period, relative to any of the other films. In heteroepitaxy, the area under the shoulder of the initial PRS 75 peak gives an indication of the nucleation time. It represents a period when the dielectric constant of the film is averaged out between the nuclei and the ambient. Some of the shoulders in the other PRS 75 curves are obscured by the maxima, but for those cases, like the filament settings at 10 and 12 V, the first peak is wider to account for that.

With scattering intensity, it’s easy to compare smoothness between the baseline sample and the plasma enhanced film, because the deposits achieve equal thickness. Since the defects in a film accumulate throughout growth, the deposition morphology coarsens as thickness progresses. In the filament group where thickness varies, texture is somewhat difficult to evaluate, because the scattered signal correlates with the film thickness. Conceivably, the defect density among the filament samples could be about the same magnitude, but a new series restoring thickness parity would address this uncertainty.

There's still a fundamental question whether the plasma's influence on nucleation defines the subsequent film growth, or it somehow provides an ongoing therapeutic effect throughout growth. A simple experiment where the plasma is shut off after the first PRS 75 fringe might discern the overall impact. In the developmental chapters of my thesis, I stated that illumination, ion collisions, and electron bombardment collectively increase the adatom mobility, improving every aspect of growth, unless the bombardment causes morphology damage at the surface. Again, this damage could be subverted if the defects created are annealed out faster than they are generated. Since the etch rate appears to be insignificant for the power level used, the plasma likely fosters crystal integrity throughout deposition. In diamond growth, the hydrogen plasma selectively etches away graphite, allowing the metastable diamond phase to kinetically persevere. Perhaps the hydrogen plasma beam etches away energetically weak defects and enhances adatom mobility, shifting the balance in favor of thermodynamics.

The deterioration in growthrates at higher filament voltages may suggest an upper limit where high energy particles become detrimental to film morphology. Even though the plasma and filament powers are on the same order, the filament volume is considerably smaller, allowing the filament to exert a higher power density on the gaseous species. With the difference in frequency between the plasma and filament power supply, RF versus AC, it's risky to compare power levels quantitatively, but remember, the filament gas stream contains TBP. If the filament provides too much energy, the TBP surface fragments might have a shorter residence time on the substrate or could react more vigorously, rendering less favorable growth products. A scenario where the tertiary butyl group unleashes multiple carbon radicals less viable than the parent radical could devastate GaP growth. Activated hydrogen mixed in with the TBP could yield phosphine as they collide together on the filament, raising the phosphorous reaction barrier on the growth surface. An elemental analysis where carbon and phosphorous content is measured throughout the whole GaP series may validate my concerns about the filament and see if the plasma influences composition.

To review the GaN surface studies, let's observe the standard GaP/ hydrogen plasma run, figure 6.8, to understand what normally happens during growth. In fact, this experiment represents the raw data used to generate the hydrogen plasma curves in the GaP series. The reflectivity at 75 degrees starts at a minimum along the baseline of the graph, as does the scattered light intensity. In contrast, the PRS 70 signal is almost saturated out, because it is 5 degrees away from silicon's pseudo–Brewster angle, so it's value is most sensitive to temperature fluctuations during the pregrowth regime. As deposition commences, the PRS 75 signal is most responsive, because $\frac{\Delta R}{R}$, the change in reflectivity over its absolute value, when R is at a minimum, will amplify a shift. Because only diffuse light from the surface can contribute, the scattered intensity helps to differentiate between surface roughness and interface roughness, which the reflectivity measurements integrate together. At a wavelength of 632.8 nm, the light beam penetrates to the interface, since it is below either the substrate or film band gap. Although the surface reaction layer oscillations, the fine structure, is somewhat blurred out at this resolution, the envelope near the maxima and minima is more pronounced on the PRS 75 signal in accordance with $\frac{\Delta R}{R}$.

There's contradicting trends in the gross interference fringe maxima; the PRS 70 signal declines from peak to peak, while the PRS 75 signal ascends. Intuitively, I would attribute this to preferential crystal texture aligning to various planes during film growth, even though we're dealing with epitaxial layers. Equally puzzling is a baseline shift for the PRS 75 signal, when the PRS 70 minima stay flat. Assuming the PRS 75 signal is more sensitive to the GaP film, relative to PRS 70, it might be revealing an interface transformation, hopefully not carbonation.

Finally, the scattered intensity has a plateau at about 4500 s, which corresponds to a thickness near 2400 Å. Without any other data to confirm this, it could indicate an elastic to plastic stress/ strain transformation, characteristic of lattice mismatch in heteroepitaxial growth. Despite the overall scattering pause at this solid angle, on a smaller scale the surface could be in transition. Again, a RHEED surface profile might yield more comprehensive insight into this phenomenon. Referring back to figures 6.5 through 6.7, the GaP excitation series, the scattering plateau is synchronous with the interference fringe positions, indicating a thickness dependence. To address this hypothesis, theoretical calculations can estimate where the critical thickness lies for the transformation in the GaP/ Si system. Experimentally, one might look for the same artifact with scatter measurements in homoepitaxial growth to dismiss the theory. A collection of thicker heteroepitaxy films without any further plateaus might corroborate this hypothesis, since only one such transition can take place.

Now that we have a sense for what happens during optimal GaP heterostructure growth, let's see what transpired when nitrogen was mixed into the hydrogen plasma beam, while maintaining standard TEG/ TBP pulse fluxes. Figure 6.9 depicts a first attempt at GaPN, where equal amounts of hydrogen and nitrogen flow through the plasma tube for a combined flow of 5 sccm, a substrate temperature of 380 C, and a plasma power setting at 5.0, which corresponds to about 50 W. By 2400 s, no deposition had occurred, so I cut back the plasma power to a setting of 1.0, equivalent to 8 W. The optical sensors each started their normal trends, but the growth behavior appeared somewhat restrained. After the normal growth time had expired, only half of a PRS 70 fringe had evolved. Since things looked hopeful, I decided to leave the same substrate in for subsequent growth, as figure 6.10 attests. My impression was that the nitrogen was suppressing deposition, so I adjusted the hydrogen/ nitrogen flow ratio through the plasma tube from 1 to 4, leaving the total flow at 5 sccm, the substrate temperature at 380 C, and a plasma power dwelling on 8 W. Again, the optical probes sprung into action, but it appeared that growth was tapering off. At this point, I changed the substrate temperature in incremental steps to: 490, 560, 620, 260, 170, 110 C, best captured by the scattered intensity plateaus after the 3500 s mark. Whatever deposition had started, self terminated, if I only knew what it was. In one last attempt, figure 6.11 shows an experiment where the plasma was kept at 50 W, the substrate temperature held at 380 C, and the hydrogen/ nitrogen flow ratios modified between 1 to 20, preserving the overall flow at 5 sccm. Although the film didn't progress as far as the previous runs, a fine structure superimposes itself on the PRS 75 signal. To summarize these initial GaPN attempts, the primary variant in each experiment corresponds to:

Figure	Run #	Variant
6.9	80507_1	RF power
6.10	80507_2	Substrate temperature
6.11	80511_1	H_2/N_2 flow ratio

Rather than try to sort out what deposited, I would like to draw from the wealth of knowledge compiled in this thesis to suggest a new GaN growth strategy. Despite the sensitivity afforded by the optical measurements, no evidence from them ever supported the likelihood of Si substrate nitridation. If the RHEED had been functional, it might have recognized a surface change. In retrospect, the plasma should not have been ignited with nitrogen flowing until GaP completely saturated the substrate. Let's review the constraints, then consider a strategy:

Constraints

1) *Nitrogen plasma exposure to Si substrate likely invokes nitridation.*
2) *TEG exposure without TBP present carbonates the Si substrate.*
3) *Neither GaN nor GaP favor growth on SiN or SiC if metalorganic precursors are involved.*
4) *TBP may catalytically enhance TEG decomposition.*

Strategy

1) *Set hydrogen flow to 5 sccm and ignite plasma.*
2) *Carry out GaP growth at 380 C until first peak of PRS 75.*
3) *Pause growth, extinguish plasma.*
4) *Set hydrogen flow to 4 sccm and nitrogen flow to 1 sccm, then ignite plasma.*
5) *Resume growth and ramp up substrate temperature to 750 C.*
6) *Unless growth stops, scale back TBP.*

Why not take advantage of the hydrogen plasma during the GaP buffer layer growth. Develop at least a 500 Å thick buffer layer to protect against etching or evaporation as the nitrogen plasma becomes established and the substrate heats up to an optimum GaN growth temperature at 750 C. Although it's improbable that TEG will still need a catalytic boost at 750 C, TBP flow should be diminished at a cautious rate watching its effect on the reflectivity sensors.

Unless SiC crystallites exist at the interface, experimentalists have observed that direct growth of GaN on Si(001) produces heavily polycrystalline material[6.4]. The majority of crystal growers favor an AlN or SiC buffer layer to achieve GaN epitaxial deposition on Si. In the GaN literature review, chapter 5, the buffer layer encompasses multiple functions, it may: provide stress relief at the interface, improve the lattice match, and/or establish the proper polarity. Under the constraints of metalorganic precursors, the SiC buffer layer would appear implausible. As for AlN, researchers have achieved GaN deposits on a nitrided sapphire substrate with TEG and MW–ECR nitrogen plasma beams[6.5].

If the GaN growth scheme outlined above does work, the question arises what crystal structure will dominate on a GaP buffer, wurtzite or zinc blende. Considering cubic GaN deposits on GaAs substrates[6.6], and GaP exhibits zinc blende behavior like GaAs, I would venture a guess that cubic GaN results. In contrast, GaN prefers hexagonal crystal habit on wurtzite AlN buffer layers[6.3]. Remember, cubic and hexagonal GaN polymorphs often grow simultaneously in an epitaxial layer, leading to stacking faults[6.4]. Unfortunately, the cubic lattice constant and thermal expansion coefficients aren’t readily available for GaN, in the most recent *CRC Handbook of Chemistry and Physics*, to serve as a comparison.

6.4 Conclusion

Until the reflectance temperature measurements of the Si substrate can be calibrated with a surface reconstruction temperature, like the 7x7 to 1x1 transition at 830 C for a Si(111) oriented wafer, it’s accuracy is in question. With the exception of the 6 V filament setting, TBP precracking reduced the growthrate of a GaP film. A hydrogen plasma seems to have no net influence on growthrate, but diminishes the nucleation time and enhances smoothness for GaP deposition on Si. A curious plateau appears in the scattered intensity signal at a thickness near 2400 Å, which could be an elastic to plastic stress/ strain transformation in heteroepitaxial growth, but deserves further attention. Under the constraints of metalorganic precursors, the best growth strategy of GaN on Si might include a GaP buffer layer with the current molecular beam configuration.

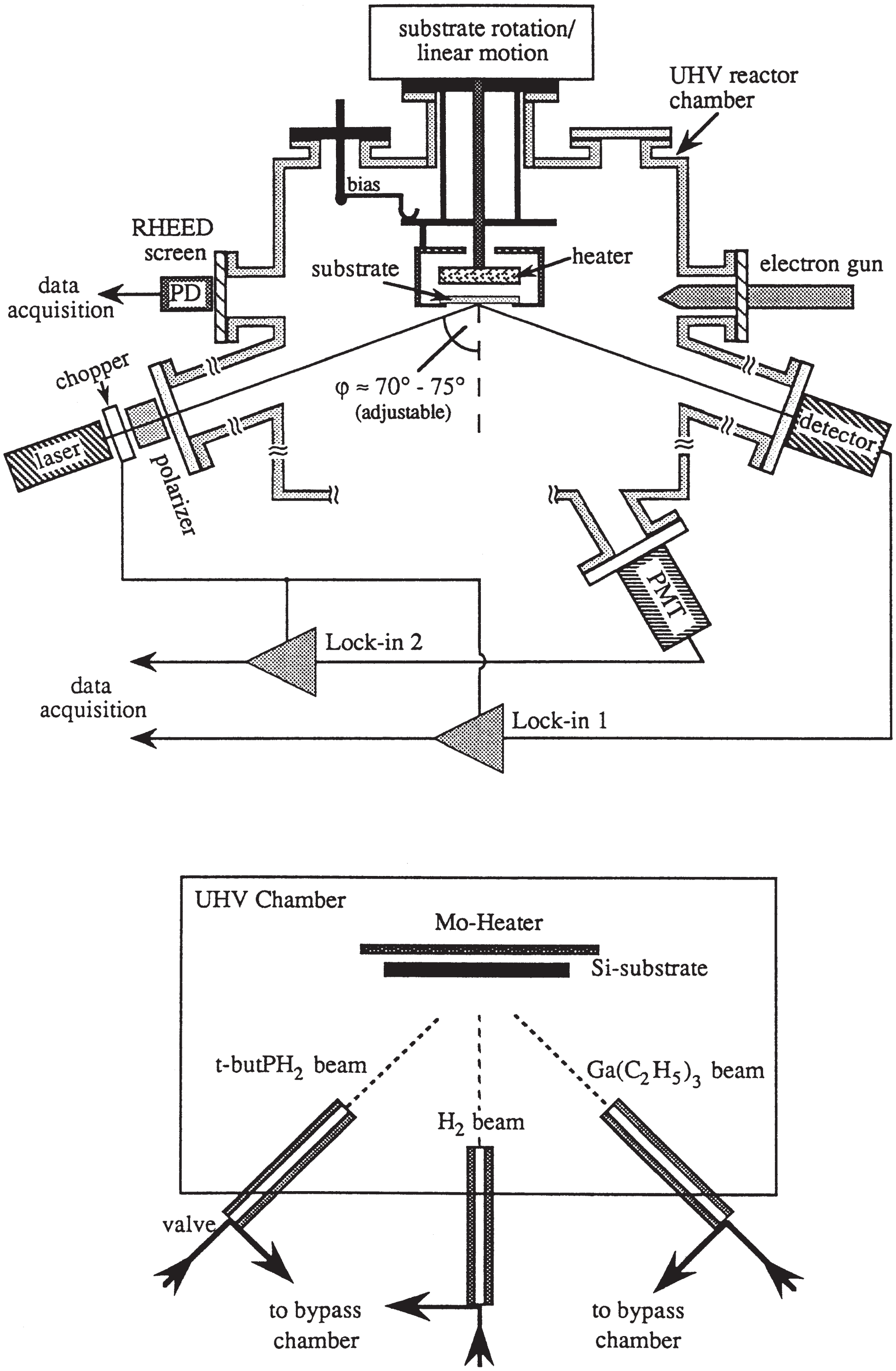

Figure 6.1: Instrumental (top) and dynamic (bottom) perspective of chemical beam epitaxy system.

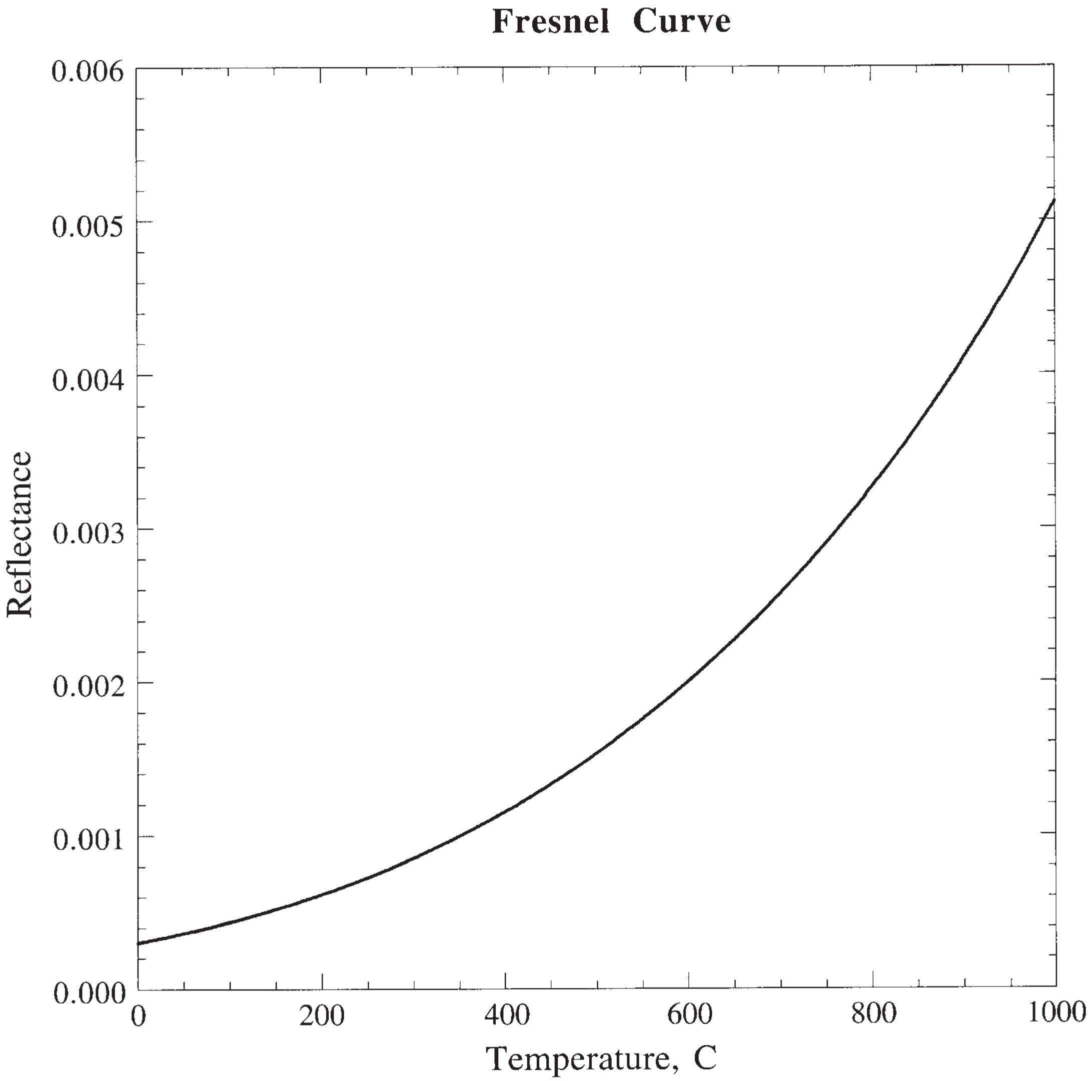

Figure 6.2: Fresnel curve for Si at the pseudo–Brewster angle of 75 degrees at 632.8 nm.

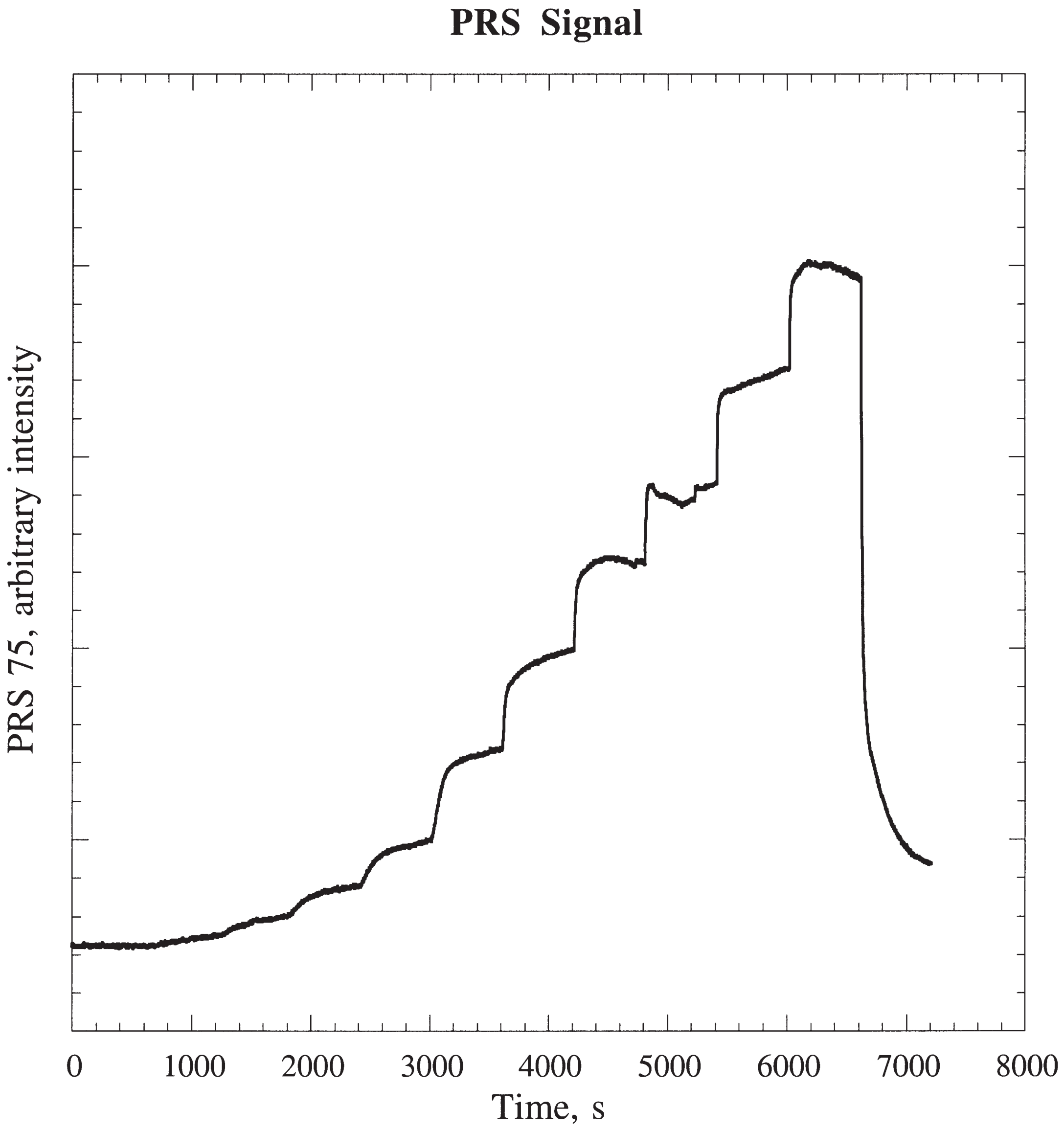

Figure 6.3: Raw reflectivity values measured from a Si substrate at discreet heater power settings.

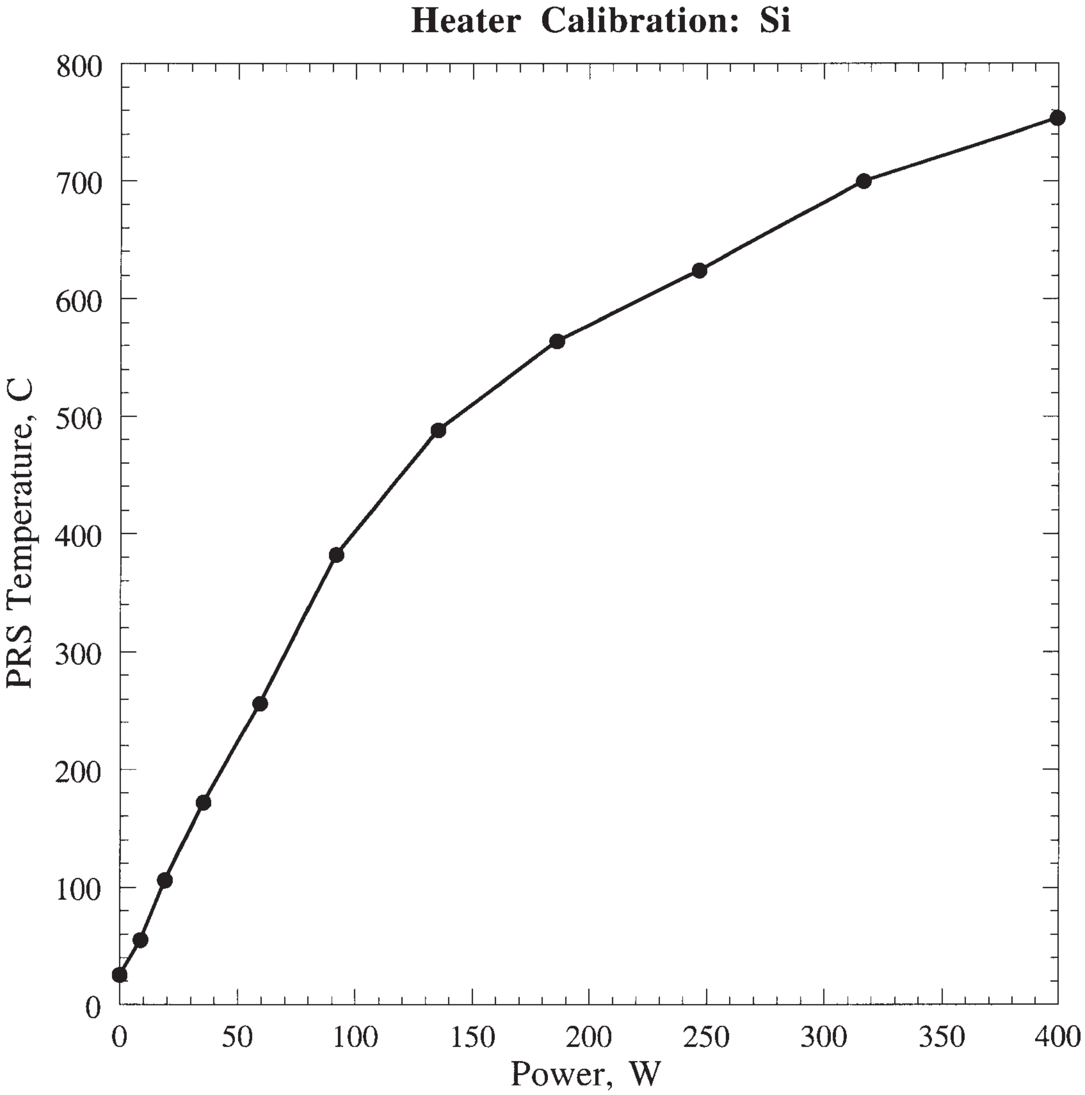

Figure 6.4: Calculated PRS temperature as a function of heater power for a Si wafer.

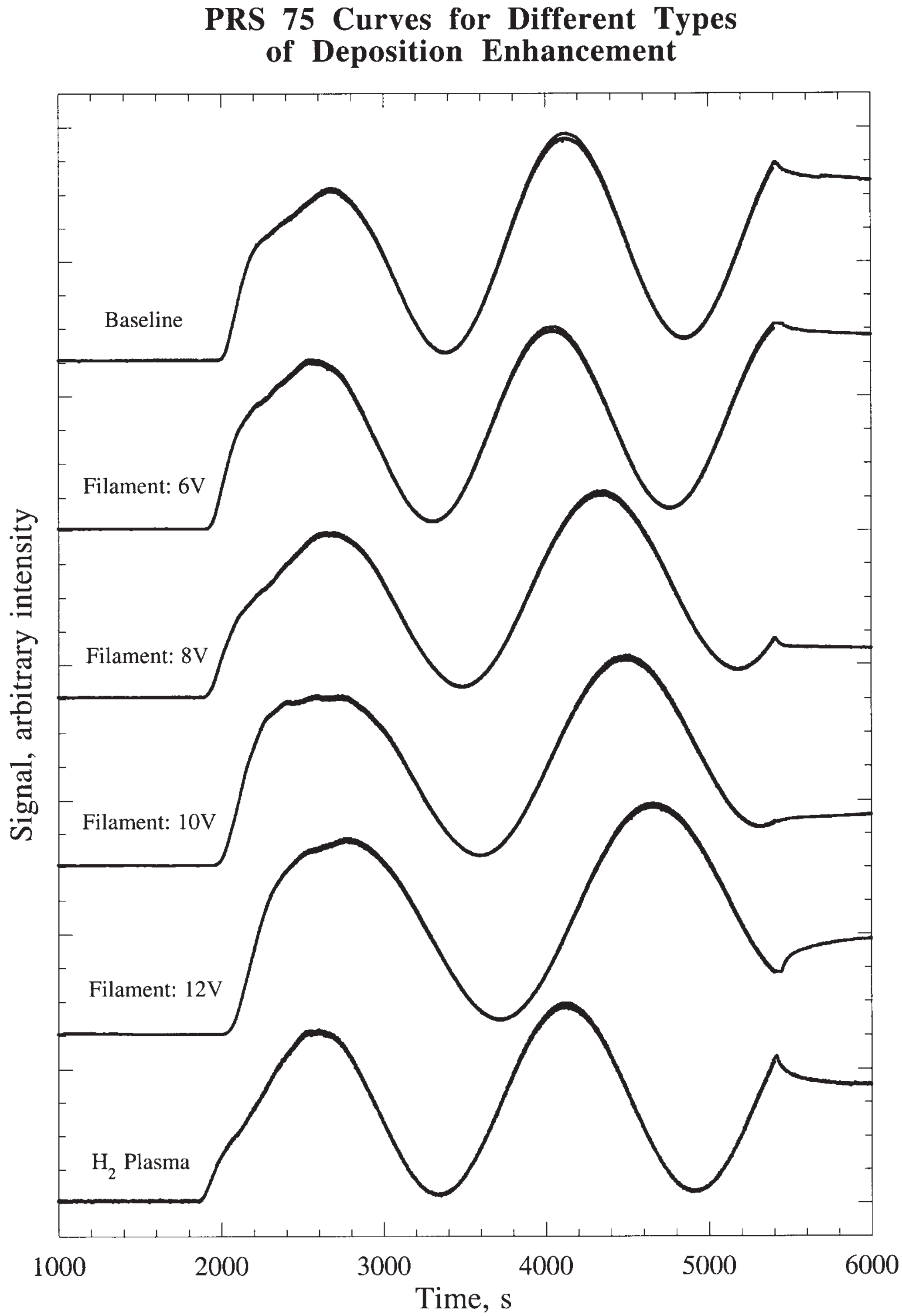

Figure 6.5: Reflectivity signal evolution at 75 degrees for GaP growing on Si under various excitation conditions.

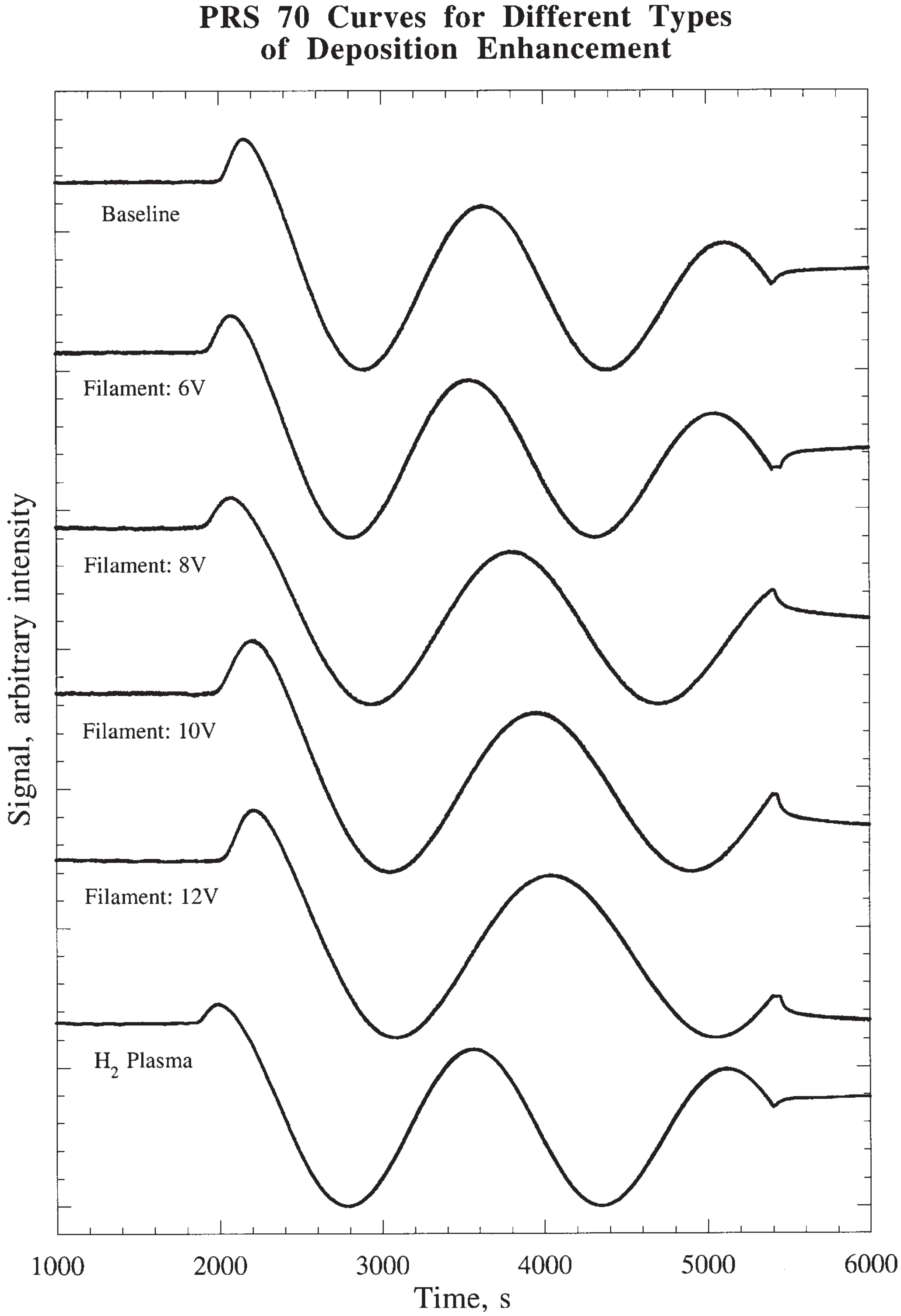

Figure 6.6: Reflectivity signal evolution at 70 degrees for GaP growing on Si under various excitation conditions.

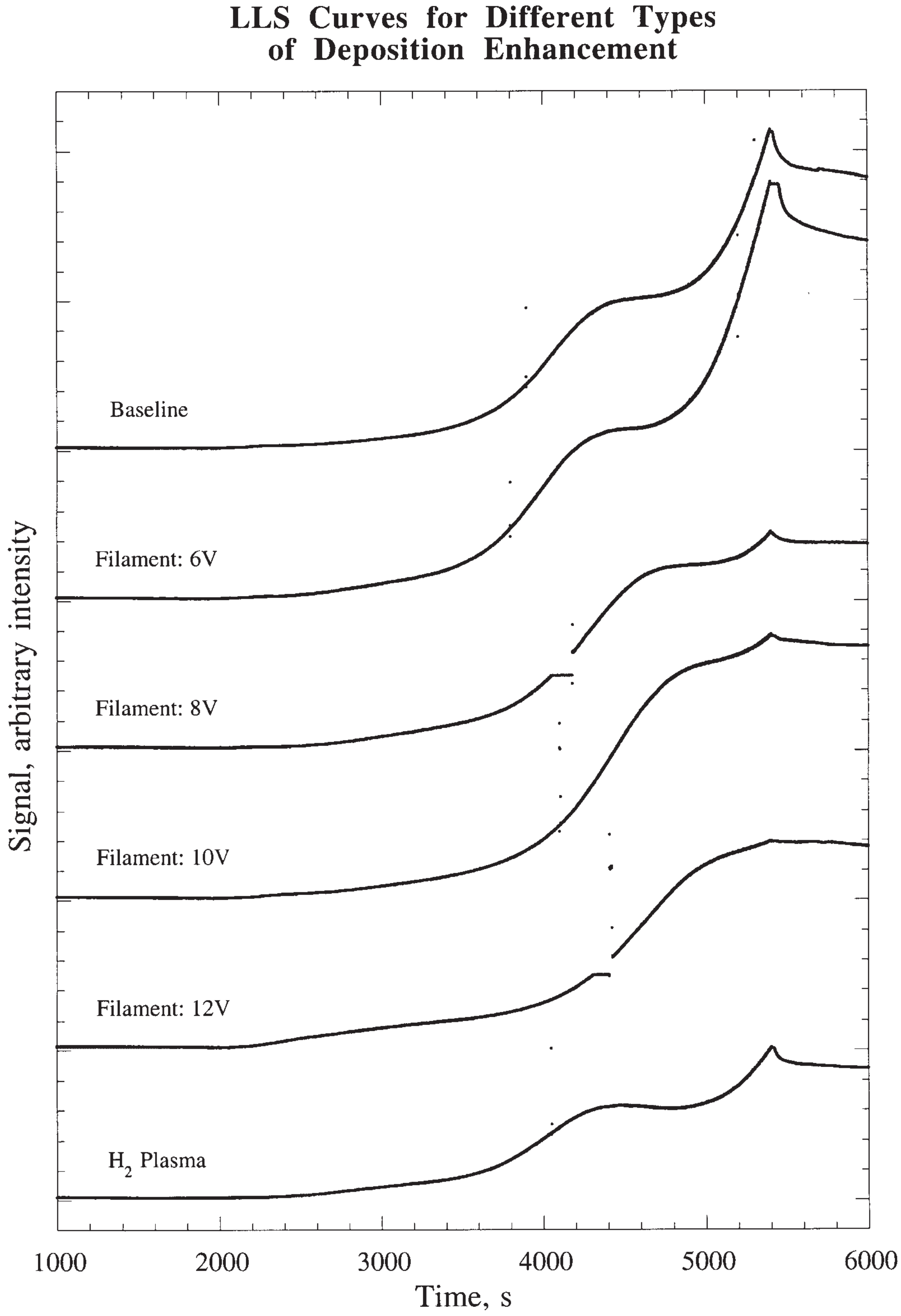

Figure 6.7: Scattered intensity evolution for GaP growing on Si under various excitation conditions.

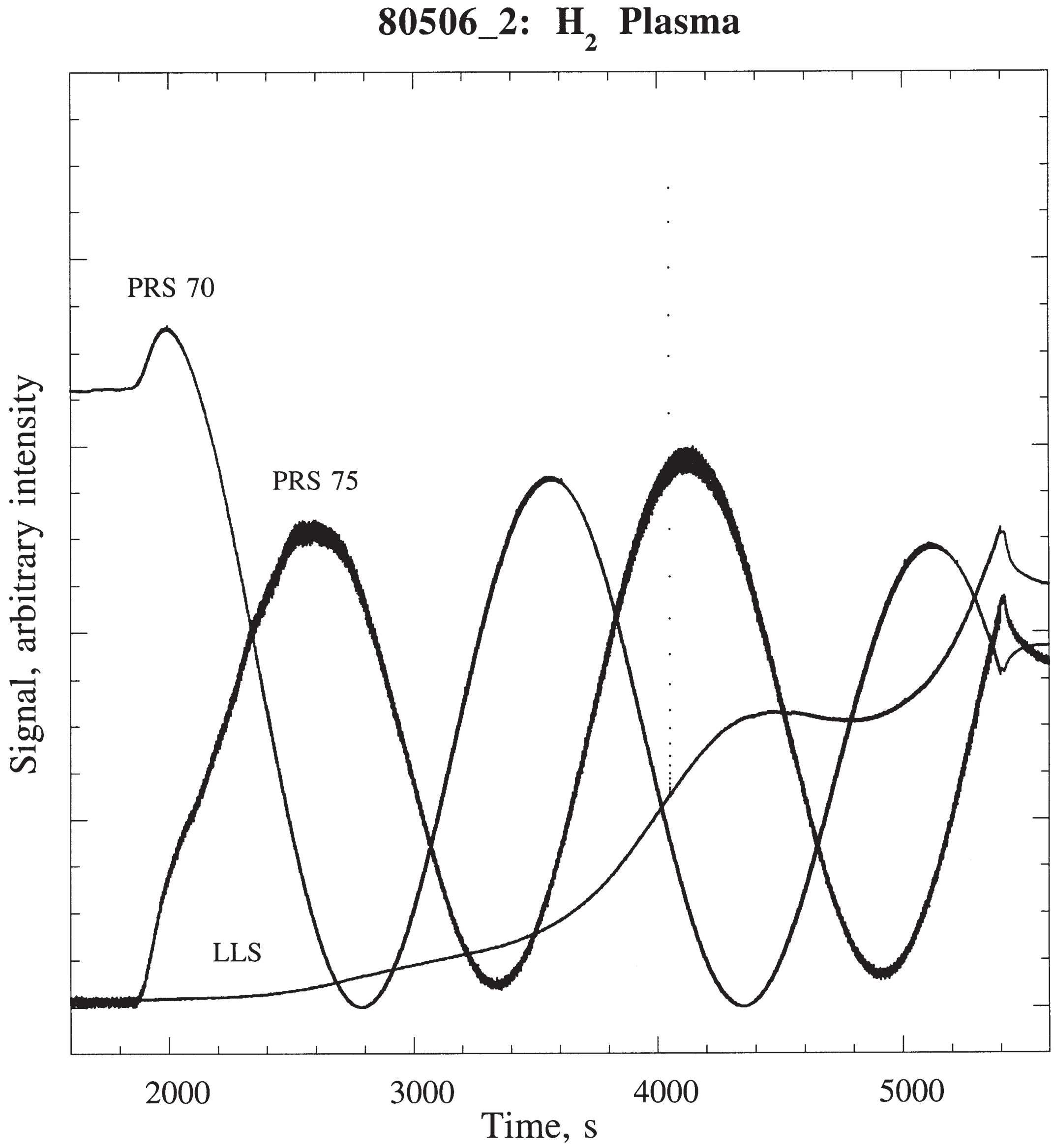

Figure 6.8: Optical response during GaP heteroepitaxial growth with a hydrogen plasma beam.

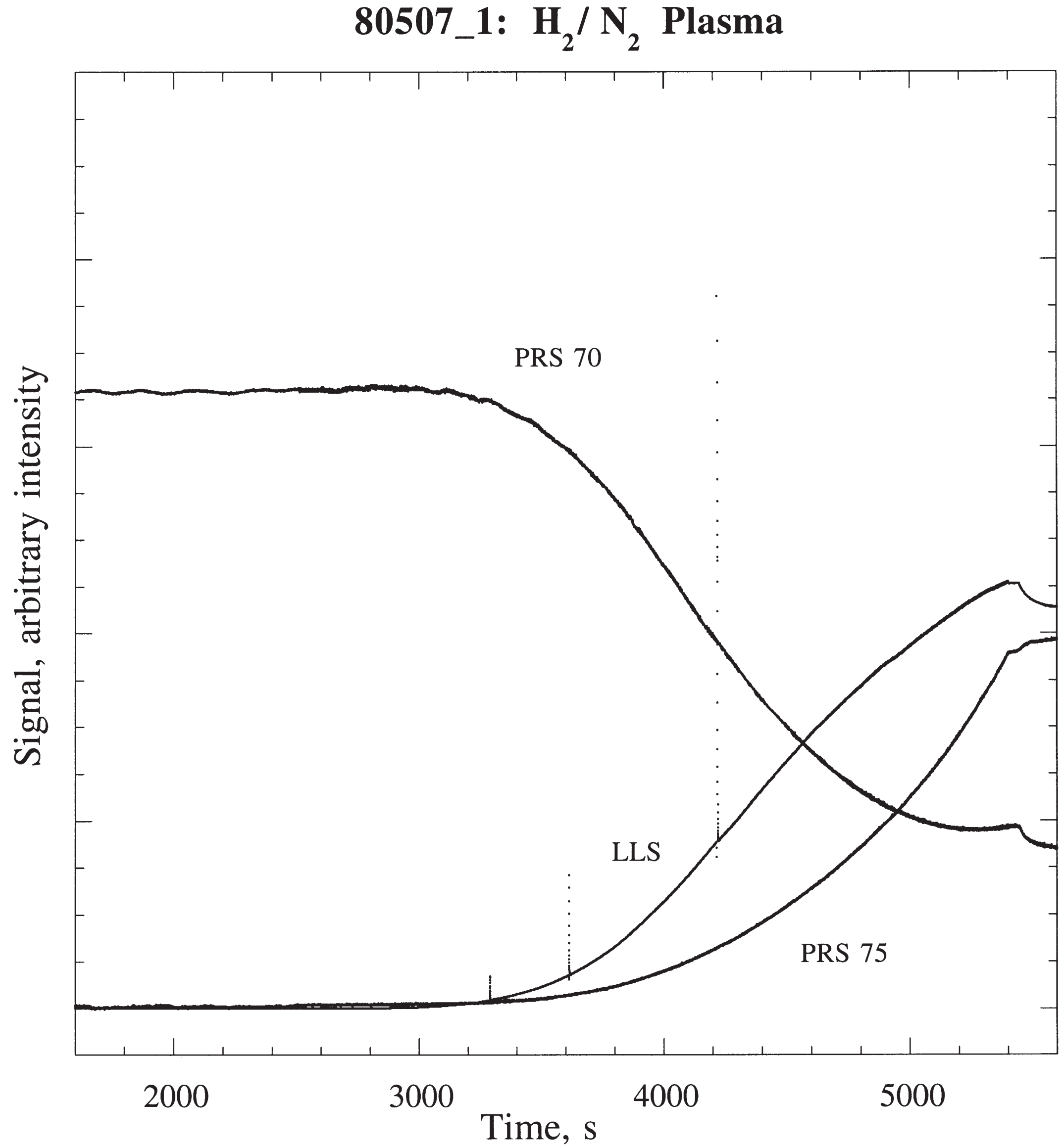

Figure 6.9: Preliminary attempts at GaPN deposition under similar GaP growth conditions except for a hydrogen/ nitrogen plasma beam.

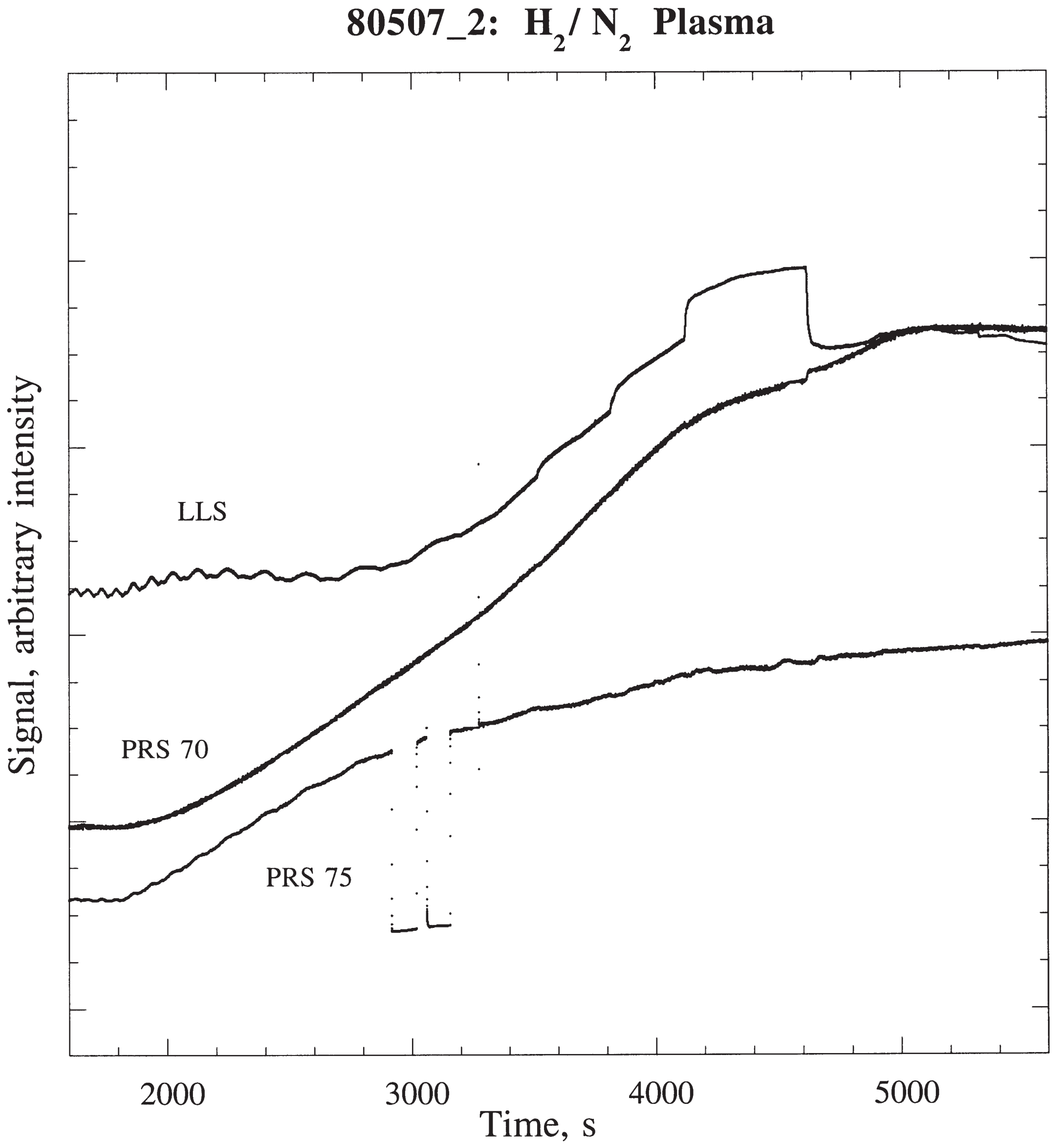

Figure 6.10: GaPN regrowth effort where the previous run is used as a template for subsequent deposition.

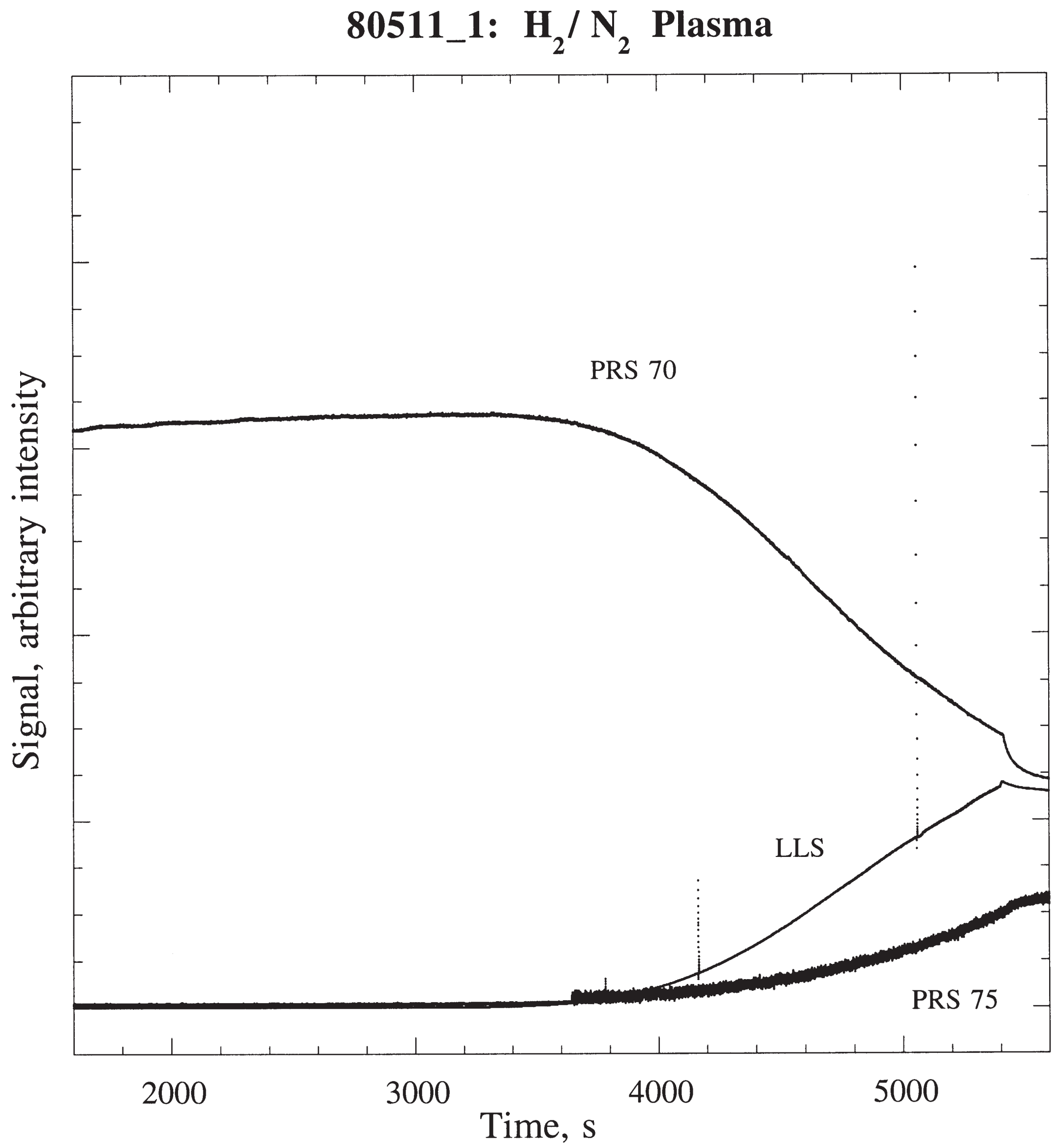

Figure 6.11: Fresh GaPN growth strategy where fine structure appears on the PRS 75 signal.

References

[6.1] Y. J. Van der Meulen and N. C. Hien, *Journal of the Optical Society of America*, **64**, 804 (1974).

[6.2] G. E. Jellison Jr. and F. A. Modine, *Physical Review*, **B27**, 7466 (1983).

[6.3] E. S. Hellman, et al., *MRS Internet Journal of Nitride Semiconductor Research*, **3**, 43 (1998).

[6.4] A. Barski, et al., *MRS Internet Journal of Nitride Semiconductor Research*, **1**, 21 (1996).

[6.5] E. Kim, et al., *MRS Internet Journal of Nitride Semiconductor Research*, **3**, 22 (1998).

[6.6] T. Zywietz, et al., *MRS Internet Journal of Nitride Semiconductor Research*, **3**, 26 (1998).

7

Future Recommendations

7.1 GaP

For a lattice mismatch of 0.5 % in the GaP/ Si growth system at 380 C, the critical thickness for the transition between elastic to plastic deformation ranges from 85 to 6500 Å, depending on which model is chosen, Van der Merwe or People & Bean. Furthermore, the two models converge at 4.0 % lattice mismatch yielding a 10 Å critical thickness[7.1]. Since the scattered intensity exhibits a plateau at 2400 Å, within the range of viable transformations, the hypothesis survives the first pass. One strategy to test this hypothesis further might involve $Ga_xIn_{1-x}P$ mixtures, because the models are based on average lattice mismatch. By x = 0.54, the lattice mismatch reaches 4.0 %, so a series of experiments increasing the indium concentration should dramatically impact the scattering plateau position if the hypothesis applies.

Considering the potential carbon radicals activated in a filament, an alternative way to precrack the TBP molecule involves an externally heated treatment chamber with baffles, similar to the ammonia On–Surface Cracking devices. Under this controlled environment, the carbon radicals can be kept to a minimum, and their energies suppressed, to avoid carbon incorporation. In terms of hydrogen activation, some trials exploring the difference between filament and plasma excitation might bear fruit through power density variations.

7.2 GaN

If the GaP buffer layer succeeds in achieving GaN deposition, a series of experiments where the growth temperature is varied at discreet values between 380 and 750 C, while maintaining the TBP flow, might yield some fascinating composition results. With rising growth temperatures, I would expect a declining phosphorous level, in accompany with an increasing nitrogen level, as the kinetic barrier for GaP decomposition succumbs to GaN formation. Thereafter, reflectivity studies focusing on plasma power and reactant flows could optimize GaN process conditions. With these variables in hand, the GaP buffer layer can be thinned out until a virgin substrate is attempted as the GaN growth template.

References

[7.1] S. Sharan, *MS Thesis*, North Carolina State University: Raleigh, NC (1987).